

Amorphous Silicon Based Microchannel Plates for Time-of-Flight Positron Emission Tomography

Présentée le 17 janvier 2023

Faculté des sciences et techniques de l'ingénieur
Laboratoire de photovoltaïque et couches minces électroniques
Programme doctoral en physique

pour l'obtention du grade de Docteur ès Sciences

par

Samira Alexandra FREY

Acceptée sur proposition du jury

Prof. N. Grandjean, président du jury
Prof. C. Ballif, Dr N. Würsch, directeurs de thèse
Dr W. Lustermann, rapporteur
Dr A. Tremsin, rapporteur
Prof. E. Charbon, rapporteur

If you think you are too small to make a difference, try sleeping with a mosquito.
—Dalai Lama

To my family, friends, my dog and the coffee machine...

Abstract

Microchannel plates fabricated from hydrogenated amorphous silicon (AMCPs) are a promising alternative to conventional glass microchannel plates. Their main advantages lie in their cheaper and more flexible fabrication processes, allowing for adaptable channel shapes, the possibility of vertical integration with an electronic readout, and the resistivity of the main amorphous silicon layer, which allows a charge replenishment by a current flowing directly through the bulk material. In the framework of this thesis, the design and fabrication of AMCPs were further developed to a point where they can now be considered a viable option for real applications such as time-of-flight positron emission tomography (TOF-PET). Small channel diameters down to $1.6\mu\text{m}$ could be achieved, allowing for fast timing characteristics of the devices. By increasing the aspect ratio to 25, the multiplication gain could be enhanced to around 1500 from the previous maximum of ~ 100 . Characterization of the fabricated devices was done in both the continuous and transient regimes, and a time resolution of (4.6 ± 0.1) ps was measured for the AMCP chip connected to a low-noise amplifier (LNA). This work on AMCPs was carried out as part of the Sinergia project, “MEMS based gamma ray detectors for time-of-flight positron emission tomography”. The envisioned detector in this project focuses on using Cherenkov radiation rather than scintillation to determine the annihilation site during TOF-PET imaging. Since Cherenkov radiation is quasi-instantaneous, this approach could significantly improve the timing resolution and, consequently, the scanner’s signal-to-noise ratio. Due to the low yield of Cherenkov photons per incoming gamma, detection efficiency becomes a critical factor. In an AMCP, the detection efficiency strongly depends on the sensor’s open area ratio (OAR). This OAR could be increased to around 95 % by fabricating funnel-shaped channel openings, demonstrating the potential of the fabrication flexibility of AMCPs.

Key words: Amorphous Silicon, Microchannel Plates, Vacuum Detector, Secondary Emission, Deep Reactive Ion Etching, Monolithic Integration, Plasma-enhanced Chemical Vapor Deposition, Time Resolution, Electron Detection

Zusammenfassung

Mikrokanalplattendetektoren aus amorphem Silizium (AMCPs) sind eine vielversprechende Alternative zur herkömmlichen Variante aus Glas. Ihre Hauptvorteile liegen im kostengünstigeren und flexibleren Herstellungsverfahren, welches anpassbare Kanalförmigkeiten ermöglicht, der Möglichkeit der Integration mit einer elektronischen Auslese und in der variablen Leitfähigkeit der amorphen Siliziumschicht. Die Ladungsträger können hier direkt durch den in der Schicht fließenden Strom ersetzt werden. Im Rahmen dieser Arbeit wurden Design und Herstellungsverfahren von AMCPs weiterentwickelt, so dass sie nun für reale Anwendungen, wie zum Beispiel der Positronen-Emissions-Tomographie mit Flugzeit Bestimmung (TOF-PET), in Betracht gezogen werden können. Detektoren mit schmalen Kanaldurchmessern von bis zu $1.6\text{ }\mu\text{m}$ konnten entwickelt werden und ermöglichen eine hohe Messgenauigkeit der Ankunftszeit eines Signales. Durch die Erhöhung des Seitenverhältnisses auf 25 konnte die Verstärkung der Detektoren vom bisherigen Maximum von ~ 100 auf bis zu 1500 erhöht werden. Die Charakterisierung der Detektoren erfolgte sowohl im kontinuierlichen Bereich als auch für kurzzeitige Ströme, und eine Zeitauflösung von $(4.6 \pm 0.1)\text{ ps}$ konnte gemessen werden für einen AMCP verbunden mit einem rauscharmen Verstärker (LNA). Die Weiterentwicklung von AMCPs erfolgte im Rahmen des Sinergia-Projekts “MEMS based gamma ray detectors for time-of-flight positron emission tomography”. Der in diesem Projekt vorgesehene Detektor konzentriert sich auf die Nutzung von Cherenkov-Strahlung anstelle von Szintillationsphotonen zur Bestimmung des Annihilationsortes während der TOF-PET Bildgebung. Da Cherenkov-Strahlung nahezu unmittelbar auftritt, könnte dieser Ansatz die zeitliche Auflösung und folglich das Signal-Rausch-Verhältnis des PET Systems erheblich verbessern. Aufgrund der geringen Ausbeute an Cherenkov-Photonen pro einfallender Gammastrahlung ist die Detektionseffizienz ein kritischer Faktor. In AMCPs wird diese Detektionseffizienz durch die aktive Fläche der Kanäle (OAR) begrenzt. Sie konnte durch die Herstellung trichterförmiger Kanalöffnungen auf etwa 95 % erhöht werden- ein Beweis für die Flexibilität in der Herstellung von AMCPs.

Stichwörter: Amorphes Silizium, Mikrokanalplatten, Vakuumdetektor, Sekundäremission, tiefes reaktives Ionenätzen, monolithische Integration, plasmaunterstützte chemische Gasphasenabscheidung, Zeitauflösung, Elektronendetektion

Résumé

Les plaques à micro canaux fabriquées à partir de silicium amorphe hydrogéné (AMCP) constituent une alternative prometteuse aux plaques à micro canaux conventionnelles en verre. Leurs principaux avantages résident dans leurs procédés de fabrication moins coûteux et plus flexibles permettant des formes de canaux adaptables, la possibilité d'une intégration verticale directement sur l'électronique de lecture, et une résistivité modulable de la couche principale de silicium amorphe permettant une recharge de la capacité par un courant circulant directement à l'intérieur du matériau. Dans le cadre de cette thèse, la conception et la fabrication des AMCPs ont été poussées à un point tel qu'elles peuvent maintenant être considérées comme une option viable pour des applications réelles telles que la tomographie par émission de positrons avec mesure du temps de vol (TOF-PET). Des diamètres de canaux aussi petit que $1.6\mu\text{m}$ ont pu être réalisés, permettant des appareils aux caractéristiques rapides. En augmentant le rapport de forme à 25, le gain de multiplication a pu être augmenté jusqu'à environ 1500 par rapport au maximum de ~ 100 des générations précédentes. La caractérisation des appareils a été effectuée dans des régimes continus et transitoires, et la résolution temporelle des détecteurs a été mesurée pour la première fois. Une gigue temporelle d'arrivée de $(4.6 \pm 0.1) \text{ ps}$ a pu être observée pour un AMCP connecté à un amplificateur à faible bruit (AFB). Cette dernière étude sur l'AMCP a été réalisée dans le cadre du projet Sinergia, "MEMS based gamma ray detectors for time-of-flight positron emission tomography". Dans le cadre de ce projet, le détecteur envisagé se concentre sur l'utilisation du rayonnement Cherenkov plutôt que de la scintillation pour déterminer le site d'annihilation pendant l'imagerie TOF-PET. Le rayonnement Cherenkov étant quasi instantané, cette approche pourrait améliorer considérablement la résolution temporelle et, par conséquent, le rapport signal sur bruit de l'image finale. Cependant, en raison du faible nombre de photons Cherenkov par rayon gamma entrant, l'efficacité de détection devient un facteur critique. Dans un AMCP, cette efficacité de détection est limitée par la surface active des canaux (OAR). Cette dernière a pu être augmentée à environ 95 % de la surface totale en fabriquant des ouvertures de canaux en forme d'entonnoir- démontrant ainsi le potentiel de flexibilité de fabrication des AMCPs.

Mots clefs : Silicium amorphe, plaques à micro canaux, détecteur à vide, émission secondaire, gravure ionique réactive profonde, intégration monolithique, dépôt chimique en phase vapeur assisté par plasma, résolution temporelle, détection des électrons.

Contents

Abstract (English/Deutsch/Français)	i
List of Figures	xi
List of Tables	xv
Acronyms	xvii
1 Introduction	1
1.1 Motivation and objective of this work	1
1.2 Contribution to the research field	2
1.3 Structure of this thesis	3
2 Amorphous Silicon Based Microchannel Plates	5
2.1 Hydrogenated amorphous silicon	5
2.1.1 Atomic structure and metastability of a-Si:H	5
2.1.2 Electronic transport in hydrogenated amorphous silicon	7
2.1.3 Radiation hardness	10
2.1.4 a-Si:H deposition	10
2.1.5 Summary	12
2.2 Microchannel plates	13
2.2.1 Structure and working principle	13
2.2.2 MCP properties	14
2.2.3 Limitations	15
2.2.4 MCP characteristics summary	16
2.3 Amorphous silicon based microchannel plates	16
2.3.1 AMCP working principle	17
2.3.2 Advantages and disadvantages of AMCPs	19
2.3.3 Current state-of-the-art	20
3 Detectors for Time-of-Flight Positron Emission Tomography	23
3.1 Sinergia project overview	23
3.2 Positron emission tomography	24
3.2.1 Working principle	24
3.3 Cherenkov radiation	27
	vii

3.4	AMCPs as photodetectors	30
3.5	Summary	31
4	AMCP Simulations	33
4.1	Modeling of AMCPs	33
4.1.1	Monte-Carlo Model	34
4.1.2	Finite Element Method Model	39
4.1.3	Model limitations	42
4.2	Simulation results	43
4.2.1	Simulation of a high aspect ratio device	43
4.2.2	AMCPs with funnel-shaped channels	46
4.2.3	AMCP with a trench geometry	48
4.3	Conclusion and summary	50
5	Fabrication of AMCPs	51
5.1	AMCP- fifth generation fabrication	51
5.1.1	Motivation and prior art	51
5.1.2	Process flow	53
5.1.3	High secondary emission layers	68
5.2	Alternative channel geometries	70
5.2.1	Funnel openings	70
5.2.2	Trench AMCPs	74
5.2.3	Low capacitance samples	75
5.2.4	Tilted channels	78
5.3	Conclusion and outlook	79
6	Characterization of AMCPs	81
6.1	Capacitance measurement	81
6.2	AMCP conductivity	83
6.3	Gain characterization	85
6.3.1	Setup description	85
6.3.2	Calibration of the photocathode	88
6.3.3	Gain measurements of the third generation of AMCPs	90
6.3.4	Electron energy inside the channels	94
6.3.5	Gain measurements of the fifth generation of AMCPs	95
6.3.6	Gain dynamics	103
6.3.7	Characterization of funnel-shaped AMCPs	105
6.4	Electron Beam Induced Current Measurements	107
6.4.1	Setup description	107
6.4.2	Measurements on third generation AMCPs	108
6.4.3	Measurements on forth generation AMCPs	111
6.5	Summary and conclusion	112

7	AMCP Integration	113
7.1	Planacon integration	113
7.1.1	AMCP chip design	114
7.2	Electronic integration and timing properties	119
7.2.1	Theoretical aspects	119
7.2.2	Measurement setup and procedure	121
7.2.3	Time resolution with and without an external amplifier	124
7.2.4	Time resolution without additional photocathode	127
7.2.5	Integrated amplifier	130
7.3	Conclusion and outlook	131
8	Discussion and Outlook	133
8.1	Summary of the main results	133
8.1.1	AMCP fabrication	133
8.1.2	AMCP gain and timing properties	134
8.2	Discussion of the research questions	136
8.3	Outlook	138
	Bibliography	145
	Acknowledgements	147
	Curriculum Vitae	149

List of Figures

2.1	Structure of amorphous silicon	5
2.2	Localized states in band diagram	6
2.3	Conduction mechanisms in a-Si:H	8
2.4	Doping of a-Si:H	9
2.5	Radiation hardness of a-Si:H	10
2.6	PE-CVD reactor chamber	11
2.7	MCP working principle	13
2.8	Glass MCP with funnels	15
2.9	AMCP working principle	17
2.10	A-Si:H emission yield	19
2.11	Intermediate electrode current	20
2.12	Gain 3 rd generation AMCPs	21
2.13	AMCP channels cross-section	21
3.1	Sinergia project schematic	24
3.2	Positron emission tomography.	25
3.3	Cherenkov radiation timing resolution	29
3.4	Gain simulation for aspect ratio 30	30
3.5	Hi-QE Photocathodes	31
4.1	Elastic backscatter probability	35
4.2	Emission yield curves	36
4.3	Secondary electrons emission energies	37
4.4	FEM simulation schematic	39
4.5	FEM simulation starting position	40
4.6	FEM simulation for aspect ratio 25	44
4.7	Gain vs Bias and arrival time jitter	45
4.8	FEM simulation for a funnel AMCP	46
4.9	FEM simulation for a funnel AMCP with MgO	47
4.10	FEM simulation for a trench AMCP	49
4.11	FEM simulation for a deep trench AMCP	50
5.1	Process flow: Bottom electrode	53
5.2	Bottom electrode design	54

5.3	Process flow: Decoupling layer	55
5.4	Intermediate electrode design	56
5.5	Process flow: Intermediate electrode	56
5.6	Adhesion layer optimization	57
5.7	Intrinsic stress as a function of the deposition pressure	59
5.8	Temperature dependence of intrinsic stress	60
5.9	Process flow: Multiplication layer	60
5.10	BARC coating	61
5.11	Top electrode design	62
5.12	Process flow: Top electrode	62
5.13	Bosch process schematic and scallop formation	63
5.14	Etching defects	65
5.15	Process flow: Channel etching	66
5.16	AMCP cross-section with aspect ratio 25	67
5.17	Process flow: ALD	68
5.18	MgO layer deposited by SALD	69
5.19	Funnel shape optimization	70
5.20	Top electrode for funnel AMCPs	71
5.21	Process flow: Funnel etching	72
5.22	Funnel device cross-section	73
5.23	Trench AMCP cross-section	74
5.24	Process flow: Low capacitance sample	75
5.25	Low capacitance AMCP cross-section	76
5.26	Schematic of a redesigned intermediate electrode	77
5.27	Channel tilt	78
6.1	Capacitance schematic	81
6.2	Capacitance measurement	82
6.3	Dark conductivity of a-Si:H	84
6.4	AMCP test structure design	85
6.5	Gain characterization setup	87
6.6	Photocathode calibration graph	88
6.7	Photocathode calibration	89
6.8	Gain measurement for a sample with AR:11.7	91
6.9	Gain measurement for a sample with AR:13.6	92
6.10	Gain measurement for a sample with AR:11.5 and ALD coating	92
6.11	Electron energy measurement schematic	94
6.12	Maximum electron energy measurement	94
6.13	Gain as a function of incident energy	96
6.14	Typical output signals for different applied biases	97
6.15	Measured gain for MCP152C9	98
6.16	Measured gain for Planacon2C5	99

6.17 Channel geometry comparison	100
6.18 Comparison between measured and simulated gain	101
6.19 Gain dynamics for AMCP generation 3	103
6.20 Gain dynamics for AMCP generation 5	104
6.21 Funnel gain measurement	106
6.22 EBIC setup schematic	107
6.23 EBIC Map showing the influence of the bias voltage	108
6.24 EBIC Map showing the influence of the beam tilt	109
6.25 EBIC Map showing charging effects	110
6.26 EBIC Map for the fourth generation of AMCPs	111
7.1 Planacon schematic	114
7.2 Planacon chip design	115
7.3 Planacon die attach	116
7.4 Quantum efficiency of the Planacon photocathode	117
7.5 Planacon assembly	118
7.6 MCP jitter theoretical aspects	120
7.7 MCP Jitter- influence of noise	121
7.8 Timing measurement setup	122
7.9 Timing measurement board design	124
7.10 Acquired waveforms for the timing measurement	125
7.11 Arrival time distribution with and without amplifier	125
7.12 Time walk correction	126
7.13 Time resolution measurement without additional photocathode	127
7.14 Time resolution measurement with decreased laser power (160 nJ)	128
7.15 Time resolution measurement with decreased laser power (100 nJ)	128
7.16 Time resolution change with signal amplitude	129
7.17 Time resolution measurement with integrated amplifier	130

List of Tables

2.1	Properties of a-Si:H	12
2.2	MCP Properties	16
4.1	Monte-Carlo Model parameters	38
4.2	Simulation parameters for an AMCP with AR 25.	43
4.3	Simulation results for an AMCP with AR 25.	44
4.4	Simulation parameters for an AMCP with a funnel-shaped opening	46
4.5	Simulation results for a funnel AMCP with and without MgO	48
4.6	Simulation parameters for an AMCP with trenches.	48
4.7	Simulation results for an AMCP with trenches.	49
5.1	AMCP Generations Overview	52
6.1	Capacitance	83
6.2	Properties of characterized AMCPs and measurement conditions	90
6.3	Gain measurements generation 3 AMCP	93
6.4	Properties of characterized AMCPs and measurement conditions	95
6.5	Summary of the measured devices from AMCP generation 5	99
6.6	Funnel AMCP	105
7.1	Planacon chips specifics	115
7.2	Time resolution measurement setup	123

Acronyms

a-Si:H	hydrogenated amorphous silicon
ALD	atomic layer deposition
AMCP	amorphous silicon based microchannel plate
APD	avalanche photodiode
ARDE	aspect ratio dependent etching
BARC	bottom anti-reflective coating
BGO	bismuth germanium oxide
CMOS	complementary metal–oxide–semiconductor
CsI	caesium iodide
CT	computerized tomography
CTR	coincidence time resolution
DB	dangling bond
DRIE	deep reactive ion etching
EBIC	electron beam induced current
EDX	energy-dispersive X-ray spectroscopy
FDG	fluorine-18 fluorodeoxyglucose
FEM	finite element method
FWHM	full width at half maximum
GaN	gallium nitride
GEANT4	geometry and tracking
LNA	low-noise amplifier

LYSO	lutetium yttrium oxyorthosilicate
MCP	microchannel plate
MgO	magnesium oxide
MRI	magnetic resonance imaging
Nd:YAG	neodymium-doped atrium aluminum garnet
OAR	open area ratio
PCB	printed circuit board
PDE	photon detection efficiency
PE-CVD	plasma enhanced chemical vapor deposition
PET	positron emission tomography
QE	quantum efficiency
RF	radio frequency
SALD	spatial atomic layer deposition
SCLC	space-charge-limited current
SEE	secondary electron emission
SEM	scanning electron microscope
SEY	secondary emission yield
SiC	silicon carbide
SiO	silicon oxide
SiPM	silicon photomultiplier
SMA	subminiature version A
SNR	signal-to-noise ratio
SPTR	single photon timing resolution
SWE	staebler-wronski effect
TMA	tri-methyl aluminum
TOF	time-of-flight
TSV	through silicon vertical electrical connection

UV ultraviolet

VHF very high frequency

1 Introduction

1.1 Motivation and objective of this work

Particles and their interactions with one another are what govern, on the most fundamental level, the physics of our universe. Advances in particle and radiation detectors have given us new insights into many phenomena happening in space as well as inside our bodies. In medical imaging, for instance, the detection of the arrival times of gamma rays stemming from the decay of an inserted radiotracer reveals information about the metabolic activity of the patient. This imaging technique is commonly used in oncology to localize tumor cells but also to investigate brain disorders and heart problems [1]. The detectors used in time-of-flight (TOF)-positron emission tomography (PET) systems need to possess a high time resolution in the order of picoseconds to achieve detailed tomographic scans while keeping the radiation dose as low as possible [2]. Currently available detectors, such as silicon photomultipliers (SiPMs) or microchannel plates (MCPs), already exhibit excellent performances. However, detector characteristics such as the count rate, time- and spatial resolution can still be further improved by exploring alternative solutions. This thesis presents the further development and characterization of an amorphous silicon based microchannel plate (AMCP) detector. This technology presents some unique advantages, such as the possibility of fabricating monolithic detectors, flexibility in the fabrication process, and a variable conductivity of the bulk material. AMCPs have the potential to achieve an exceptional time resolution of a few picoseconds. Together with their high spatial resolution of a few μm and possible fast charge replenishment, they could be envisioned as an alternative to MCPs or SiPMs in PET systems or other applications such as mass spectrometry.

The following research questions were investigated during the duration of this thesis:

1. What is the minimal AMCP gain needed for their use in real applications, such as TOF-PET scanners, and which other requirements need to be fulfilled?
2. Can the fabrication process of AMCPs be improved to meet these requirements?
3. What are the advantages and limits of AMCPs, and can they overcome some of the limitations of conventional MCPs?

To summarize, this thesis aimed at improving the performance of AMCPs, evaluate their characteristics and investigate their potential to replace current standard detectors, such as glass MCPs or SiPMs in certain applications.

1.2 Contribution to the research field

In the framework of this thesis, fabrication issues present in earlier AMCP generations have been resolved, resulting in a working detector with a gain of 1500, a significant increase compared to previous devices where the multiplication factor was limited to around 100. The great flexibility in channel geometry is one of the significant advantages of the hydrogenated amorphous silicon (a-Si:H) based technology. The geometry of the channels was adjusted to allow for an active area of the detectors of around 95 %, opening the possibility of performing single particle counting with these detectors. Other channel shapes were also investigated, and their performance was simulated. The simulation results have shown that the gain can be further increased to at least 3000-4000 by implementing a trench geometry and possibly even more by using wall coatings with a high secondary emission yield (SEY). The performance of the fabricated devices was tested under conditions similar to potential applications. A first investigation into the timing properties of the devices underlined their vast potential in applications where outstanding timing resolution is needed, such as medical imaging detectors or TOF measurements. Given the radiation hardness of amorphous silicon, AMCPs would also be suitable for high-energy physics or space applications. Finally, the first steps towards an integrated prototype TOF-PET detector were taken.

1.3 Structure of this thesis

This thesis is structured as follows. In Chapter 2, the overall topic is introduced, describing the material properties and growth mechanism of a-Si:H, state-of-the-art MCPs are reviewed, and some of their limitations are highlighted. Finally, AMCPs are introduced, stating the main motivations behind their development, their working principle, and reviewing previous generations of sensors and the challenges that still need to be overcome. Chapter 3 places the further development of AMCPs in the context of a prototype detector for a TOF-PET scanner, outlining the issues being addressed in this thesis. In Chapter 4, the modeling of AMCPs is presented. It shows the implementation of a cinematic Monte-Carlo model, developed within the framework of a previous thesis, into a finite element method (FEM) model so that non-cylindrical channel geometries can be more easily simulated. Simulation results from the fabricated structures are presented, including a high aspect ratio device, channels with funnel-shaped openings, and trench-shaped sensors. In Chapter 5, the design and fabrication of the newest generation of AMCPs are presented in detail, leading to the development of sensors with aspect ratios up to 25. Alternative fabrication steps are explored to address some of the remaining issues of the detectors, such as the low detection efficiency, high output capacitance, and limited multiplication gain. Chapter 6 presents the characterization of the fabricated devices, the resistivity of the layers, the capacitance of the different sensor designs, and the channel multiplication gain. Gain measurements under continuous and pulsed illumination are presented, and the results are compared with the simulations presented earlier. In the subsequent Chapter 7, the first steps toward an integrated detector are presented, describing the implementation of three AMCP chips into a vacuum-sealed tube called Planacon. Measurements of the timing properties of AMCPs are presented, displaying their potential for fast timing applications. Finally, in Chapter 8, the main results of this work are summarized and discussed, and an outlook for future improvements is provided.

2 Amorphous Silicon Based Microchannel Plates

2.1 Hydrogenated amorphous silicon

Amorphous solids are a group of materials characterized by a certain degree of disorder in their atomic structure. While glass, the most well-known representative of this group, has been used since ancient times, the structure and properties of these materials have been the subject of scientific studies for only a few decades. Their physical properties derive from the degree and nature of disorder, which can be controlled during manufacturing, making them promising materials for many novel applications. The following section summarizes the fundamental properties and the fabrication process of a-Si:H.

2.1.1 Atomic structure and metastability of a-Si:H

Amorphous silicon is a tetrahedrally-bonded disordered semiconductor. Whereas the material retains the organized configuration of crystalline silicon on a short-range scale, the long-range order is gradually lost [3]. Figure 2.1 illustrates the structure of the amorphous silicon network.

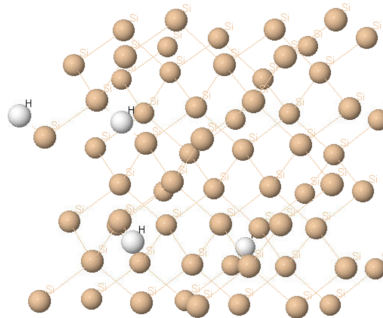


Figure 2.1: Model of the a-Si:H network. Long-range order is gradually lost due to variation in bond length and angle. Some of the Si-Si (orange) bonds are broken and are passivated by hydrogen (white).

Variations in bond length and angle lead to bonds with weakened binding energy. The band diagram represents these bonds as localized states in the bandgap where they form the band tails. The band tails exponentially decrease towards the middle of the gap, as shown in Figure 2.2. Many Si-Si bonds are also broken, called dangling bonds (DBs) or defects. They generate additional localized states near the middle of the bandgap. These DBs are present in high concentrations in pure amorphous silicon obtained from sputtering. When the material is deposited by glow discharge of silane (SiH_4) [4], the present hydrogen can partially passivate the broken bonds and hence decrease the defect density [5]. The resulting material is then referred to as a-Si:H. Hydrogenated amorphous silicon is not a homogeneous material but instead consists of voids embedded in the amorphous matrix [6]. The size and density of these voids depend on the deposition conditions, with a poor-quality material having a void fraction of around 20 %. In contrast, device quality a-Si:H has been shown to contain only around 1 % voids with diameters of around 100 nm [7]. The density of amorphous silicon is 2.15 gcm^{-3} , which is slightly lower than that of crystalline silicon.

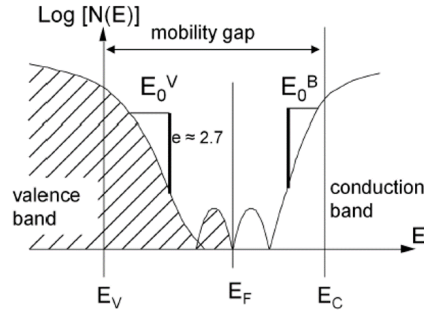


Figure 2.2: Graphic showing the density of states as a function of energy. The states in the band tails decrease exponentially towards the middle of the gap. The states near the Fermi energy E_F correspond to the dangling bonds.

The density of dangling bonds and hence the electronic properties of a-Si:H strongly depends on the deposition parameters (temperature, hydrogen concentration, doping concentration, and deposition rate) [8]. A critical aspect of a-Si:H lies in its intrinsic metastability. After the deposition, the DBs density varies under external influences rather than staying constant. At any given temperature, the DBs density stabilizes at an equilibrium value such that the generation and removal rates of defects are equal. Upon exposure to light, the conductivity of a-Si:H decreases, called the staebler-wronski effect (SWE) [9]. This effect is due to an increase in defects. The induced defects are metastable and can be removed by annealing the material at a high temperature for a few hours.

The optical and electronic properties of the material are influenced mainly by the localized states. The presence of the band tails enables optical absorption of energies lower than the bang gap (between 1.4 eV and 1.7 eV). They also influence carrier mobility by trapping charges as they move through the material. On the other hand, DBs act as recombination centers, as a charge once trapped is unlikely to be released. In this aspect, DBs are more detrimental to the electronic properties than the band tails because charges are lost.

2.1.2 Electronic transport in hydrogenated amorphous silicon

Conduction mechanisms

The presence of localized states strongly influences electrical conduction in amorphous silicon. Different conduction mechanisms are dominant at various temperature ranges. If the temperature is large enough, carriers trapped in localized states can be excited to states in the valence or conduction band where they can move freely. This conduction mechanism is referred to as extended state conduction, and it is the dominant conduction mechanism at room temperature. The movement of the carriers is characterized by multiple trapping and release processes. The higher the temperature, the shorter the trapping time, and hence the larger the carrier density in the extended states. The conductivity σ can be described by

$$\sigma = en\mu = \int en(E)\mu(E)f(E, T)dE \quad (2.1)$$

with the elementary charge e , the carrier density n and the carrier mobility μ . The Fermi-Dirac function $f(E, T)$ describes the probability that a state with energy E is occupied. In the case when the energy difference between the conduction band edge E_C and the Fermi level energy E_F is large, Equation 2.1 can be simplified to:

$$\sigma = \frac{1}{kT} \int_0^\infty \sigma^*(E) \exp\left[-\frac{E - E_F}{kT}\right] dE. \quad (2.2)$$

Integrating Equation 2.2 finally leads to

$$\sigma = \sigma_0 \exp\left[-\frac{E_0(T) - E_F(T)}{kT}\right] = \sigma_0 \exp\left[-\frac{E_a(T)}{kT}\right], \quad (2.3)$$

where $\sigma^*(E) = n(E)e\mu(E)kT$ is the conductivity at $E = E_F$ and $\sigma_0 = n(E_C)e\mu_0kT$ the minimal conductivity in the extended states. $E_a(T)$ is the activation energy.

At lower temperatures hopping conductivity becomes the primary conduction mechanism. In what is called nearest-neighbor hopping, carriers move from one band tail state to the spatially closest state by tunneling. Phonons are absorbed or emitted to compensate for the energy difference between the initial and final state.

This conductivity strongly depends on the temperature. For temperatures below 200 K, the hopping occurs between the two energetically closest states, called variable range hopping. The three main conduction mechanisms are summarized in Figure 2.3.

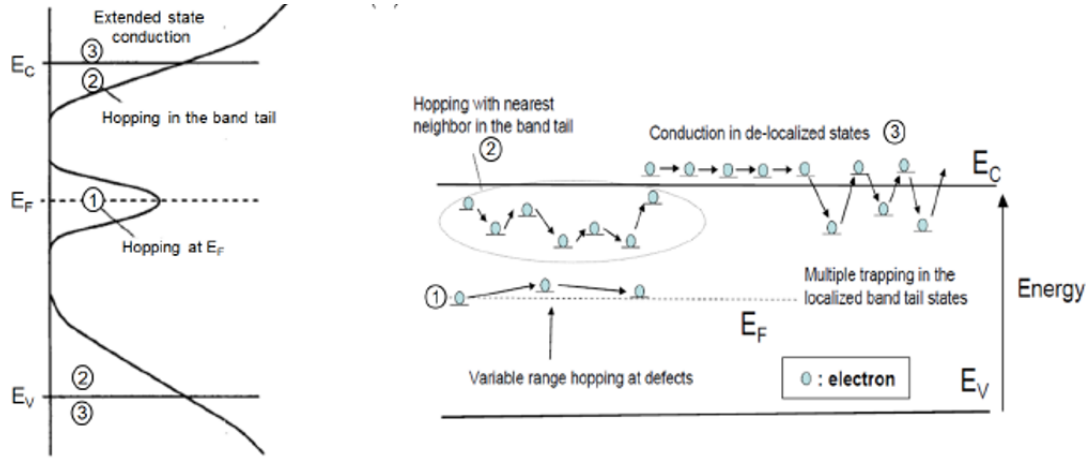


Figure 2.3: Schematic summarizing the three primary conduction mechanisms in a-Si:H—variable-range hopping, nearest-neighbor hopping, and extended-state conductivity (Image taken from [10]).

Another essential aspect to consider is the change in conductivity near the material's surface. It has been reported that additional localized states exist near the surface [11]. These additional states are primarily induced by the absorption of oxygen and water molecules. Oxygen acts as a donor in a-Si:H, and the hydrogen in the water molecules induces an electron accumulation near the surface. Electrical conductivity can hence locally increase by a few orders of magnitude [12]. Annealing at temperatures above 100 °C makes the molecules desorb and restores the bulk conductivity.

Doping of a-Si:H

The electronic properties of amorphous silicon massively improved once it could be deposited by glow discharge of silane, which allowed the passivation of dangling bonds by hydrogen. This deposition method also allows the possibility to efficiently dope a-Si:H by introducing phosphine (PH_3) or diborane (B_2H_6) into the gas mixture. The conductivity can be changed by several orders of magnitude from $\sigma = 10^{-12} \Omega^{-1} \text{cm}^{-1}$ to $\sigma = 10^{-2} \Omega^{-1} \text{cm}^{-1}$ [13]. The conductivity as a function of the phosphine/boron ratio is shown in Figure 2.4. As can be seen from the graph, intrinsic a-Si:H shows a slightly n-doped behavior. This is due to the incorporation of impurities, like oxygen, that act as electron donors during deposition. The doping efficiency of a-Si:H is not as good as the one for crystalline silicon. Additional defects are created with larger doping concentrations, which eventually causes the increase in conductivity to saturate [14].

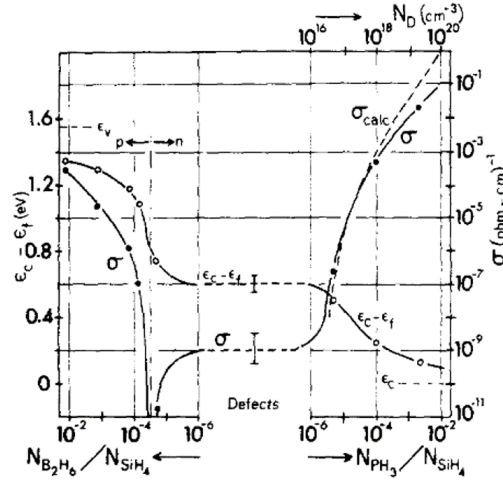


Figure 2.4: Doping efficiency of amorphous silicon. Room temperature conductivity can be changed by several orders of magnitude by doping the material with either phosphine or boron (Image taken from [13]).

Photoconductivity

Photoconductivity occurs when the creation of electron-hole pairs under illumination leads to an increase in free-carrier density. In the case of amorphous silicon, its conductivity can be increased by up to five orders of magnitude under illumination with visible light [15]. The total conductivity σ_{tot} is then given by the sum of the dark conductivity σ_{dark} and the photoconductivity σ_{photo} :

$$\sigma_{tot} = \sigma_{dark} + \sigma_{photo} = \sigma_{dark} + e(n\mu_{n^d} + p\mu_{p^d}), \quad (2.4)$$

where n and p are the photogenerated electron and hole concentrations and μ_{n^d} , μ_{p^d} their drift mobilities, respectively. In the case of thermal equilibrium where carrier concentration and recombination rates are the same this can be rewritten as

$$\sigma_{photo} = eG(\mu_n\tau_n^R + \mu_p\tau_p^R), \quad (2.5)$$

where G is the generation rate, μ_n and μ_p the electron and hole band mobilities and τ_n^R , τ_p^R the electron/hole lifetimes before recombination.

2.1.3 Radiation hardness

Another feature that makes hydrogenated amorphous silicon stand out is its remarkable radiation hardness. A-Si:H diodes were irradiated with a high-energy proton beam. The irradiation led to an increase in the dark current, which could be almost completely reversed after thermal annealing [16]. This high radiation tolerance makes a-Si:H an attractive candidate for many applications, especially in the fields of high-energy physics, radiotherapy, and diagnostic imaging.

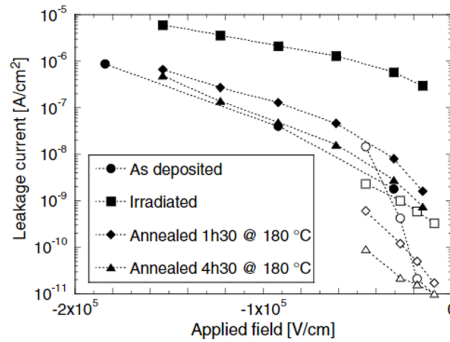


Figure 2.5: Dark current as a function of the applied field for a 1.1 μm and a 32.6 μm (full symbols) thick diode, respectively, shown before and after irradiation with a 405 keV proton beam and after annealing at 180 °C (Image taken from [16]).

2.1.4 a-Si:H deposition

The first depositions of amorphous silicon were done in the 1950s by evaporation. The result was a highly defective material unusable for electronic applications. Interest in the material was raised only a couple of years later when amorphous silicon films could be grown by plasma enhanced chemical vapor deposition (PE-CVD) with silane as a precursor gas [4]. During PE-CVD depositions, defects could be partially passivated by hydrogen, hence massively improving the material's electronic properties. The first successful doping of a-Si:H in 1975 [17], hydrogenated amorphous silicon started to be considered for a variety of applications such as solar cells and thin-film transistors [18]. A schematic of a typical PE-CVD reactor is shown in Figure 2.6. The precursor gases (SiH_4 , potentially hydrogen (H_2) and doping gases), enter the reactor through a showerhead at the bottom of the chamber. This ensures a uniform distribution of the gases over the substrate surface. A radio frequency (RF) electric field is applied between two capacitively coupled electrodes. The standard RF frequency is 13.56 MHz. For the growth of thick a-Si:H layers an adopted frequency of 70 MHz, known as very high frequency (VHF) PE-CVD, is used. This change in frequency enables to grow layers with a high deposition rate and low intrinsic stress [20], [21].

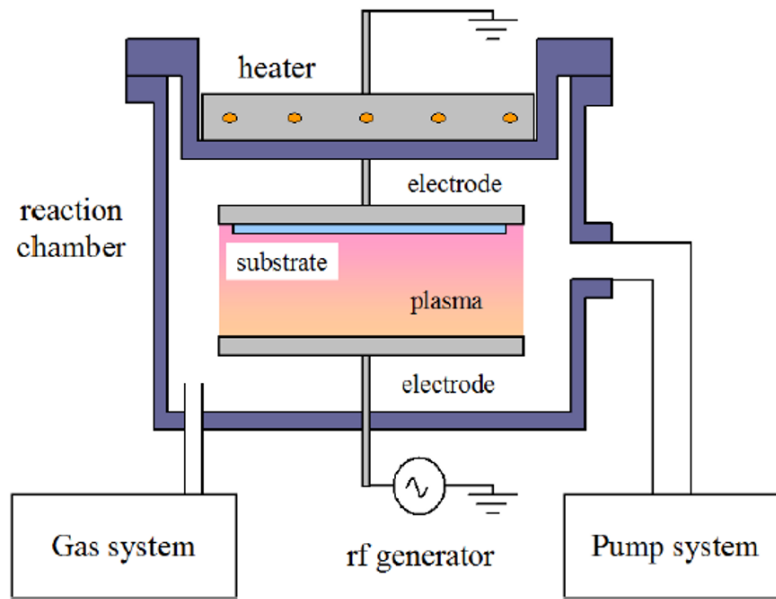


Figure 2.6: Schematic of a typical reactor chamber for PE-CVD processes. The substrate is placed on the top electrode. The gases enter at the bottom of the chamber. The plasma is ignited between the two capacitively coupled electrodes (Image taken from [19]).

The RF power induces a plasma which is a partially ionized gas containing ions, electrons, and neutral excited gas molecules (radicals). Photon emission during the transition of an electron between an excited and ground state causes the plasma in the chamber to light up. This so-called glow discharged plasma is characterized by a lack of thermal equilibrium between the electron temperature T_e and the gas temperature T_g . Due to their lighter mass and higher mobility, electron temperature can reach up to 10000 K, while the gas temperature is typically close to room temperature in the plasma. Due to the low gas temperature, a glow discharge plasma is called cold plasma. The main advantage of PE-CVD is that the film growth becomes possible at a much lower temperature than before without the plasma, allowing for a wider choice of substrate materials incompatible with high-temperature processes. The properties of the grown a-Si:H film depends strongly on the deposition parameters such as plasma frequency, substrate temperature, gas flows, and chamber pressure and have to be carefully tuned to achieve the desired material properties. More details on the specific deposition conditions for amorphous silicon based microchannel plates are given in Chapter 5. One significant advantage of PE-CVD deposition is that large areas can be uniformly covered at a low cost.

2.1.5 Summary

The last section provided an overview of the essential material characteristics of hydrogenated amorphous silicon and its fabrication. Table 2.1 lists some numerical values of important properties that are referenced throughout this thesis.

Table 2.1: Properties of a-Si:H

Property	Value	Unit
Density	2.15	g cm^{-3}
Atomic Density	$5 \cdot 10^{22}$	cm^{-3}
Band Tail States	$\sim 10^{19}$	cm^{-3}
Defect Density	$\sim 10^{15}$	cm^{-3}
Optical Band Gap	1.6 – 1.7	eV
Mobility Gap	1.7 – 1.8	eV
Dark Conductivity (Intrinsic)	$10^{-10} - 10^{-12}$	$\Omega^{-1} \text{cm}^{-1}$
Activation Energy	0.7 – 0.8	eV
Electron Drift Mobility	1-10	$\text{cm}^2 \text{V}^{-1} \text{s}^{-1}$
Hole Drift Mobility	$3 \cdot 10^{-3} - 10^{-1}$	$\text{cm}^2 \text{V}^{-1} \text{s}^{-1}$
E-H pair Creation Energy	4-6	eV

2.2 Microchannel plates

MCPs are electron multipliers invented as an alternative to secondary electron multipliers with a set of discrete dynodes in the 1970's [22]. Nowadays, they are widely used to detect electrons, ions, neutrons or photons, particularly in image intensifiers and image converters. Other applications include time-of-flight mass spectrometry, nuclear physics, astrophysics, and electron microscopy.

2.2.1 Structure and working principle

The basic structure and working principle are illustrated in Figure 2.7. MCPs consist of a thin glass plate with many micrometer-sized channels going through the glass substrate. The channel length to diameter ratio is called aspect ratio α and is typically between 40:1 and 80:1 with pore (channel) diameters between 10 and 20 μm . An electric field is established over the channels by applying a bias voltage V_D (typically of a few hundred volts) on one side of the MCP. An incoming particle reaches one of the channel entrances and drifts according to the accelerating electric field towards the other end of the channel. By doing so, it may collide several times with the channel wall. At each collision, more electrons are released by secondary electron emission. These secondary electrons are then accelerated by the electric field, hitting the channel walls again and causing the release of new secondary electrons. Like this, an exponentially increasing number of electrons is reaching the other end of the micro-channel. This avalanche process happens at a timescale of picoseconds, making MCPs one of the fastest detectors available. The multiplication factor of MCPs is generally in the order of $10^3 - 10^4$. Higher gains up to 10^7 can be achieved by stacking several microchannel plates on top of each other.

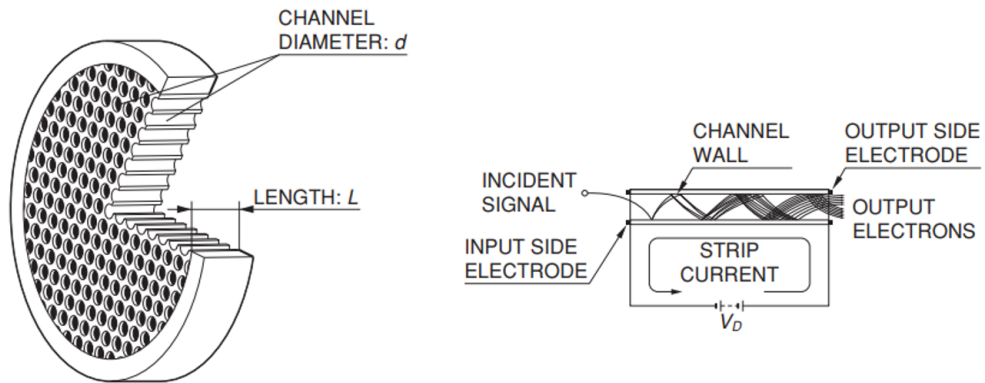


Figure 2.7: Schematic representation of the MCP working principle. An incident particle strikes one of the channel walls, creating secondary electrons. These secondary electrons are then accelerated by an applied electric field, colliding again with the channel walls, causing a multiplication of the original signal (Image taken from <http://www.hamamatsu.com>).

During the multiplication process, electrons are drawn from the bulk material. The time it takes to recover these charges is called charge replenishment time. It is the needed waiting time between the detection of two consecutive events and is typically in the order of a few milliseconds, determined by the plates resistance ($\gg 1 \text{ M}\Omega$) and capacitance ($\sim 100 \text{ pF}$) [23]. Since the glass of conventional MCPs is too resistive for replenishing the secondary electrons, a semiconducting layer is grown on the channel surface by a high-temperature hydrogen reduction process called hydrogen firing. The replenishing current flowing in this semiconducting layer, called strip current, also sets the uniform electric field distribution inside the channels. An emissive layer is needed on the channel surface to increase the secondary electron yield properties. This layer can be implemented by either channel wall oxidation with silicon oxide (SiO_2) or, more commonly nowadays, by coating the walls by atomic layer deposition (ALD) with a high secondary emissive material such as alumina (Al_2O_3) or magnesium oxide (MgO). Finally, to increase the detection efficiency and decrease the probability of ion feedback, the pores in an MCP have bias angles between 8° and 20° , with respect to the plane normal.

2.2.2 MCP properties

The multiplication factor or gain G is most strongly a function of the applied voltage V and the channel's aspect ratio α . The gain-bias characteristics can be approximately described by treating the MCP as a discrete stage electron multiplier with a fixed number n of stages or dynodes ($n = \alpha/\beta$, where β is a dimensionless proportionality constant) as it was done in a model proposed by Eberhardt [24]. This assumption leads to the following general expression:

$$G = \delta_1 (V/nV_c)^{k(n-1)} = \gamma [(nV_{pk} + V)/nV_c]^k (V/nV_c)^{k(n-1)}. \quad (2.6)$$

δ_1 the effective gain at the first impact, V_c is the so-called first crossover potential (the minimum potential for unity secondary emission ratio), eV_{pk} is the input energy of the photoelectrons, γ is the effective electron acceptance area ratio, and k is a constant coefficient related to the curvature of the secondary emission function $\delta(V_z)$. It should be noted that channel saturation effects are not considered in Equation 2.6. Assuming the energy eV_{pk} at the first impact to be much larger than the energies inside the channels, the equation can be simplified to show linear proportionality between $\log(G)$ and $\log(V)$:

$$\log(G) = k(n-1)\log(V/nV_c) + \log\gamma(V_{pk}/V_c)^k \quad (2.7)$$

If $\log(G)$ is plotted vs $\log(V)$ the data will show a straight line with a slope equal to $k(n-1)$ [24], [25].

Although the discrete dynode model seems to work well under some circumstances, some assumptions are unlikely to be valid. For example, the model assumes the number of dynodes to be independent of the applied voltage. Monte- Carlo simulations can be used to get a more accurate model of the MCP behavior [26], [27].

The maximum detection efficiency of MCPs is limited by the ratio between the channel open area to the entire effective area of the MCP called open area ratio (OAR). This value ranges between 40 %- 80 % for most commercial MCPs. Channels with a funnel-shaped opening have been fabricated by Hamamatsu and can achieve an OAR of around 90 % as shown in Figure 2.8. For the detection of photons, a photocathode has to be put above the MCP. Therefore, the photons' detection efficiency is limited by the quantum efficiency (QE) of the photocathode.

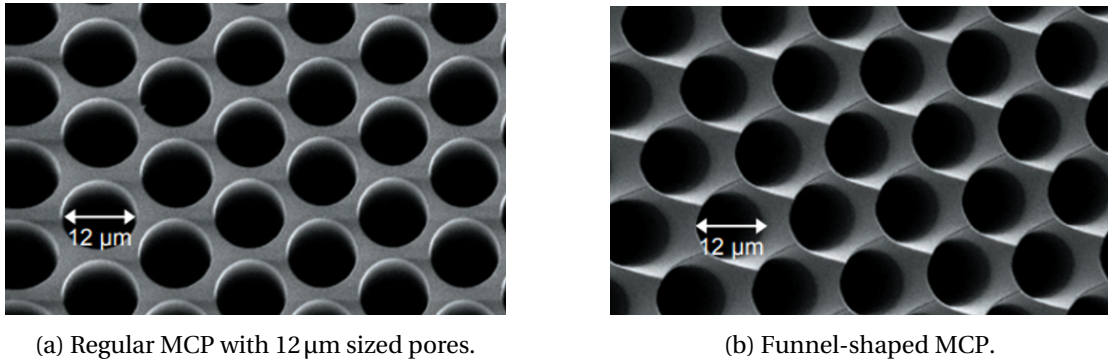


Figure 2.8: Surface view of a conventional and a funnel-shaped MCP (Pictures taken from <http://www.hamamatsu.com>).

The main advantages of MCPs over other detectors, like SiPMs, lies in their high spatial and temporal resolution and low dark count rates. The spatial resolution is only limited by the distance between the pores (typically 6 μm-12 μm). The time resolution depends on the channel diameters and can reach between 10 ps and 25 ps for 5 μm to 10 μm pores [28], [29]. The dark count rate depends only on spontaneous emission of the photocathode, influenced by the work function and temperature; typical rates are between 10 Hzcm² and 10 kHzcm² [30].

2.2.3 Limitations

One main limitation of microchannel plates is associated with saturation effects of the channel walls. When the multiplied current signal increases up to a significant fraction of the strip current, lost charges cannot be fully replenished between successive pulses; hence the channel gain decreases. This loss of linearity due to saturation effectively limits the maximum count rate of MCPs [31]. Another problem arises when using MCPs in combination with photocathodes. During the multiplication process inside the channels, atoms and molecules of the residual gas can get ionized. They are then accelerated towards the photocathode causing physical damage and lowering its QE over time [32]. It could be demonstrated that an ultra-thin layer of either Al₂O₃ or MgO, deposited by ALD improves the lifetime by preventing the glass substrate from outgassing and hence reducing the ion flux hitting the photocathode [33].

However, adverse effects such as an increased magnetic field sensitivity [34] as well as low current saturation levels and high gain recovery times were observed in ALD-coated MCPs [35]. Another drawback of MCPs lies in their fabrication process. For the assembly of MCPs batches of glass fibers are fused together. Despite many improvements in the MCP fabrication over the last years [36], it remains a costly process that is not easily scalable and with limited flexibility in channel geometries.

2.2.4 MCP characteristics summary

Table 2.2 gives an overview of the numerical values for the main properties of conventional MCPs.

Table 2.2: Properties of conventional MCPs

Property	Value	
Aspect Ratio	40- 80	
Channel Diameter	Typical: 6- 10 μm	Minimum: 2 μm
Gain	Single: $10^3 - 10^4$	Stacked: $10^6 - 10^8$
Open Area Ratio	Typical: 40- 80 %	Maximum: 90 % (Funnel opening)
Strip Current	12- 13 μAcm^{-2}	
Timing Resolution	10- 25 ps	For 5-10 μm channels
Spatial Resolution	6- 12 μm	
Dark Count Rates	10 Hzcm^{-2} - 10 kHzcm^{-2}	

2.3 Amorphous silicon based microchannel plates

The idea to fabricate MCPs out of hydrogenated amorphous silicon was first investigated in 2010 [37] with the proof of concept being presented in the following years [38], [39]. They offer unique advantages over conventional glass MCPs and may potentially overcome some of their limitations. The following section will provide an overview of the working principle and the current state-of-the-art of AMCPs.

2.3.1 AMCP working principle

The basic working principle of AMCPs is very similar to the one presented for glass-based microchannel plates. An incoming particle will interact with the channel walls and produce electrons through secondary electron emission. An applied electric field accelerates the electrons down the channel. Each collision releases more secondary electrons to produce an avalanche inside the channels. A thick a-Si:H layer (between 40- 100 μm) represents the main component of an AMCP. Compared to conventional MCPs, the current to replenish the lost charges during the multiplication phase flows directly through the bulk material. Conductivity of amorphous silicon layers can be varied over several orders of magnitude by doping with either phosphine or boron [17]. The current flowing inside the stack can thus be higher than usual strip currents in MCPs which means that charge replenishment time may be shortened. The detector is directly grown on top of a metal anode. An intermediate electrode connected to the ground is additionally introduced in the structure to evacuate the leakage current. The bottom anode is isolated from this electrode by a 2 μm thick a-Si:H layer called the decoupling layer. The channels are etched inside the a-Si:H by deep reactive ion etching (DRIE). A bias voltage can be applied to the top metal electrode. More details on the exact fabrication process are given in Chapter 5. Figure 2.9 summarizes the basic structure of an AMCP and its working principle.

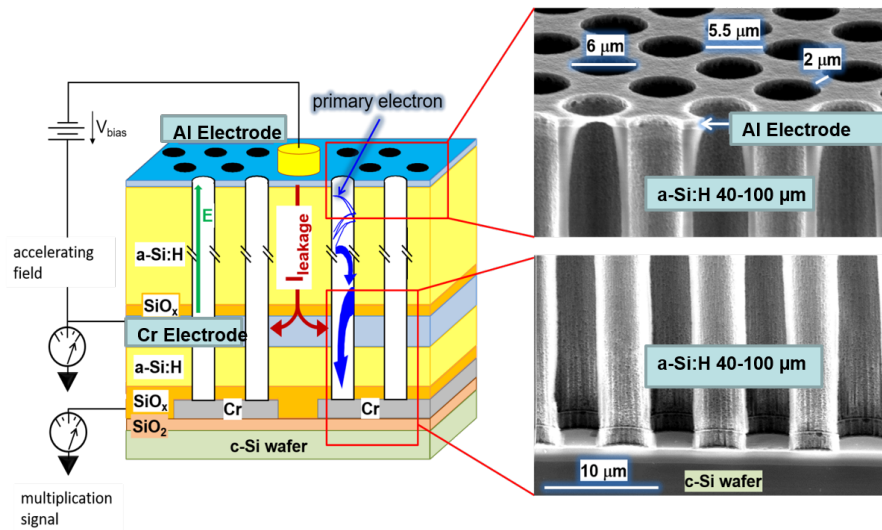


Figure 2.9: Schematic representation of the AMCP working principle. An incident particle strikes one of the channel walls, creating secondary electrons. An intermediate chromium electrode is connected to the ground and isolated from the bottom anode by the decoupling layer. A bias voltage is applied between the top electrode and the intermediate electrode.

Secondary emission

Both MCPs and AMCPs function by secondary electron emission (SEE) inside the pores. SEE describes the release of electrons from a material when a primary particle, either an electron or another charged particle, impinges on the material's surface. These electrons are called secondary electrons. The process of SEE was first observed in 1902 [40], and more detailed descriptions of the mechanism were provided a few years later [41]. When an electron reaches a surface, it can either be elastically scattered, inelastically scattered, or absorbed into the material. Both inelastic scattering and absorption can lead to the production of secondary electrons inside the material. These electrons then travel towards the surface, and if their energy is higher than the electron affinity E_A of the material, they escape over the vacuum barrier. The ratio between the produced secondary electrons per impinging primary particle, SEY, depends on the energy and incident angle of the incoming particle as well as some material related parameters, such as the work function, the escape depth of the particles, and the energy losses during their movement inside the material. The secondary electron yield has a maximum at incoming energies between 100- 800 eV for most elements, whereas it tends to be a bit higher for compounds [42],[43]. The dependence of the SEY δ on the incoming angle θ , with respect to the surface normal, is most accurately described by [44]:

$$\delta(\theta) = \delta_0(\cos(\theta))^{-n}, \quad (2.8)$$

where δ_0 is the SEY at normal incidence and n is a constant depending on the material (its value is around 1.3 for lighter elements, and around 0.8 for heavier ones [45]). The higher the incident angle θ , the more energy is deposited at a shallower depth, increasing the escape probability of the produced secondary electrons. The mean escape depth has been measured to be around 0.5- 1.5 nm for most metals and 10- 20 nm for insulators [43]. It should be mentioned that the surface morphology drastically affects the amount of produced secondary electrons. Low-energy electrons, which would not be able to escape from a flat surface, can escape from an inclined plane of a rough surface. This causes an increase in the SEY [46],[47]. On the other hand, shading effects can significantly reduce it [48]. The initial kinetic energy of the produced secondary electrons is very low, in most cases only a few electronvolts. Their maximum energy has been defined to be at around 50 eV [49]. Many measurements for the SEY exists for different kind of materials [42]. Large SEY, between 5-7, are exhibited for materials with a wide-band gap such as NaCl or LiF. This is because energy losses are less pronounced in larger band gap materials, and escape depth becomes bigger [50]. Some measurements exists in the literature for the SEY of a-Si:H [51], [52].

Its average value tends to be slightly larger than that of crystalline silicon, most probably due to hydrogen bonding, which was shown to increase the SEY because it produces a negative electron affinity [50], [53]. However, these measurements usually cover energy ranges above 100 eV. The energy of the electrons inside the channels rarely exceeds 100 eV due to the low initial energy of the produced secondary electrons and the short traveling distances between collisions. Additionally, most theoretical models are unreliable for these low-energy electron-matter interactions. The total SEY for low incident energies was measured using a calibrated electron analyzer [54]. Figure 2.10 shows the total yield as a function of incident energy and for four different angles of the incoming particle. As for conventional MCPs, one way to increase the number of secondary electrons and hence the multiplication factor of AMCPs is by depositing materials with a high SEY on the inner wall by ALD.

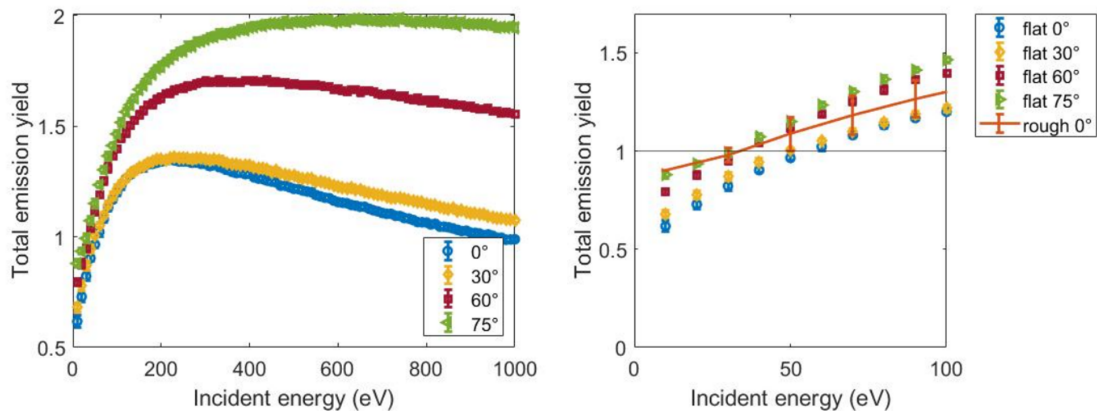


Figure 2.10: Measured total emission yield of an a-Si:H sample for different incident angles and the crossover energy (minimum energy to have a yield equal to one) [54].

2.3.2 Advantages and disadvantages of AMCPs

The main advantage of AMCPs over their conventional counterpart is that they can be directly fabricated on top of electronic circuits, realizing monolithic detectors. The low fabrication temperatures (below 220 °C) mean that fabrication can be achieved on almost any type of substrate and over large areas. This minimizes the detector dead area and improves both the spatial and temporal resolution of the detector. Vertical integration of thin-film amorphous silicon detectors on top of complementary metal–oxide–semiconductor (CMOS) readout electronics has already been demonstrated [55]. Another advantage lies in the bulk resistivity of a-Si:H, which is large enough to sustain a high bias voltage and small enough to provide fast charge replenishment. As mentioned earlier, the layer resistivity can be easily varied over several orders of magnitude by doping. This opens the possibility of optimizing the electric field along the channels to counteract saturation effects. Finally, the fabrication of AMCPs employing micromachining techniques allows for a fully customized channel geometry and a much cheaper fabrication process in comparison to glass MCPs.

Channels with diameters down to $1\mu\text{m}$ can be realized. Small channel diameters tend to produce the fastest output pulses [56] and improve the pulse height distribution [57]. The main limitation of AMCPs lies in the fact that they need to be fabricated on a substrate and are not stand-alone structures. The need for a substrate eliminates the possibility of stacking several AMCPs on top of one another to increase the gain.

2.3.3 Current state-of-the-art

Previous generations of AMCPs were already available at the beginning of this thesis. A microcrystalline silicon ($\mu\text{c-Si}$) based intermediate electrode was introduced during the 3rd generation of AMCPs [39]. Due to the implementation of this electrode, the anode signal could be decoupled from the leakage current flowing through the stack. The residual leakage current on the anode decreased by about five orders of magnitude to about 2 pAmm^2 , and the signal originating from the multiplication inside the channels could be successfully measured. Figure 2.11 shows the change in the anode signal with the introduction of the grounded intermediate electrode.

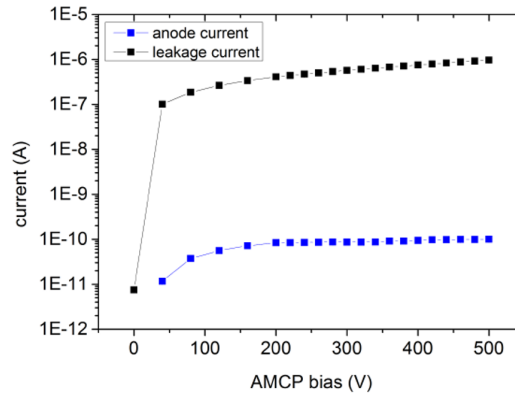


Figure 2.11: Leakage current as a function of the applied bias voltage for both the intermediate electrode and the anode. Measured on a 24 mm^2 area [19].

These AMCPs have layer thicknesses between $60\text{--}90\mu\text{m}$ and minimum channel diameters of around $6\mu\text{m}$. A maximum gain of about 45 was measured for an AMCP with an aspect ratio of 12.5:1. The first detector with a 5 nm ALD deposited wall coating of Al_2O_3 was fabricated and yielded a gain of 80 for the same aspect ratio. The measurements are shown in Figure 2.12.

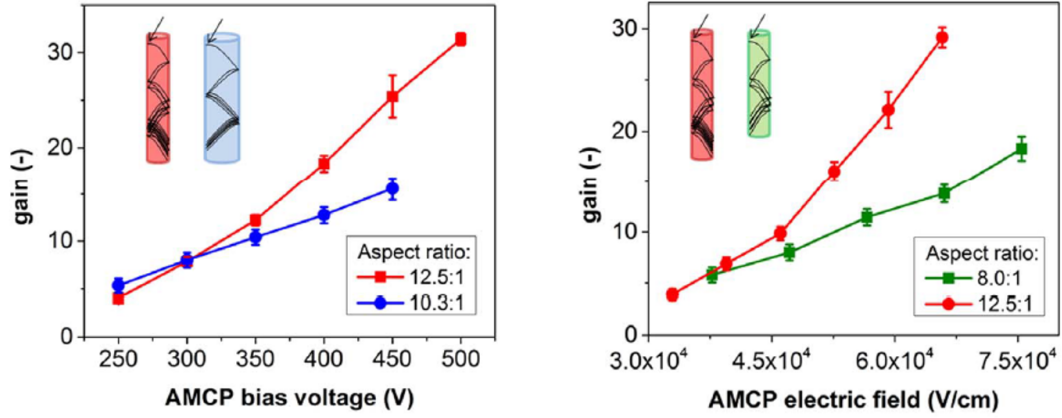


Figure 2.12: Measured gain versus applied bias/electric field for AMCPs with different aspect ratios [39].

After this first proof of concept, the fabrication process was further optimized. Higher aspect ratios of the channels could be realized by the use of a metal mask during the etching of the channels and use of an advanced DRIE equipment [54]. These samples have channel diameters down to $3\mu\text{m}$ and aspect ratios up to 22, as shown in Figure 2.13. Although no signal could be measured from those samples due to a too high leakage current, the improved etching process paved the path for detectors with aspect ratios close to those of conventional MCPs.

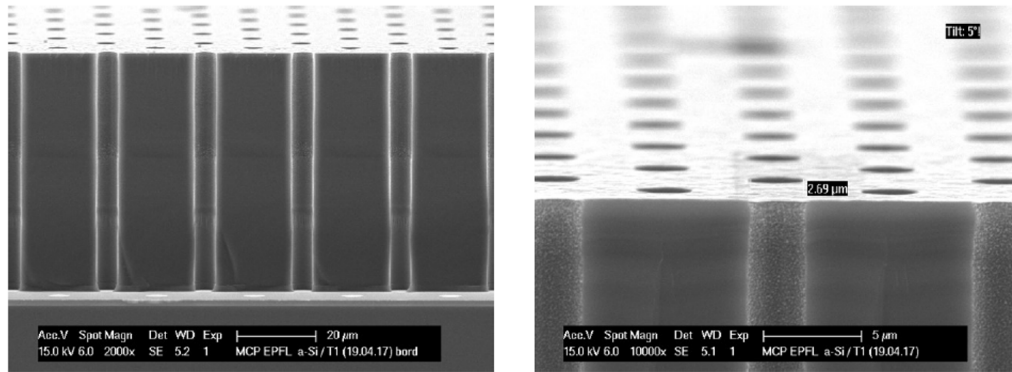


Figure 2.13: scanning electron microscope (SEM) images of etched channels with a top chromium mask and channel diameter down to $3\mu\text{m}$ [54].

3 Detectors for Time-of-Flight Positron Emission Tomography

3.1 Sinergia project overview

The further development of AMCPs is linked to the Sinergia project “MEMS based gamma ray detectors for time-of-flight positron emission tomography”. Within this project’s scope, a gamma-ray detector is being developed that will ultimately be used in TOF-PET systems. A key aspect of this novel detector is the use of Cherenkov radiation instead of conventional scintillation photons. Cherenkov light is produced quasi-instantaneously with the absorption of a 511 keV gamma photon. This approach hence significantly improves the time resolution and ultimately the signal-to-noise ratio (SNR) of the system. After the initial absorption of the gamma photon in a Cherenkov radiator, the resulting Cherenkov photons will then reach a highly efficient photocathode, placed on the sides of the radiator, to produce photoelectrons that will then be detected by an AMCP. The AMCP itself will be directly integrated with the underlying electronic readout. Both AMCP and the electronic components are going to be placed inside a vacuum-sealed tube. Utilizing this architecture aims to achieve a coincidence time resolution (CTR) of 10 ps. This chapter discusses the different components of the detector and the main challenges involved in more detail. Figure 3.1 shows the schematic architecture of the envisioned sensor.

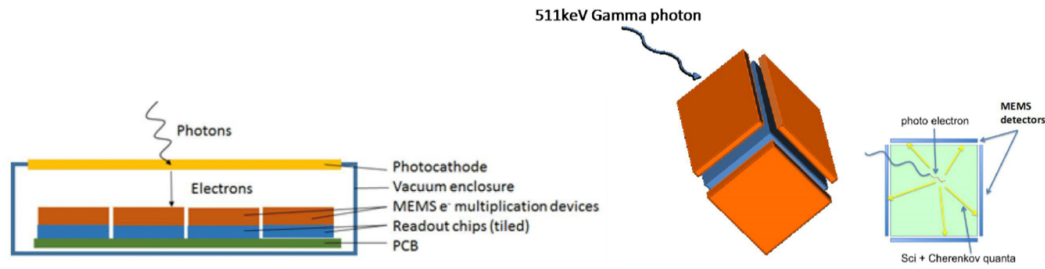


Figure 3.1: Schematic representation of the gamma-ray detector architecture. An incoming gamma-photon is absorbed in a Cherenkov radiator, causing the release of several Cherenkov photons that then reach a photocathode. The resulting photoelectrons are eventually detected by the AMCP and the readout electronics.

3.2 Positron emission tomography

3.2.1 Working principle

PET is a biomedical imaging technique based on detecting radiotracers inside the body. PET scanners are commonly used in hybrid devices with either X-ray computerized tomography (CT) or magnetic resonance imaging (MRI) to combine molecular and anatomical imaging [58]. Their main applications lie in clinical diagnostic imaging, most often for oncologic indications, as well as pre-clinical imaging [59]. The early versions of today's clinical PET systems were developed in the 1970s [60]. In Figure 3.2 the main steps to acquire a PET image are illustrated. In the first step, the patient, either a human or an animal, is injected with a solution containing a radiotracer. These radiotracers are metabolically active substances labeled with a positron-emitting radionuclide. Labeling biomarkers, biochemicals, or pharmaceuticals can be done without disturbing their biological function [61]. Nowadays, many available radiotracers produce image contrast related to metabolic pathways, underlying physiology, or molecular targets. One of the most commonly used for the early detection of cancerous cells is fluorine-18 fluorodeoxyglucose (FDG). FDG is an analog of glucose and is used as a tracer of glucose metabolism. It is transported into the cells by glucose transporters but is not metabolized, a process called metabolic trapping. Abnormally metabolizing tumor cells can be identified by the increased uptake and accumulation of FDG [62]. Once inside the body, the radioactive isotope will eventually decay, releasing a positron. The emitted positrons travel a short distance, called the positron range, before annihilating with an electron of the surrounding tissue. For fluorine-18, the travel distance is usually around 0.6 mm but can reach several millimeters for other radionuclides [63]. Another factor to consider is that the positron and electron are not entirely at rest when annihilation occurs, causing a slight deviation of around 0.2° in the emitting angle between the two photons. This effect, called non-collinearity, leads to a location error that increases with the distance between the detector units [64].

Eventually, the annihilation leads to the release of two back-to-back gamma photons with energies of 511 keV. They can then be detected in coincidence mode, and an image reconstructed by the use of reconstruction algorithms [65]. About 10^7 to 10^8 decay events are detected to reconstruct a PET image. The annihilation photons can also scatter inside the body, causing a loss of energy and a change in direction. These are called scattered events. Besides that, there are also random events when two unrelated photons strike the detectors simultaneously, producing a false coincident detection. Distinguishing true events from scattered and random coincidences is not possible, but several algorithms exist to partially correct for them to improve the PET image quality [66]. Lastly, the two photons will arrive at the detectors with a slight difference in time depending on the distance of the annihilation point to the detector unit. In TOF-PET, this difference is measured, which significantly improves the SNR of the detector.

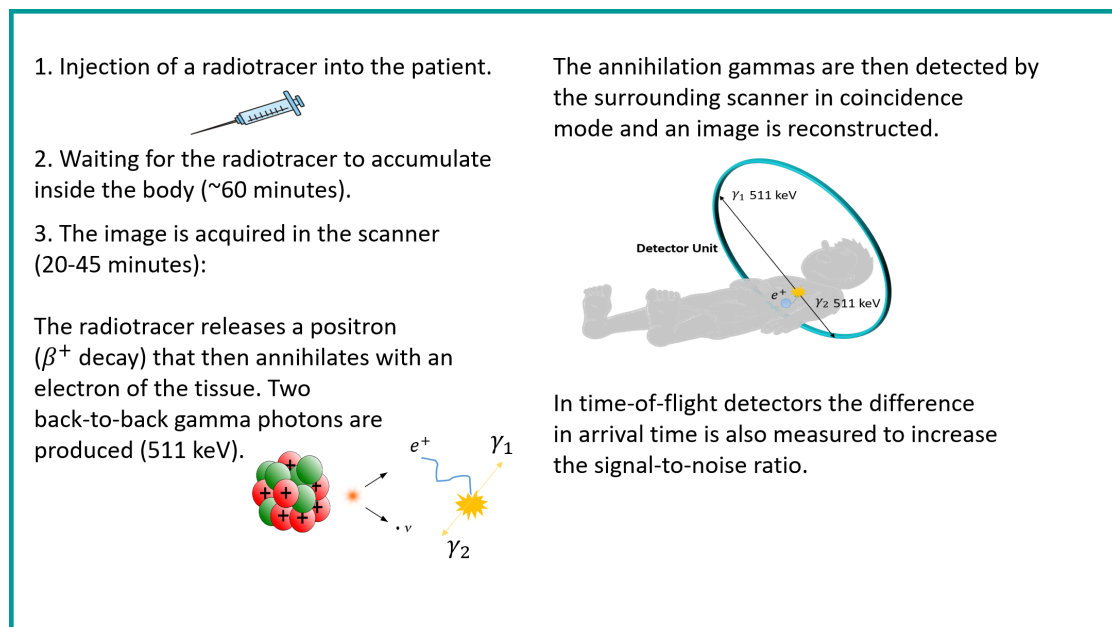


Figure 3.2: Basic working principle of positron emission tomography. A patient is injected with a radioactive tracer that accumulates in certain regions inside the body. The radioactive isotope eventually decays, emitting a positron. The positron annihilates with an electron of the tissue, releasing two back-to-back gamma photons in the process.

A low SNR negatively affects the possibility of detecting small amounts of radiotracers. In a first-order approximation, the SNR depends on the number of detected events n ,

$$SNR \propto \sqrt{n} \approx kAG\epsilon^2 T \quad (3.1)$$

where A is the amount of activity in the field of view of the scanner, G the average geometric coverage, ϵ the efficiency of detecting an incident 511 keV photon, T the acquisition time, and k a patient-specific factor taking into account attenuation and scattering of the photons inside the body. The relationship between SNR and time resolution Δt is given by [67]:

$$SNR \propto \sqrt{D/\Delta t} \approx \sqrt{\frac{k'AG\epsilon^2 T}{\Delta t}} \quad (3.2)$$

where k' includes the previously mentioned factor k but also the diameter of the subject and factors relating to the reconstruction algorithm. Conventional detection units consist of a scintillator coupled to a photodetector. The incoming gamma photon interacts inside the scintillator, depositing some or all of its energy and producing a flash of light. The amount of photons produced depends on the scintillation material and is proportional to the deposited energy. These scintillation photons are then detected by photodetectors, most commonly SiPMs, leading to an electronic pulse to signal the detection of an event. Detection of two events simultaneously at opposite detectors represents a coincident event [68]. As can be seen from Equation 3.2 to increase the SNR one has to either lengthen the scan time, improve the detection efficiency or improve the time resolution, which will be the main focus in the following discussion. Most commercial PET systems nowadays have time-of-flight capabilities. They are integrated with either CT or MRI to form hybrid diagnostic instruments [69] with some reaching a coincidence time resolution of 210 ps full width at half maximum (FWHM) [70]. There is a push towards reaching a CTR of 10 ps to increase the SNR further.

3.3 Cherenkov radiation

In a scintillator, the initial absorption of the gamma photon will usually produce several thousands of scintillation photons (32000 photons/MeV for lutetium yttrium oxyorthosilicate (LYSO) and 8500 photons/MeV for bismuth germanium oxide (BGO) [71]). Scintillation photons are produced by the recombination of electron-hole pairs in the scintillator. The number of produced photons follows Poisson statistics, whereas their emission times follow an exponential distribution. After their emission, the scintillation photons travel through the material, where they are either absorbed, scattered, or ideally directly reach the photodetector. The loss of photons in the scintillator, their variable propagation time, and the randomness of their creation together impose an upper limit of achievable timing resolution when using scintillation-based detectors. An alternative approach is to make use of Cherenkov radiation rather than scintillation. Cherenkov light was first observed in 1934 by P.A. Cherenkov and S.I. Vavilov [72]. This form of radiation is produced when a charged particle moves in a medium with a speed v faster than the phase velocity of light in this medium ($v > c/n$), with n being the refractive index. An incoming gamma photon produces electrons (with an energy of 511 keV or less) either by Compton scattering or the photoelectric effect. A charged particle moving in a dielectric material will polarize the medium along its track. If the particle is slow, the resulting radiation from the displaced electrons returning to their original position is not observed due to destructive interference. If, however, the particle's velocity is faster than the phase velocity of light in the medium, the wavelets are in phase with one another, and coherent radiation can be observed. The photons are released in a cone relative to the moving particle. The angle of the cone θ is related to the particle velocity v through:

$$\cos \theta = \frac{1}{\beta n}, \quad (3.3)$$

where c is the speed of light and $\beta = v/c$. The amount of produced light W per traveled path l is described by the Frank-Tamm formula:

$$\frac{dW}{dl} = \frac{e^2}{c^2} \int_{\beta n > 1} \omega \left(1 - \frac{1}{\beta^2 n^2} \right) d\omega, \quad (3.4)$$

where e is the charge of the particle and ω is the angular momentum. From Equation 3.4 it can be seen that the spectrum is continuous and by neglecting dispersion (meaning $n = \text{continuous}$) follows:

$$\frac{dW}{d\omega} \propto \omega \rightarrow \frac{dW}{d\lambda} \propto \frac{1}{\lambda^3}, \quad (3.5)$$

which is why Cherenkov light appears bluish-white in color [73], [74].

Because Cherenkov light is produced quasi-instantaneously with the interaction of the incoming gamma, much faster timing properties can be achieved compared to luminescence processes with intrinsic decay time constants between tens to hundreds of nanoseconds.

However, one of the main drawbacks in utilizing Cherenkov radiation is the relatively low number of photons that are produced for each 511 keV photon interaction, typically only 10-20 in common Cherenkov radiators. A material used as a Cherenkov radiator should have a high stopping power for the initial 511 keV gamma and good transmission for light in the blue to near ultraviolet (UV) region [75]. Various geometries and materials are being studied within the framework of another thesis in this project. A short summary of the obtained results is given here. Monte-Carlo simulations have been performed using the geometry and tracking (GEANT4) toolkit. These simulations employed a coincidence setup of two distant detector elements with a point source generating back-to-back 511 keV gammas in the center. Two different potential geometries are being investigated- a small 3 mm^3 crystal with a single side readout and a 25 mm^3 crystal cube with readout on all six sides. While a single detection of a Cherenkov photon is sufficient in the small crystal for the identification of a gamma interaction, reconstruction is needed in the cube geometry. The best timing resolution can be achieved using a small lead fluoride (PbF_2) crystal. PbF_2 is a pure Cherenkov radiator (meaning no additional scintillation photons are produced) with an average photon yield of 20.3 per gamma interaction. Figure 3.3 shows the single photon timing resolution (SPTR) as a function of the intrinsic timing resolution of the photosensor. For a photon detection efficiency of 30 % and a time resolution of the photosensor of 10 ps, a SPTR of ~ 11 ps was simulated, resulting in a CTR of 14.4 ps. Another material worth mentioning is BGO. BGO is a low-cost material that used to be a standard scintillator in previous generations of PET scanners. It later got replaced by lutetium-based crystals due to their better timing and energy properties. The disadvantages of lutetium-based crystals present themselves in the form of lower stopping power and intrinsic radioactivity. In contrast to PbF_2 , BGO produces both Cherenkov and scintillation photons. This hybrid approach allows for exploiting the excellent timing properties of the prompt photons while still providing energy resolution from the scintillation radiation.

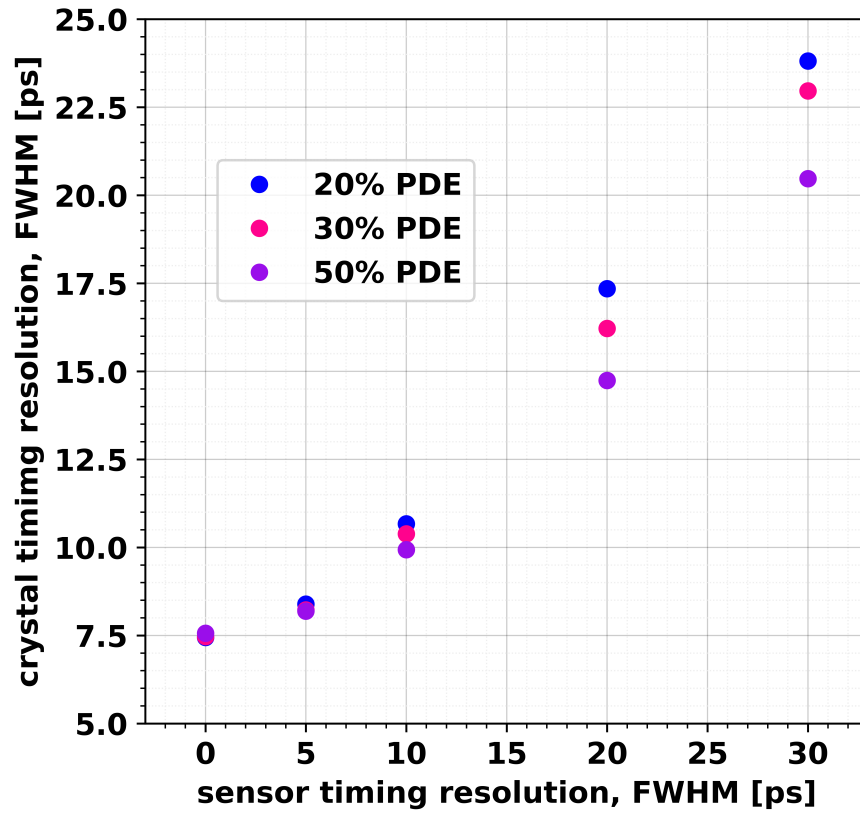


Figure 3.3: SPTR in a $3.0 \text{ mm} \times 3.0 \text{ mm} \times 3.0 \text{ mm}$ crystal as a function of the photosensor intrinsic timing resolution for different photon detection efficiencies (PDEs) (Courtesy of Sofia Forostenko).

3.4 AMCPs as photodetectors

After the initial detection of the 511 keV gamma in the radiator, the resulting photons (either Cherenkov or scintillation) need to be detected by a photodetector. The time resolution of the photodetector needs to be as high as possible to exploit the fast timing from the Cherenkov radiator fully. In this project, the photons will be detected by amorphous silicon based microchannel plates in combination with a highly efficient photocathode. AMCPs are ideal for this application as their excellent timing properties have already been shown in simulations [76]. A time resolution below 10 ps for a single electron input could be demonstrated. As mentioned in Chapter 2, the possibility of directly fabricating the AMCPs on top of the readout electronics further enhances timing and spatial resolution.

Two main challenges need to be overcome for this detector architecture to succeed. Firstly, the channel gain must be high enough for a single electron input to produce a readable signal for the electronics. For a modern CMOS low-noise amplifier (LNA), this means a multiplication factor of at least 1000. Previous generations of AMCPs have shown gain values below 100 for aspect ratios up to 12.5 [39]. Simulations with a Monte-Carlo-based model support the evidence that high enough multiplication factors can be reached by increasing the aspect ratio of the channels to around 30 [76]. Figure 3.4 shows a simulated gain of 1944 for a channel aspect ratio of 30.

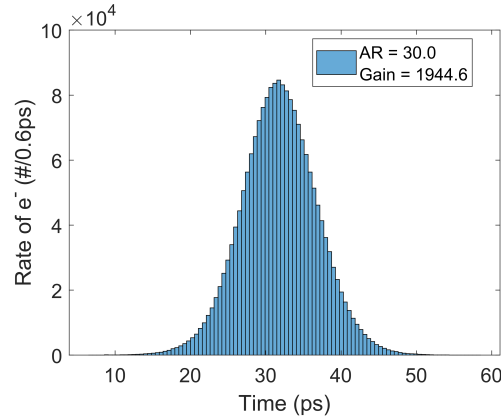


Figure 3.4: Simulation of the multiplication gain in a 60 μm long channel with 2 μm diameter. The graph shows the cumulative arrival time of 1000 incident electrons. The average gain was shown to be 1944 [76].

Secondly, due to the low number of produced Cherenkov photons (~ 20 per gamma interaction), the detection efficiency of the AMCP needs to be close to 100 %. The detection efficiency of the AMCPs is primarily given by the OAR of the channels. A funnel-shaped channel opening needs to be implemented to achieve this high efficiency. The quantum efficiency of the implemented photocathode limits the total detection efficiency for an incoming photon. A highly efficient photocathode, manufactured by "Photonis", will be used for this project.

Figure 3.5 shows the spectral response of different available photocathodes. The quantum efficiency exceeds 30 % at the maximum response. The photocathode Hi-QE UV offers superior detection to 330 nm, while the Hi-QE blue one provides improved response up to 400 nm. Hi-QE green is optimized for the range from 400-550 nm and Hi-QE Red from 400-900 nm. The Hi-QE blue photocathode is preferred for the detection of Cherenkov radiation. The dark count rate of these photocathodes is typically around 50 Hz/cm² at room temperature.

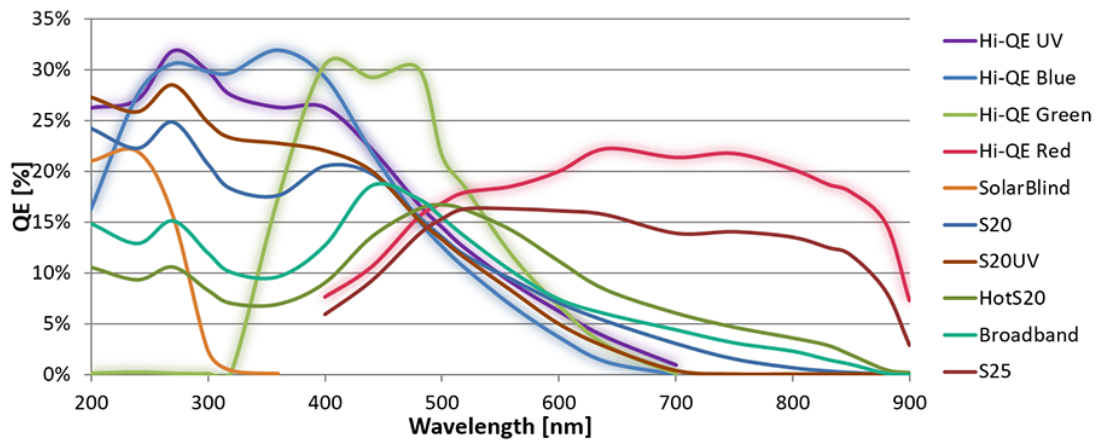


Figure 3.5: Quantum efficiency of different photocathodes for a wavelength range of 200-900 nm. The maximum achievable quantum efficiency is around 30 % (Image from <http://www.photonis.com>).

SiPMs are the standard detectors used in today's conventional PET imaging systems. SiPMs are an array of avalanche photodiodes (APDs) operated in Geiger mode. They offer single-photon sensitivity, and their time resolution has been massively improved in recent years, reaching a single photon timing resolution as low as 20 ps in recent developments [77]. Their main limiting factors are a high dark count rate, up to a few hundred kHz/mm² (depending on temperature, overvoltage, and size of the active area), cross-talk between the pixels and a rather large dead area around individual microcells. Larger microcells can be implemented to maximize efficiency. This will, however, decrease the achievable time resolution due to the increased capacitance.

3.5 Summary

In this chapter the main ideas and objectives of the Sinergia project “MEMS based gamma ray detectors for time-of-flight positron emission tomography” were outlined. The main challenges concerning the AMCP development lie in achieving the needed gain and detection efficiency to successfully detect the produced Cherenkov photons.

4 AMCP Simulations

4.1 Modeling of AMCPs

This section presents the theoretical framework of AMCP modeling. The SEE process governs the response of an AMCP to an incoming electron. What makes the modeling of AMCPs challenging is the low energy interactions inside the channels, as most models describing SEE and scattering effects of electrons were developed for higher energies of the primary particles (>100 eV). For low-energy interactions like the ones encountered inside the AMCP channels, the validity of these models becomes questionable. Describing scattering events in the low energy range remains challenging as the surface morphology becomes more critical. Additionally, there exists a lack of experimental data in this energy range, making existing theories mostly an extrapolation of higher energy interactions. A rather simple model proposed by Eberhardt can be used to make rough predictions about the achievable gain of AMCPs and was already shortly introduced in Chapter 2. A probabilistic model developed within the scope of another thesis [78] is described in the first part of this chapter. Afterward, the implementation of this model into a FEM model using the COMSOL® Multiphysics environment is described.

4.1.1 Monte-Carlo Model

A Monte-Carlo based model developed to describe the behavior of AMCPs is used as a foundation for the simulations presented in this chapter. The full details of the model can be found in previous publications [78], [76]. This section summarizes the main ideas to provide the context for the finite element method model described in the next section. Unless otherwise mentioned, all presented equations and fitted values are taken from [76].

Elastic backscattering probability

An incoming electron can either be elastically backscattered, inelastically backscattered or absorbed for each collision. For every event, elastic backscattering and the creation of secondary electrons are mutually exclusive. The probability of a particle to be elastically backscattered η_e depends mainly on the incident energy E_{In} and the incident angle θ_{In} (relative to the surface normal) of the primary particle. Electron emission measurements at low incident energies were used to find a formulation for the backscattering probability. For $\theta_{In} < 85^\circ$, the angular dependency was negligible in the analyzed data and η_e can be calculated by the following empirical formula:

$$\eta_e(E_{In}) = a \cdot \exp(-b \cdot E_{In}) + c \quad \text{for } \theta_{In} < 85^\circ, \quad (4.1)$$

where a, b and c are constant fitting parameters. Their numerical values for a-Si:H, Al_2O_3 and MgO are given in Table 4.1 at the end of this section. If the particle is elastically scattered the radial part of its velocity is reversed and its kinetic energy remains unchanged $E_{BS} = E_{In}$. For incident angles above 85° a theoretical model presented by Cazaux [79], shown in Equation 4.2, was used to calculate the elastic backscattering probability as the angular dependency becomes more prominent at high incident angles and no measurements were available for this range:

$$\eta_e(E_{In}, \theta_{In}) = \frac{\left(1 - \sqrt{1 + (\chi / (E_{In} \cos^2 \theta_{In}))}\right)^2}{\left(1 + \sqrt{1 + (\chi / (E_{In} \cos^2 \theta_{In}))}\right)^2} \quad \text{for } \theta_{In} \geq 85^\circ, \quad (4.2)$$

where χ represents the electron affinity of the material. Figure 4.1 shows both the fitted backscattering probability from Equation 4.1 as well as the one found by Cazaux (4.2) for an incoming particle energy between 0 eV to 1000 eV and two different incident angles.

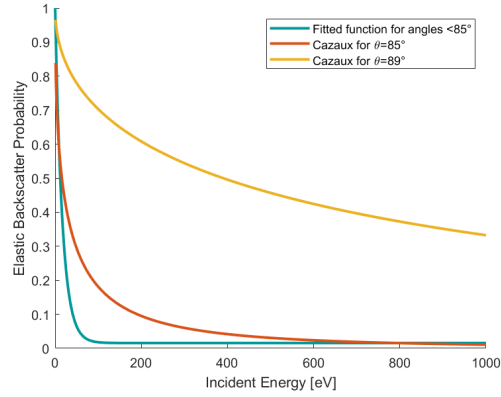


Figure 4.1: Plotted backscatter probability for a-Si:H for an incident energy between 0 eV and 1000 eV according to Equation 4.1 and the model in 4.2 for two different incident angles.

Secondary emission yield

If the electron is not elastically backscattered, it will enter the material where it can be inelastically backscattered, produce secondary electrons or be absorbed without leading to the emission of any electrons. The expected value for the secondary emission yield $\delta(E, \theta)$ as a function of the incident angle θ_{In} and the energy of the primary particle E_{In} is calculated using an empirical model proposed by Vaughan [80]:

$$\delta(E_{In}, \theta_{In}) = \delta_m(\theta_{In}) \left(\frac{E_{In}}{E_m(\theta_{In})} \exp \left[1 - \frac{E_{In}}{E_m(\theta_{In})} \right] \right)^s, \quad (4.3)$$

where s is a positive shaping parameter chosen to best fit the experimental data. E_m and δ_m are defined as

$$E_m(\theta_{In}) = E_m(0) \left(1 + k \frac{\theta_{In}^2}{2\pi} \right) \quad \text{and} \quad \delta_m(\theta_{In}) = \delta_m(0) \left(1 + k \frac{\theta_{In}^2}{2\pi} \right). \quad (4.4)$$

$E_m(0)$ is the energy of maximum secondary yield $\delta_m(0)$ at normal incidence. The yield $\delta(E_{In}, \theta_{In})$ includes secondary electrons as well as inelastically backscattered electrons without distinguishing between the two of them. The values of $\delta_m(0)$, s and k have been fitted to best represent the experimental data, whereas $E_m(0)$ was extracted from the secondary yield measurements. The values found for a-Si:H, Al₂O₃ and MgO are all summarized in Table 4.1 at the end of this section.

Figure 4.2 illustrates the curves found for $\delta(E_{In}, \theta_{In})$ from Equation 4.3 for an energy range from 0 eV to 1000 eV and four different incident angles.

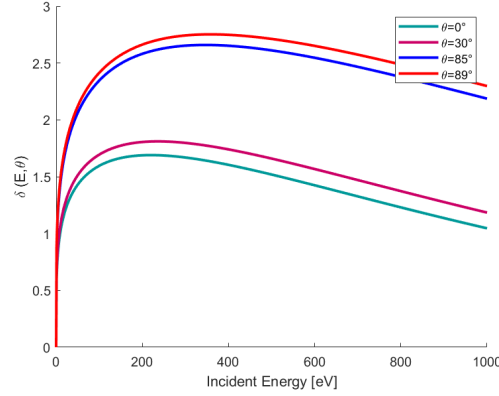


Figure 4.2: Plotted function for the expected secondary yield as a function of the incident energy according to Vaughan[80] with the fitted parameters from Table 4.1. Three curves for four different incident angles are shown.

The number of released particles is then picked from a Poisson distribution centered around $\delta(E_{In}, \theta_{In})$. This is done because the actual secondary electron emission is Poisson distributed. Whereas $\delta(E_{In}, \theta_{In})$ represents the average secondary yield for many electrons, the variation in yield for each individual electron must be considered to simulate the AMCP behavior for single particles accurately.

Emission energy

As mentioned before, the calculated yield includes electrons that were inelastically backscattered. When assigning the emission energy those electrons have to be considered since their energy can be much higher than those of the secondary electrons. The emission energy of secondary electrons is usually only a few electronvolts, depending on the energy of the incident electron. Secondary electrons are conventionally defined to have an energy below 50 eV. Released electrons with an energy bigger than 50 eV are considered to be inelastically backscattered. For simplicity the inelastic backscatter probability was roughly approximated by a factor 0.2, as it was done by [76], for an incident energy above 50 eV since the dependence on energy and angle is very small. Below 50 eV these electrons can not be distinguished from secondary electrons. In the case of an inelastic backscattering event, the energy of the outgoing particle is randomly chosen between 0 eV and $E_{IN} - 2$ eV, (an electron with an energy bigger than $E_{IN} - 2$ eV would be considered as elastically backscattered). In contrast to elastic backscattering, inelastic backscattering and secondary emission are not mutually exclusive. The particles that have not been backscattered are then considered "true" secondary electrons and their energies are assigned accordingly.

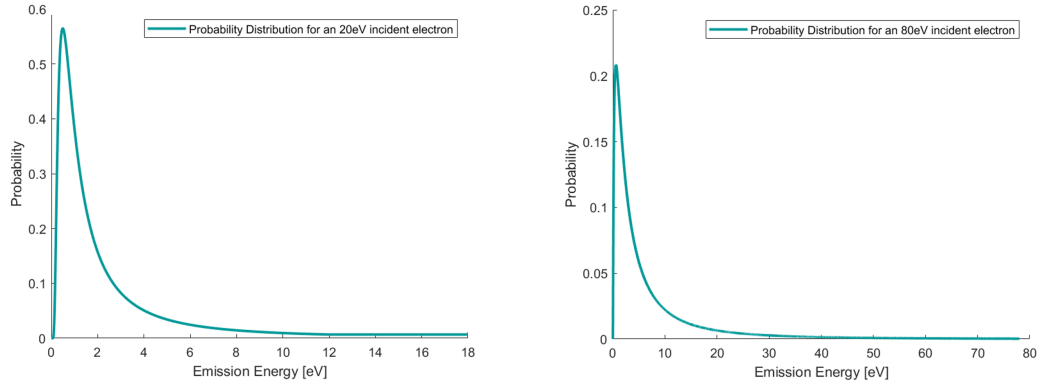
The energies of the secondary electrons are chosen out of a probability distribution that depends on the energy of the primary particle. For incoming energies below 25 eV a fit function is used to describe the emission energy (E_S) distribution $\partial\delta/\partial E_S$:

$$\partial\delta/\partial E_S(E_{In} \leq 25 \text{ eV}) = \frac{\Gamma((P_1 + P_2)/2) \cdot (P_1/P_2)^{P_1/P_2} \cdot E^{P_1/P_2-1}}{\Gamma(P_1/2) \cdot \Gamma(P_2/2) \cdot (1 + P_1/P_2 \cdot E)^{(P_1+P_2)/2}} \quad (4.5)$$

where $P_1 = 39 \cdot \exp(-E_{In}/68) + 111$ and $P_2 = 2$ are parameter describing the shape of the gamma function depending on the incident energy E_{In} . The energies of the secondary electrons are then picked from the distribution resulting from Equation 4.5. For incident energies higher than 25 eV, theoretical models for the emission energy distribution, like the one presented by Kruschwitz [27], fit well with the measurements and are used to calculate the emission energy. The probability distribution is given by:

$$\partial\delta/\partial E_S(E_{In} > 25 \text{ eV}) = C \exp \left[-\frac{[\ln(E_S/E_{MP})]^2}{2 \cdot \sigma^2} \right], \quad (4.6)$$

where the most probable energy (E_{MP}) and σ are chosen to best fit the data and C is a normalization constant. Their values are given in Table 4.1 at the end of this section. The resulting emission energy distributions are shown in Figure 4.3.



(a) Emission Energy Distribution $E_{In} = 20 \text{ eV}$

(b) Emission Energy Distribution $E_{In} = 80 \text{ eV}$

Figure 4.3: Calculated emission energy distribution for two different incident energies (20 eV and 80 eV). For incoming particles with an energy $\leq 25 \text{ eV}$ the fit function in Equation 4.5 is used to determine the emission energies. For higher energies the distribution given in Equation 4.6 is used.

Release angle

θ_{SE} , the emission angle relative to the surface normal is chosen between 0 and $\pi/2$ according to Lamberts cosine rule:

$$P(\theta_{SE}) = \frac{1}{\pi} (1 + \cos(2\theta_{SE})) \quad (4.7)$$

The azimuthal angle, φ_{SE} , is independent of this distribution and can take any value between 0 and 2π

$$P(\varphi_{SE}) = \frac{1}{2\pi}. \quad (4.8)$$

Model parameters summary

Table 4.1 summarizes all the parameters used in the current version of the Monte-Carlo model. Since these values have been fitted using a limited amount of measurement data their values are likely to be readjusted in the future. No emission spectra for MgO were available to date hence the same parameters as for Al_2O_3 were used to calculate the backscattering probability and the emission energy distribution.

Table 4.1: Simulation parameters used in the Monte-Carlo Model.
^a [81]

Parameter	a-Si:H	Al_2O_3	MgO
Backscattering Probability			
a	0.9845	0.987	0.987
b	0.06005	0.069	0.069
c	0.0155	0.013	0.013
χ	3.92 eV	1.35 eV	1.4 eV ^a
Secondary Yield Model[[80]]			
δ_m	1.65	2.5	4.8
E_m (eV)	220	310	514
k	1.63	0.45	1.67
s	0.23	0.45	0.69
Emission Energy Distribution			
E_{MP}	0.8 eV	0.7 eV	0.7 eV
C	513	12.3	12.3
σ	1.33	1.33	1.33

4.1.2 Finite Element Method Model

In this next part the implementation of the presented Monte-Carlo model into a FEM model is described. An early version of the model was already presented in previous publications [76] and has since been updated. The model was set up within the COMSOL Multiphysics® environment (Version 5.6). The main motivation behind this was to simulate the behavior of AMCP channels with non-standard geometries as the channel geometry can be easily adjusted within the COMSOL interface. The model uses the provided "Electrostatics" and "Particle Tracing" modules to calculate the trajectories of the electrons within the channels. A LiveLink™ for MATLAB® allows to incorporate customized functions written in MATLAB into the simulation. Although the main procedures are the same for both the original Matlab based Monte-Carlo model and the FEM model, some steps required alternative approaches due to some limitations within the COMSOL interface. In the following section, a step-wise explanation of the simulation procedure is provided. An example of a simulated geometry can be seen in Figure 4.4.

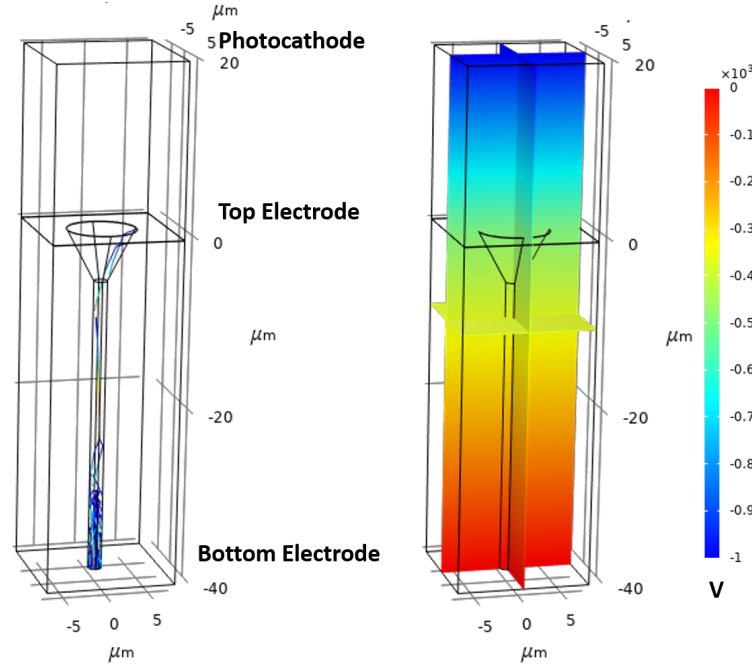


Figure 4.4: Geometry of the single channel model with a funnel-shaped opening and the trajectories of an electron avalanche (left) and the applied electric potential (right).

A single channel with a funnel opening on top is placed inside an a-Si:H block. The channel has a length of 40 μm and a lower channel diameter of 1.6 μm. The funnel has an upper diameter of 8 μm and reaches 6 μm deep. The photocathode is placed 20 μm away from the top electrode. The voltages on the photocathode ($V_{PC} = -1000$ V), the AMCP top electrode ($V_{Bias} = -500$ V), and the bottom electrode (0 V) are defined. All these values can be freely chosen at the start of a simulation.

The space inside the channel and on top of the a-Si:H block is defined to be a perfect vacuum. A physics-controlled mesh with a minimum element size of 200 nm and a maximum size of 1 μm is used. In the first step, the model is solved in stationary (time-independent) mode to calculate the electric field, which is assumed to stay constant during the avalanche process. The result can be seen in the multislice Figure 4.4. The model is then solved in the time-dependent mode for a single incident electron per run.

Release of incident particle

The position of the very first impact affects the final gain as an avalanche process starting too deep inside the channel leaves less channel length to produce secondary electrons. The maximum depth l_{max} before a wall intersection occurs depends on the angle θ_{In} between the channel and the incoming particle and the channel opening diameter d and is given by the simple trigonometric equation:

$$l_{max} = d / \tan(\theta_{In}) \quad (4.9)$$

To shorten the simulation time the primary electron is not released at the photocathode but at a random position of the channel opening as illustrated in Figure 4.5. Its kinetic energy at the release position is equal to the set potential difference between the the photocathode and the top electrode. The angle of the incoming electron has been set to 30° with respect to the normal of the AMCP top electrode as it was done in the Matlab based model.

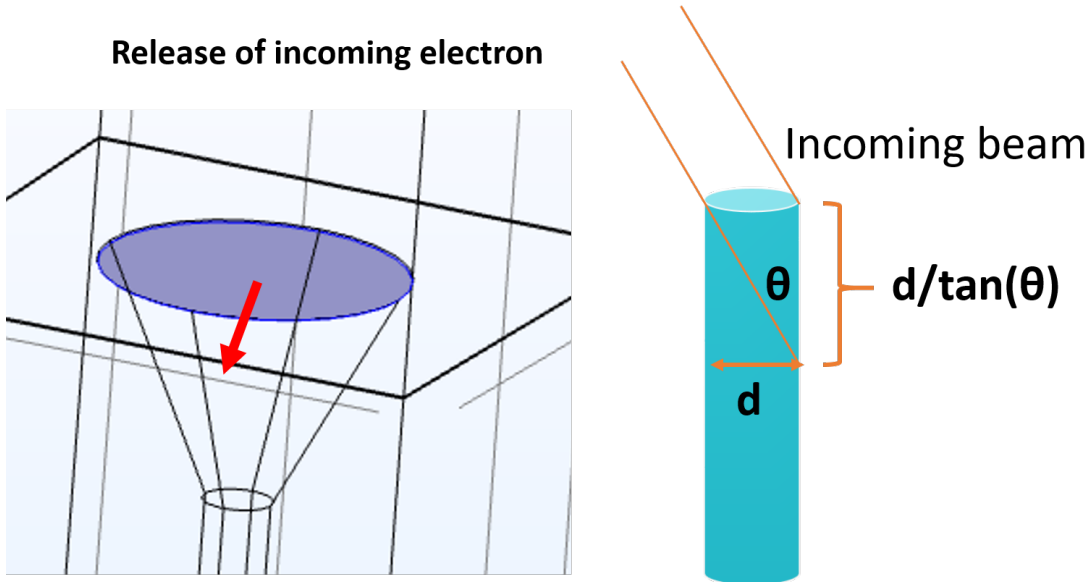


Figure 4.5: Each simulation starts with the release of a primary electron on a random position at the channel opening (purple area). The released electron has a kinetic energy of $V_{PC} - V_{Bias}$ and a release angle of 30° with respect to the AMCP surface normal.

Elastic backscattering

The channel walls have been defined to either bounce back (elastically backscatter) an incoming particle or otherwise release secondary electrons. The probability function for a particle to be elastically backscattered is the same as described in Equation 4.1 and was directly defined within COMSOL. In contrast to the original model there is no separate probability distribution for incoming angles above 85° as it was described in Section 2.1.2. The consequence is that at high incident angles θ_{In} the elastic backscatter probability might be underestimated. If the electron does not bounce back at the wall intersection it freezes and triggers the release of secondary electrons.

Secondary yield

The amount of secondary particles and their energies are then calculated in two separate MATLAB functions. The number of particles to be released is randomly picked out of a Poisson distribution centered around $\delta(E_{In}, \theta_{In})$ (Equation 4.3). Just as in the original model, $\delta(E_{In}, \theta_{In})$ also includes inelastically backscattered electrons. The total number of released electrons is then returned to COMSOL.

Emission energy and energy conservation

Once the total number of electrons to be released is determined, a second function is called to assign their kinetic energies. In a first step the function identifies which particles stem from the same event to ensure energy conservation. This can be easily done by inputting the energy of the initial primary electron into the function and by taking advantage of the fact that COMSOL processes all particles that had a collision event within the same time period at the same time. It is hence reasonable to assume that two particles stem from the same event when they were created at the same time and have the same primary electron energy. Afterwards the function determines the energies for each bunch of particles per event.

For every event, it is first determined whether one of the released particles is in fact an inelastic backscattered electron. This distinction is important because inelastic backscattered electrons have a much higher probability to have a bigger kinetic energy than secondary electrons. For this a random number is sampled between 0 and 1. If this number is smaller than $\eta_{IB} = 0.2$ one of the particles is considered to be inelastically backscattered and its energy is randomly chosen between 0 and $E_{In} - 2$ (see Section 4.1.2).

The energies of the non backscattered particles are then sampled from the distributions given in the Equations 4.5 and 4.6. After each event the condition

$$\sum_{p=1}^n E_p \leq E_{In} \quad (4.10)$$

needs to be fulfilled for the n number of released particles with emission energies E_p . If this is not the case the emission energies are reassigned until the energy is conserved. Then the next bunch is processed and eventually the emission energies are returned to COMSOL.

Secondary particles release

The secondary electrons are released with a direction given by θ_{SE} and φ_{SE} according to Equations 4.7 and 4.8 and the procedure is repeated at the next wall intersection. Finally, a particle counter records the number and timestamps of the electrons reaching the bottom of the channel. Each run starts with a single incident electron hitting the channel wall and between 500 and 1000 runs are conducted for each simulation. Afterward, the average gain and timing resolution can be calculated at the end of the simulation.

Parameter calibration

The two models were run for the same geometries and initial conditions and the results were compared. The COMSOL based model yielded gain values that were up to 20 % higher than the ones obtained from the original Monte-Carlo model. This discrepancy might be related to the slightly different implementation of the elastic backscatter. As a change in the backscatter probability at high incident angles is neglected the total amount of backscattered electrons might be underestimated which also affects the possible number of created secondary electrons. To compensate for this the maximum secondary yield at normal incidence $\delta(\theta_0)$ was refitted to accurately represent the available measurement data while all other parameters were kept constant. Its value was changed from $\delta(\theta_0) = 1.67$ to $\delta(\theta_0) = 1.58$. The choice to vary this parameter was made because it was originally fitted to the AMCP gain measurements and not calculated from independent yield or energy measurements.

4.1.3 Model limitations

The main drawback of the finite element method model is the increased computation time compared to the original Matlab-based model. Both models currently do not consider any effects due to wall charging or electron-electron interactions. Finally, since the experimental data to determine the parameters is limited, the model parameters will have to be continuously improved to fit future measurements better. Nevertheless, the current model represents an important tool to investigate the change of geometries on the detectors' gain and temporal behavior and help optimize the channel design.

4.2 Simulation results

The simulations obtained with the FEM model are presented in the next section. First, the model was used to predict the expected gain of the fabricated devices with an aspect ratio of 25 to later compare the predictions with the measurements. Afterward, funnel-shaped channels are simulated to investigate the effect of the change in geometry on the gain and timing properties. Finally, the simulation tool is used to explore the possibility of fabricating AMCPs with a trench geometry.

4.2.1 Simulation of a high aspect ratio device

First, the gain/voltage behavior was simulated for an AMCP with a channel length of $40\text{ }\mu\text{m}$ and diameter of $1.6\text{ }\mu\text{m}$, meaning an aspect ratio of 25, corresponding to the newest generation of fabricated devices. The simulation parameters are given in Table 4.2. The model was solved for 5 different applied bias voltages with 500 incident electrons per simulation. The results for a bias of -500 V are visualized in Figure 4.6.

Table 4.2: Simulation parameters for an AMCP with AR 25.

Simulation parameters	
Trench Length	$40\text{ }\mu\text{m}$
Trench Width	$1.6\text{ }\mu\text{m}$
Top Electrode Bias	-100 V to -500 V
Photocathode Bias	-300 V to -700 V
Beam Tilt	30°
Runs	500

An average gain of 1516 ± 149 was simulated when applying a maximum bias voltage of -500 V , corresponding to an applied electric field of $12.5 \cdot 10^4\text{ V/cm}$. The time resolution Δt has been defined as the FWHM of the arrival time distribution determined at a given threshold of the signal amplitude. For this analysis the time resolution was evaluated for a threshold set at 30, 50 and 80 % of the signal amplitude. The rise time was defined as the time it takes the current to increase from 10 % to 90 % of the maximum amplitude. A particle was counted as detected when a gain bigger than zero had been simulated. Like this, a detection efficiency of 82.6 % was found. It should be noted that this definition of detection efficiency assumes a 100 % active area of the device as the primary particle always enters the channel in the simulation. The same analysis was then done for simulations with applied biases of $-400/-300/-200$ and -100 V , and the results are summarized in Table 4.3.

Table 4.3: Simulation results for an AMCP with AR 25.

Value/Bias	500 V	400 V	300 V	200 V	100 V
Gain	1516±149	851±133	366±96	125±32	24±14
Δt (30 %)	(7.40±0.6) ps	(8.20±0.7) ps	(10.6±0.9) ps	(12.1±1.1) ps	(13.9±1.3) ps
Δt (50 %)	(6.70±0.6) ps	(7.80±0.7) ps	(9.70±0.9) ps	(10.5±1.1) ps	(12.7±1.3) ps
Δt (80 %)	(6.10±0.6) ps	(7.40±0.7) ps	(8.90±0.9) ps	(10.4±1.1) ps	(11.8±1.3) ps
Rise Time	(4.30±1.2) ps	(4.80±1.3) ps	(5.00±1.7) ps	(4.30±1.7) ps	(2.30±1.3) ps
Transit Time	(16.3±3.7) ps	(17.3±4.2) ps	(19.3±5.3) ps	(19.7±5.8) ps	(19.8±6.2) ps
Det. Eff.	82.6 %	81.2 %	78.4 %	73.0 %	66.2 %

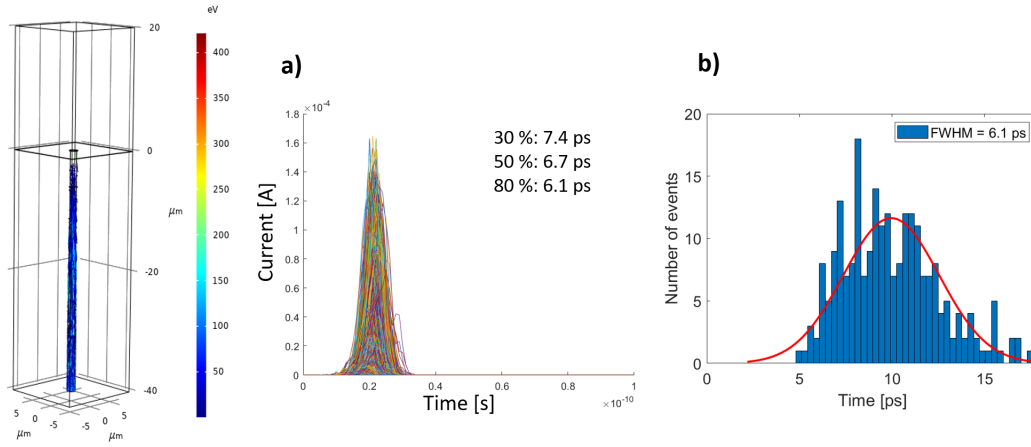


Figure 4.6: Simulation results for an AMCP with aspect ratio 25. The geometry and particle trajectories for one run can be seen in the left image. a.): Resulting current for each run and calculated time resolution. b.): Arrival time distribution at a threshold of 80 % of the signal amplitude.

The simulated gain as a function of the bias voltage is shown in Figure 4.7a. The model also predicts a log-linear relationship (Figure 4.7b) between the bias and the gain, which agrees with the one proposed by Eberhardt. The time resolution increases linearly with higher bias voltages (stronger electric fields). The detection efficiency slowly decreases with lower applied bias voltages as the probability of having a gain of zero increases.

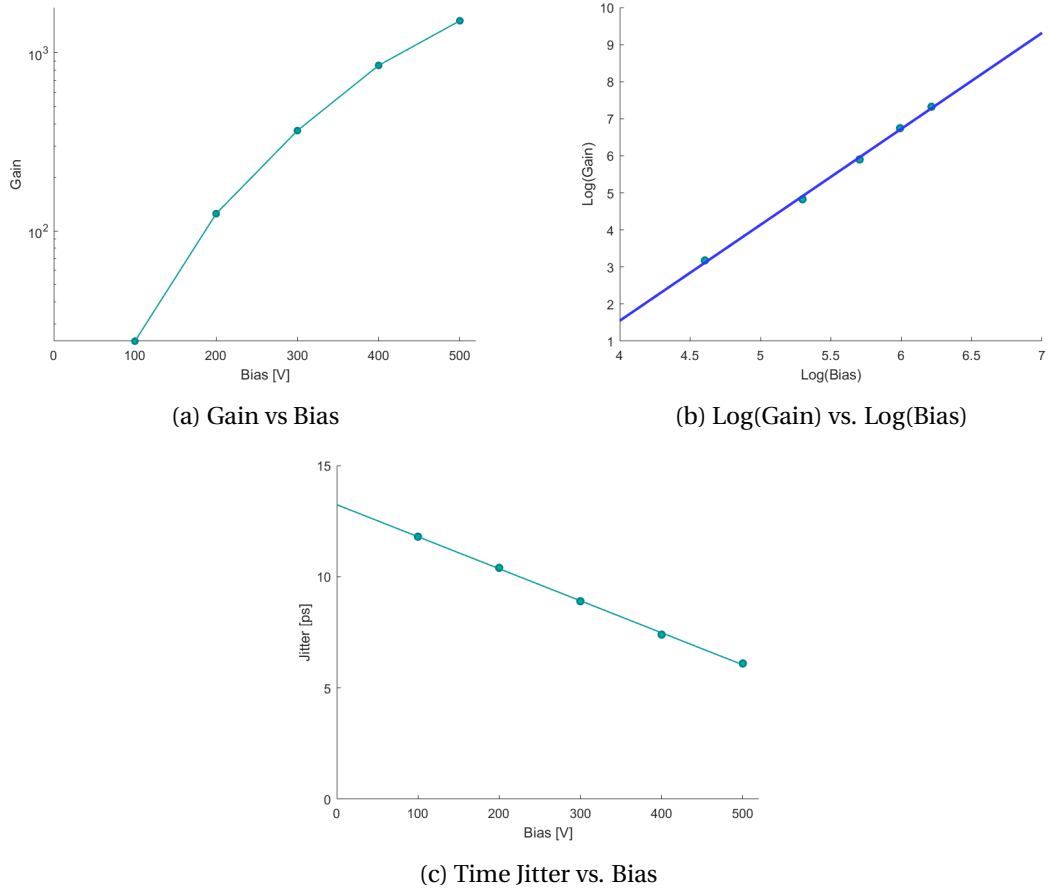


Figure 4.7: Relations between the applied bias voltage and the simulated gain and time resolution.

4.2.2 AMCPs with funnel-shaped channels

A realistic channel geometry with a funnel-shaped opening was simulated next. According to the current minimal pitch between the channels, the funnel opening was chosen to be $4\text{ }\mu\text{m}$. Etching the funnels in the cleanroom will slightly shorten the channel length and increase the lower channel diameter by 200-300 nm. So the lower channel diameter was set to $1.8\text{ }\mu\text{m}$, the total channel length to $39\text{ }\mu\text{m}$, and the funnel depth assumed to be $6\text{ }\mu\text{m}$. All other parameters were kept the same as in the simulation for the straight channel. The simulation settings are summarized in Table 4.4.

Table 4.4: Simulation parameters for an AMCP with a funnel-shaped opening

Simulation parameters	
Channel Length	$39\text{ }\mu\text{m}$
Funnel Diameter	$4\text{ }\mu\text{m}$
Funnel Depth	$6\text{ }\mu\text{m}$
Channel Diameter	$1.8\text{ }\mu\text{m}$
Top Electrode Bias	-500 V
Photocathode Bias	-700 V
Beam Tilt	30°
Runs	500

The results from the simulation are shown in Figure 4.8. As expected the average gain slightly decreased down to 1109 ± 112 with respect to the circular channel device simulated in 4.2.1.

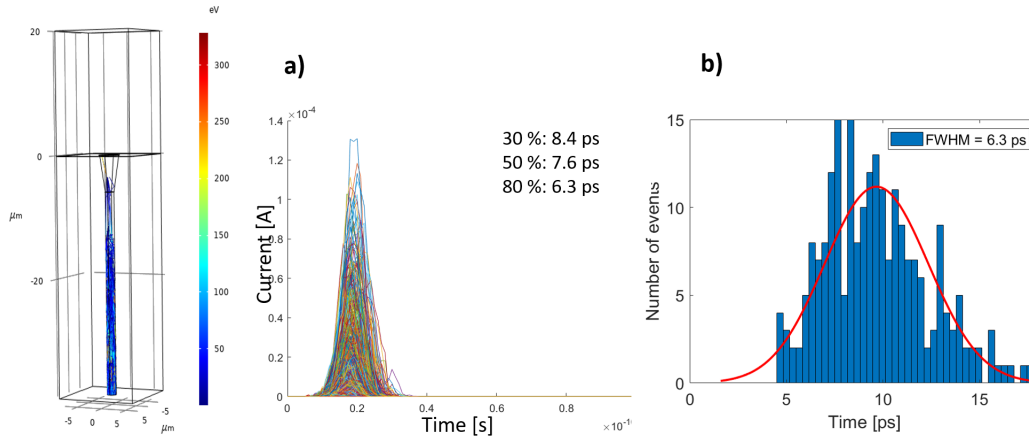


Figure 4.8: Simulation of a funnel AMCP without any additional coatings. Left: Geometry and example of a particle trajectory. a.): Resulting current for each run and calculated time resolution. b.): Arrival time distribution at a threshold of 80 % of the signal amplitude.

However, this decrease is only due to the slight broadening of the lower channel and the decrease in channel length, unavoidable during an actual fabrication process. The funnel opening itself is not expected to cause a significant loss in gain as long as it is confined to the upper few μm of the channel. The time resolution is with 6.3 ps, almost unchanged compared to the straight channel simulation ($\Delta t = 6.1$ ps). The wide opening on top allows for sputtering materials with a high secondary emission coefficient inside the funnels, such as magnesium oxide (MgO). The same simulation was run assuming a MgO coating over the entire funnel area- indicated in purple in Figure 4.9.

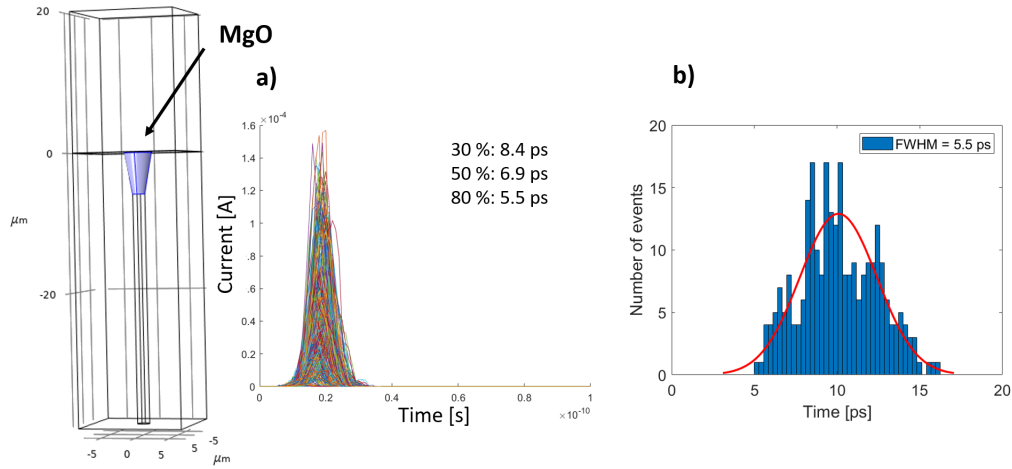


Figure 4.9: Simulation of a funnel AMCP with an MgO coating on top. Left: Geometry of the channel, the MgO coated area is indicated in purple. a.): Resulting current for each run and calculated time resolution. b.): Arrival time distribution at a threshold of 80 % of the signal amplitude.

As seen from the simulation results in Figure 4.9, having a MgO coating on top massively enhances the average gain up to 1912 ± 130 for the same geometry. This increase is due to a higher secondary emission at the first impact. Although the simulation parameters for MgO are only estimated due to a lack of measurement data, this simulation shows the huge potential of applying coatings to the funnel walls. It is also important to note that this configuration has the overall highest detection efficiency. Since the Poisson distribution at the first impact is centered at a much higher value than for a-Si:H, it is much less likely not to have any secondary electrons produced at this impact. Which, of course, increases the overall detection efficiency. Having a MgO layer on top could be crucial for detecting single electrons. The results for both simulations are summarized in Table 4.5.

Table 4.5: Simulation results for a funnel AMCP with and without MgO

	Regular a-Si:H	MgO coating (top)
Average Gain	1109±112	1912±130
Δt (30 %)	(8.40±0.7) ps	(8.40±0.6) ps
Δt (50 %)	(7.60±0.7) ps	(6.90±0.6) ps
Δt (80 %)	(6.30±0.7) ps	(5.50±0.6) ps
Rise Time	(4.39±1.4) ps	(4.70±1.1) ps
Transit Time	(16.5±4.4) ps	(18.0±3.2) ps
Det. Eff.	93.0 %	99.6 %

4.2.3 AMCP with a trench geometry

Finally, a simulation was run to explore the option of having AMCPs with a trench geometry, as shown in Figure 4.10, rather than holes. This will cause a loss in gain due to the larger diameter in one direction and slightly decrease the spatial resolution- depending on the width of the trench. The advantage is that much deeper structures can be etched due to the easier gas access during fabrication which will be discussed more in the next chapter. First, a shallow trench was simulated with a total depth of 40 μm and a width of 1.6 μm - corresponding to the values of the circular AMCP for comparison. The length was chosen to be 5 μm . Afterward, the simulation was run for a deeper channel with 80 μm channel depth. It was assumed that the same 12.5 V/ μm could be applied to the top electrode. The simulation settings are given in Table 4.6.

Table 4.6: Simulation parameters for an AMCP with trenches.

	Shallow Trench	Deep Trench
Trench Depth	40 μm	80 μm
Trench Width	1.6 μm	1.6 μm
Trench Length	5 μm	5 μm
Top Electrode Bias	-500 V	-1000 V
Photocathode Bias	-700 V	-1200 V
Beam Tilt	30 °	30 °
Runs	500	500

The results are shown in Figure 4.10. The gain decreased to 774 ± 89 , approximately half the gain of the circular AMCP with the same channel length. This result is not surprising due to the wider opening in one direction. The spread in arrival time appears to be not significantly affected by the change in geometry.

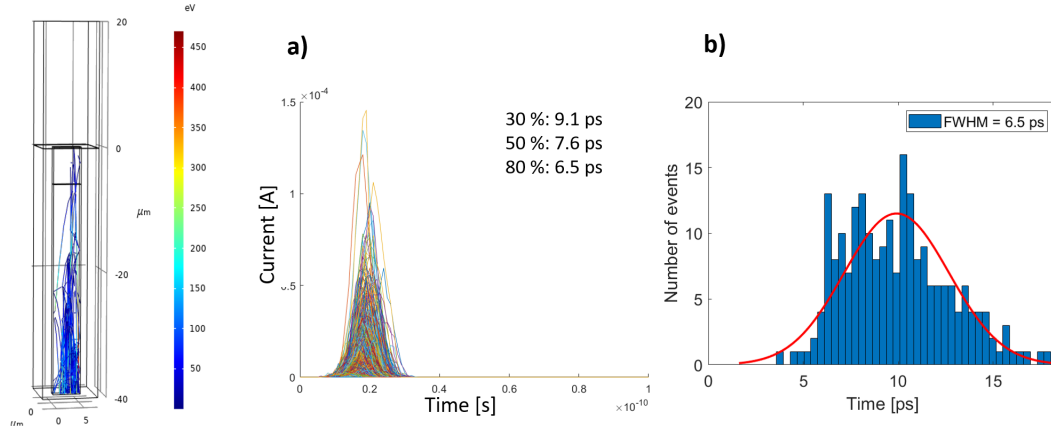


Figure 4.10: Simulation of an AMCP with a shallow trench geometry (left). a.): Resulting current for each run and calculated time resolution. b.): Arrival time distribution at a threshold of 80 % of the signal amplitude.

Next, a simulation was run for a deep trench. The results are shown in Figure 4.11. A maximum gain of 3457 ± 188 could be simulated with this geometry, with the other values not significantly affected by the geometry change. The values for both trenches are summarized in Table 4.7. The exact length of the trenches would need to be optimized with respect to cleanroom procedures and the importance of the spatial resolution in the final detector. Nevertheless, this geometry should be further explored for applications where higher multiplication gains are needed.

Table 4.7: Simulation results for an AMCP with trenches.

	Shallow Trench	Deep Trench
Average Gain	774 ± 89	3457 ± 188
Δt (30 %)	(9.10 ± 0.7) ps	(6.00 ± 0.4) ps
Δt (50 %)	(7.60 ± 0.7) ps	(5.30 ± 0.4) ps
Δt (80 %)	(6.50 ± 0.7) ps	(4.80 ± 0.4) ps
Rise Time	(4.30 ± 1.4) ps	(4.50 ± 0.9) ps
Transit Time	(16.1 ± 4.4) ps	(16.8 ± 3.8) ps
Det. Eff.	89.6 %	91.6 %

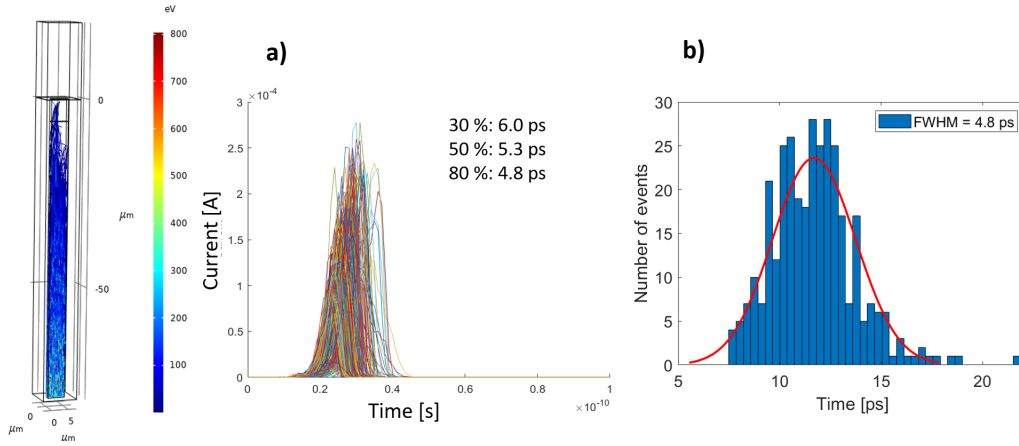


Figure 4.11: Simulation of an AMCP with a deep trench geometry (left). a.): Resulting current for each run and calculated time resolution. b.): Arrival time distribution at a threshold of 80 % of the signal amplitude.

4.3 Conclusion and summary

In this chapter the implementation of a cinematic Monte-Carlo model into a COMSOL-based FEM model was presented. The COMSOL model represents a powerful tool to investigate the influence of the change in channel geometry on essential values such as the channel gain, the time resolution, and the detection efficiency. In the second part of the chapter, the simulation tool was used to predict the behavior of realistic channel geometries fabricated in the cleanroom. The time resolution for all investigated geometries was simulated to be a few ps. Although the actual timing properties of the real device will be affected by the incident angle of the incoming particle and the electronics underneath, it was important to simulate whether it would be influenced significantly by the larger funnel-shaped opening. For single particle detection, a funnel geometry with a MgO coating was found to be best suited to achieve the highest detection efficiency- even without considering the detector's active area. MgO coatings could also be applied to straight channels by ALD coatings, but having too thick ALD layers at the bottom of the channel could affect charge collection and replenishment. Having a funnel opening makes applying MgO easier as the wide opening allows for sputtering. Trench-shaped AMCPs are a valuable option when high multiplication gains are needed. In Chapter 6, the simulation results will be compared with the performance of actual devices to better understand the model's accuracy. The model parameters are expected to require adjustments when more experimental data is available. Further improvements could also consider saturation effects and a more realistic field distribution within the amorphous silicon layer if needed.

5 Fabrication of AMCPs

5.1 AMCP- fifth generation fabrication

This section first summarizes the prior AMCP generations, discussing their main characteristics and improvements with respect to the previous devices. Afterward, the fabrication process of the 5th AMCP generation with aspect ratios up to 25 and small channel diameter down to 1.6 μm is described in detail.

5.1.1 Motivation and prior art

Four previous generations of AMCPs had been fabricated and were available at the beginning of this thesis. Since their structure and working principle were already described in Chapter 2.3, only a summary of their main characteristics is given here. The first prototype detectors were fabricated in 2010 and showed a response to an incoming electron beam, although no exact gain could be determined [37], [38]. This first generation suffered from various fabrication defects. The uneven thickness of the a-Si:H layer across the wafer made it challenging to ensure all channels reached the bottom anode. Columnar defects additionally reduced the AMCP sensing area and led to enhanced leakage currents. Finally, the DRIE process was not yet optimized for the channel geometry and caused very uneven channel shapes and occasionally resulted in the collapse of the entire AMCP sensor area. These issues were eventually addressed in the second generation of AMCPs. The uniformity of the amorphous silicon layer was improved to around 90- 95 % over the wafer surface. The formation of structural defects was also reduced, so higher bias voltages could be applied to the layer. Still, no gain could be calibrated due to the leakage current on the anode being larger than the resulting signal from the multiplication. A measurable multiplication signal was first observed with the introduction of the intermediate electrode in the 3rd generation causing the residual leakage current on the anode to drop by about five orders of magnitude.

A maximum gain of 45 was measured for channels with an aspect ratio of 12.5, which could be improved to 80 by coating the channel walls with alumina [39]. This gain is still too low to use AMCPs effectively in real applications. It must be increased to at least several hundred to trigger a minimal detectable signal with modern electronics. Simulations have shown that a gain of ~2000 can be achieved by increasing the aspect ratio to 30 [76]. Increasing the aspect ratio is not a trivial task. The best option to achieve this is by decreasing the channel diameter from 6- 8 μm down to 1- 2 μm , as smaller channels are favorable in terms of timing resolution. Fabricating such small channels comes with various difficulties related to the cleanroom processes. The first step in this direction was done in the 4th generation with the introduction of a metal hard mask. Samples with aspect ratios up to 22 and channel diameters down to 3 μm could be fabricated. These samples, however, exhibited a too high leakage current, indicating either an insufficient evacuation of the current flowing through the stack at the intermediate electrode or fabrication defects inside the layer. In the newest generation of AMCP, the channel diameter was reduced to 1.6 μm to increase the aspect ratio to 25. Additionally, the $\mu\text{c-Si}$ based intermediate electrode was replaced by a metal one. Table 5.1 summarizes the specifications for each generation of AMCPs.

Table 5.1: Specifications of the different AMCP generations

Property	Gen. 1	Gen. 2	Gen. 3	Gen. 4	Gen. 5
Layer Thickness	80- 100 μm	80- 100 μm	60- 100 μm	50- 60 μm	40- 50 μm
Min. Diameter	~4 μm	~4 μm	~6 μm	~3 μm	~1.6 μm
Max. Aspect Ratio	~10- 20	~10- 20	~14	~22	~25
Max. Bias	350 V	500 V	500 V	300 V	500 V
Leakage	~mA	~ μA	~pA	~ μA	~pA
Max. Gain	-	-	~100	-	~1500
Electrode (Top)	$\langle n \rangle \mu\text{c-Si}$	$\langle n \rangle \mu\text{c-Si}$	$\langle n \rangle \mu\text{c-Si}$	Cr	Al
Electrode (Mid.)	-	-	$\langle n \rangle \mu\text{c-Si}$	$\langle n \rangle \mu\text{c-Si}$	Cr
Electrode (Bot.)	Al	Al	Cr	Cr	Cr/Al/Cr
Notes:	Columnar defects	a-Si:H uniformity improved	Middle electrode added	Chromium electrode on top	Chromium middle electrode

5.1.2 Process flow

The AMCPs were fabricated on 1 mm thick, double-side polished 4-inch silicon wafers with a 1 μm wet oxide on top. The following pages illustrate the different steps in the entire process flow, displaying critical issues that had to be resolved.

Bottom electrode

A chromium (10 nm)/aluminum (100 nm)/chromium (10 nm) sandwich structure was sputtered on the wafer to fabricate the bottom electrode. The bottom chromium layer ensures good adhesion to the substrate, while aluminum increases the conductivity of the anode. Additionally, using aluminum allows later directly connecting the wire bonds on the pads without the need to glue gold plates on the pads. Aluminum is well known to diffuse into a-Si:H already at temperatures around 200 $^{\circ}\text{C}$ [82]. This induces the formation of hillocks in the a-Si:H layer above. The final thin chromium layer served as a barrier for the aluminum to prevent this effect. The metal was then patterned by a photolithography step, using standard spin-coating and mask exposure tools. To increase the photoresist adhesion to the metallic surface, dehydration (5 minutes at 150 $^{\circ}\text{C}$) was performed before the spin-coating. The used photoresist AZ® ECI 3007 is a positive resist for high-resolution photolithography. More detailed parameters for the photolithography are mentioned in Figure 5.1. The bottom electrode structure has been redesigned in preparation for the characterization of the temporal properties of the detectors. The main changes include smaller sensor areas (1000/500 and 250 μm) with shorter and broader connection lines. Additionally, the pads are surrounded by a metal guard ring to better shield the incoming signal. Finally, the metal was etched by wet etching, and the residual resist was removed. The structure of the bottom electrode is shown in Figure 5.2.

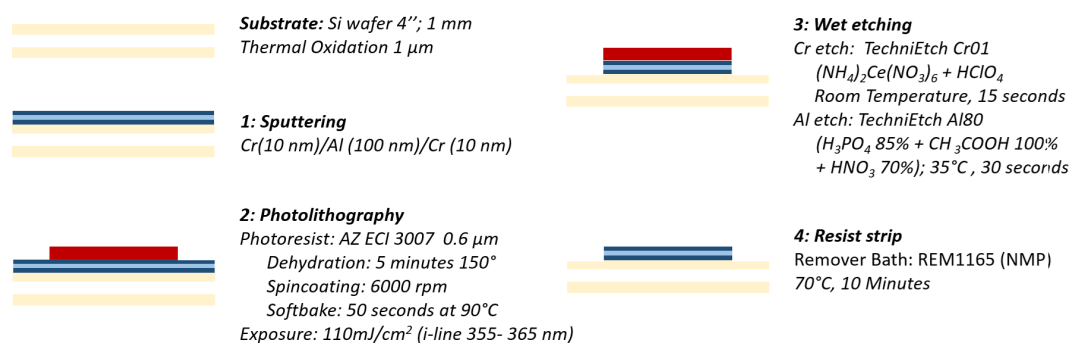


Figure 5.1: Fabrication of the bottom metal layer. The metal layers are sputtered on the substrate, patterned by photolithography, and finally etched by wet etching.

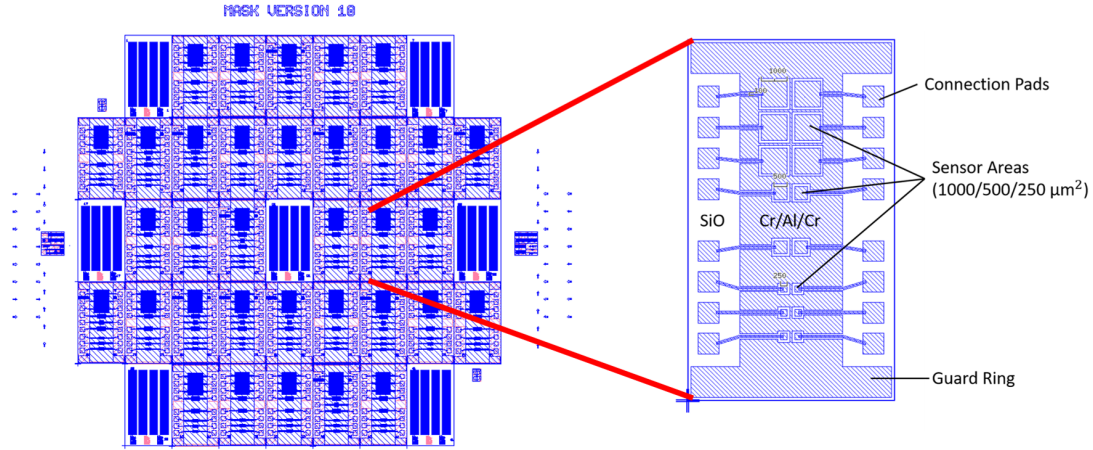


Figure 5.2: Design of the bottom metal layer. The metal consists of chromium and aluminum with a total thickness of 120 nm. Each test structure has 16 active areas of three sizes (1000/500 and 250 μm). A grounded metal area surrounds the test structures, serving as a guard ring.

Decoupling layer

A 2 μm thick a-Si:H layer was deposited by PE-CVD on the bottom electrode. This decoupling layer is used to electrically isolate the anodes from the intermediate electrode (with a resistivity of about $\rho \sim 10^{11} \Omega \text{ cm}$). A trade-off had to be found for the thickness of this layer. A thicker decoupling layer increases the anode's electric isolation and decreases the capacitance between the two electrodes. A low capacitance will be essential to achieving the optimal timing resolution of the final detector. However, a thick decoupling layer also decreases the effective aspect ratio of the channels. Since no electric field is present between the anode and the intermediate electrode, this layer does not contribute to the electron multiplication. Additionally, charging effects may become more pronounced with a thicker decoupling layer. Besides the electrical isolation, this a-Si:H was also used to compensate for some of the stress-induced wafer bending caused by the deposition of the main a-Si:H layer later on. Intrinsic stress in amorphous silicon is a function of the deposition parameters such as the plasma excitation frequency, temperature, and process pressure. It has been shown that an excitation frequency of 70 MHz and process temperature around 200 °C results in a low-stress material with a low defect density [21]. The net intrinsic stress in a-Si:H is a balance between the compressive and tensile stress components. At lower deposition pressures, the ion energies increase due to a longer mean free path, causing an increase in compressive stress [83]. The decoupling layer was grown at a compressive stress of around -138 MPa causing a wafer bow around 9 μm . The deposition conditions and a typical bow curve of a wafer at this stage in the process are shown in Figure 5.3.

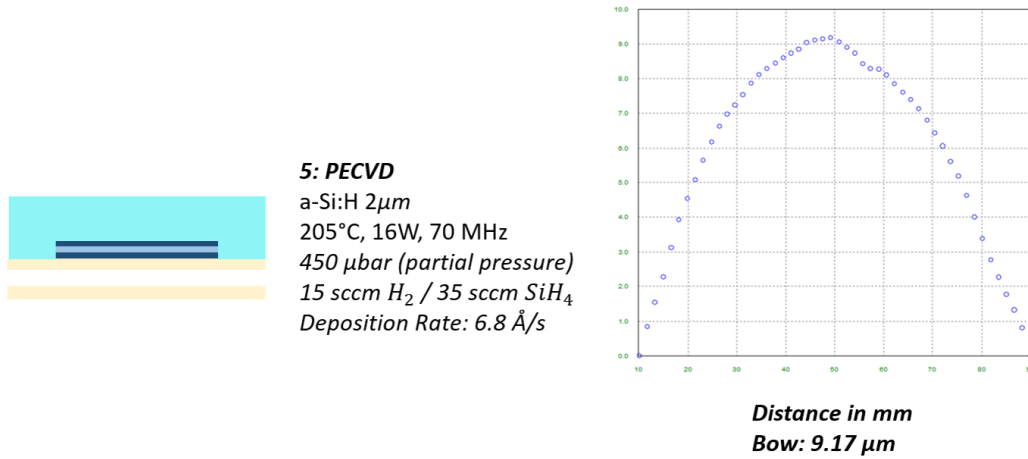


Figure 5.3: Deposition parameters of the 2 μm thick a-Si:H decoupling layer and the resulting bow due to the intrinsic compressive stress.

Intermediate electrode

A chromium-based intermediate electrode replaced the n-doped $\mu\text{c-Si}$ one of the previous generations. Earlier measurements have shown a voltage rise of the intermediate electrode with respect to ground and the anode across the intermediate electrode [19]. This was believed to be due to a too high sheet resistance ($\sim 1 \text{ k}\Omega$) of the $\mu\text{c-Si}$, leading to a non-equipotentiality of the electrode. Such a voltage rise eventually caused an increase in the leakage current and lead to an unstable output signal. To fabricate the intermediate electrode, a 80 nm thick chromium layer was sputtered onto the decoupling layer and patterned by a photolithography step. Aligning the chromium pattern with the metal pads underneath was done with alignment markers placed on the first metal layer. The openings in the metal where the channels will be later etched through were purposefully made slightly bigger (2 μm in diameter) than the targeted channel diameter ($\sim 1.5 \mu\text{m}$) to compensate for unavoidable alignment errors of a few 100 nanometers between the middle and top electrode. The pitches between the channels vary within the different chips on one wafer between 3 to 10 μm (center to center). The design of one test structure and the used alignment markers are shown in Figure 5.4. Finally, the chromium was etched, and the photoresist was removed. After stripping the photoresist, residues tend to stick to etches of the chromium. Because even slight photoresist remains can cause hydrogen accumulations when growing the thick amorphous silicon layer on top of it, an additional cleaning step in a piranha solution was introduced. In a final step, a thin layer (100 nm) of n-doped $\mu\text{c-Si}$ was grown on the chromium to ensure the presence of a conductive layer all the way to the channel. All the details for the fabrication process are summarized in Figure 5.5.

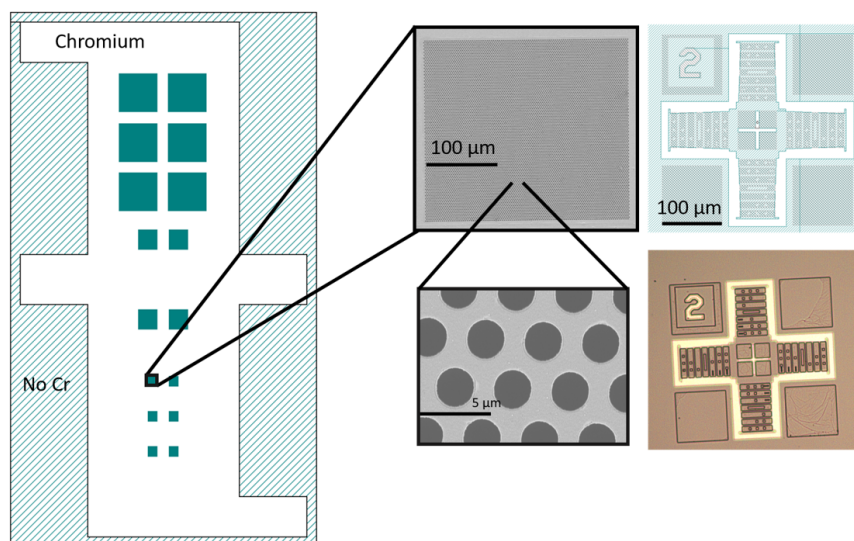


Figure 5.4: Design of the intermediate electrode. Chromium (white) covers most of the chip and is only removed (green area) where the channels will pass through and on the edges of each chip to allow access to the bonding pads underneath. The design of the hole array and alignment markers are also shown..

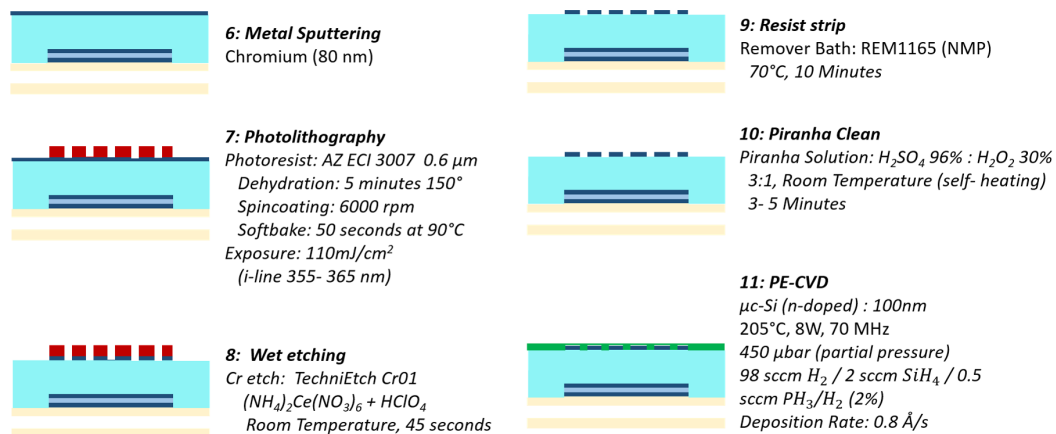


Figure 5.5: Fabrication steps for the intermediate electrode. Chromium is sputtered on the decoupling layer and patterned by photolithography. The metal is etched and the photoresist removed. Finally a thin n-doped µc-Si layer is grown on top of the chromium.

Multiplication layer

The primary fabrication step consists of depositing a 40 to 100 μm thick a-Si:H layer. Depositing thick amorphous silicon layers is challenging. Intrinsic stress of the material needs to be kept low throughout the deposition to avoid blistering and/or delamination of the film and prevent problems in the following fabrication steps. Hydrogen diffusion during the layer growth can cause molecular hydrogen accumulation, eventually forming bubbles in the film. Lastly, the deposition rate must be reasonably high to prevent too long deposition times. Intrinsic stress, deposition rate, and layer quality are complicated functions of the deposition parameters and need to be adjusted for the application in AMCPs. The deposition recipe has been further optimized from the one utilized in previous AMCP generations to achieve a blister-free surface and decreased intrinsic stress. The problem of blister formation in a-Si:H can be explained by a diffusion model initially proposed by Shanks and Ley [84]. Further details were later provided by Mishima and Yagishita [85]. The blisters are caused by hydrogen diffusing from the Si-H dangling bonds and accumulating at the lattice defects of the film-substrate interface. The forming blisters consist of molecular hydrogen with the size of the bubbles depending on the substrate temperature. We observed that preventing the formation of blisters is most critical during the first few μm of the deposition. A first study was done to test two different adhesion layers - a 90 nm thick silicon oxide layer used in previous AMCPs and a 40 nm thick a-Si:H layer with a high hydrogen dilution. A 5 μm thick a-Si:H layer was then grown on the adhesion layer at 205 $^{\circ}\text{C}$ and a deposition pressure of 650 μbar . Three different flux ratios between the precursor gases silane and hydrogen were also tested. The number of blisters was then counted on a 25 mm^2 area to decide on the best recipe and adhesion layer. The substrate for all the test pieces was a standard c-Si wafer. Figure 5.6 shows the microscope images from the test.

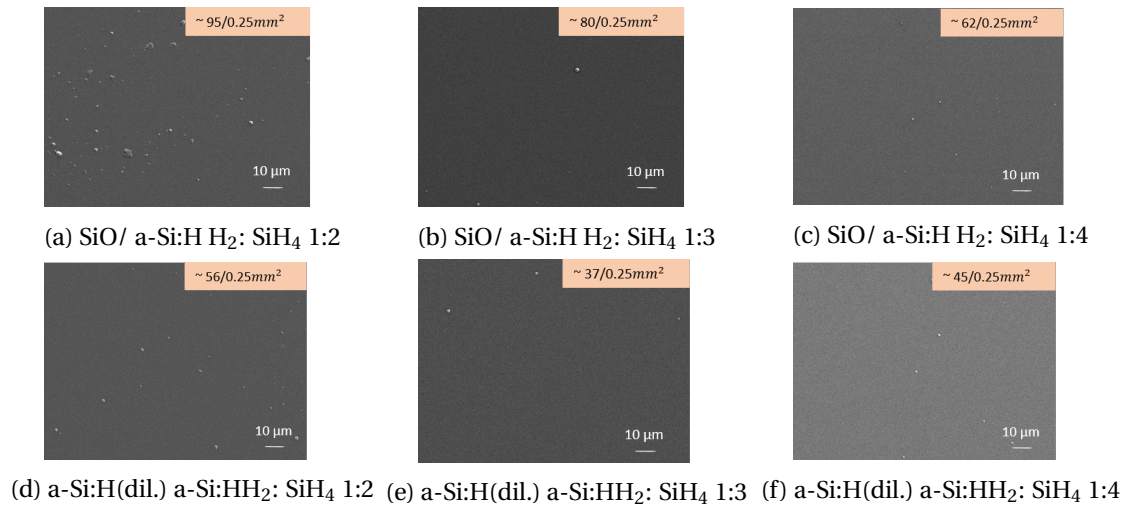


Figure 5.6: Blister formation of two different adhesion layers and with three different flux ratios of the precursor gases.

The number of blisters was lowered by roughly two when using a diluted amorphous silicon adhesion layer instead of the oxide layer. The difference between the different flux ratios was less apparent. The bubbles seem less frequent and smaller in size when changing from a hydrogen to silane ratio of 1:2 to 1:3, and increasing the ratio to 1:4 does not appear to produce any more significant changes. Both layers offered an excellent adhesion of the amorphous film to the substrate. Based on these results, the adhesion layer was changed to a-Si:H (diluted), and the hydrogen to silane ratio was set to 1:3. Because diffusion is a temperature-dependent process, keeping the deposition temperature low during the first few μm of growth also helps to reduce the number of blisters.

During the growth of the layer, the stress also needs to be kept as low as possible to minimize the risk of delamination. The residual stress also causes bending of the wafer, which might introduce problems in the following photolithography and etching steps. The final bow of the wafer should, therefore not exceed 100 μm at most. The total stress is composed of thermally induced stress and intrinsic stress. Thermally induced stress is due to a difference in the thermal expansion coefficients between the layers. When a film is deposited at a temperature T_s the resulting thermally induced stress σ_{th} can be calculated according to [86]:

$$\sigma_{th} = \frac{Y_F}{1 - \nu_F} (\alpha_f - \alpha_s) (T_s - T_a), \quad (5.1)$$

where Y_F and ν_F are Young's modulus and Poisson's ratio of the growing film, α_f , and α_s are the average coefficients of thermal expansion for the film and substrate, and T_a is the temperature during the measurement. For a-Si:H with $Y_F \sim 150$ GPa and $\nu_F \sim 0.2$, this yields thermally induced stress around +14 MPa.

The intrinsic stress of a-Si:H films results from a balance between compressive and tensile stress forces, which depend on the deposition parameters. The compressive component stems from lattice expansion effects and increases with higher ion energies (lower pressure or higher deposition temperature). In contrast, the tensile component is due to the collapse of hydrogenated nanovoids [87], [88]. The total stress σ_{tot} in a layer can be approximated by measuring the wafer bending due to the deposited layer according to Stoney [89]:

$$\sigma_{tot} = \frac{E_s t_s^2}{6 t_f (1 - \nu_s)} \frac{1}{R_f - R_0}, \quad (5.2)$$

where E_s is the elastic modulus of the substrate t_s and t_f the thicknesses of the substrate and film, and $R_f - R_0$ the change in the radius of curvature. The intrinsic stress σ_i is then given by:

$$\sigma_i = \sigma_{tot} - \sigma_{th}. \quad (5.3)$$

The intrinsic stress was measured as a function of the deposition pressure while keeping all other parameters constant. The results are summarized in Figure 5.7. The a-Si:H layers were 2 μm thick and deposited on a standard silicon wafer. Very low-stress layers (~ 5 MPa) could be deposited at a process pressure of 600 μbar . However, the same recipe yielded a much higher compressive stress (~ 30 MPa) when a 10 μm thick layer was grown. The same shift towards higher compressive stress with longer deposition times could be shown for different recipes.

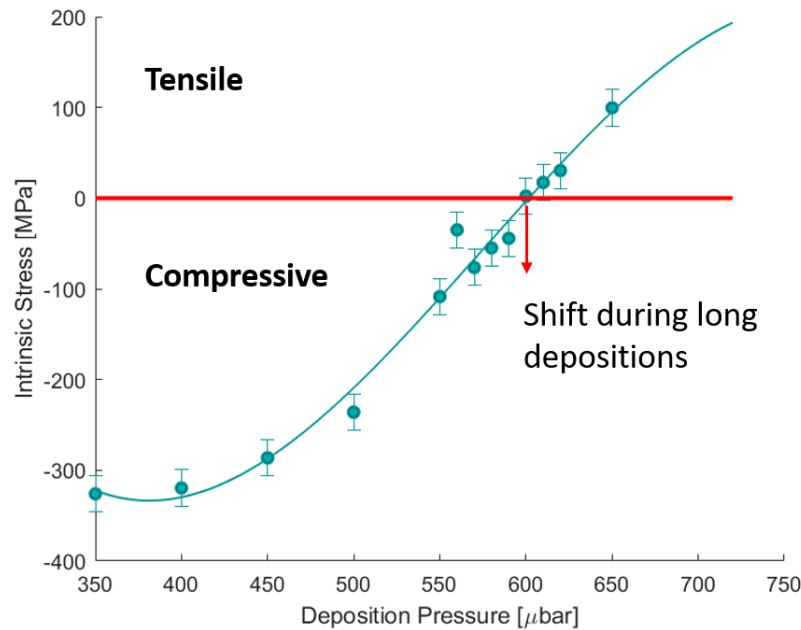


Figure 5.7: Intrinsic stress of a-Si:H as a function of the deposition pressure for 2 μm thick layers.

This increase of compressive stress appears to be only related to the deposition time but not to the thickness of the layer. As mentioned, a 10 μm thick layer grown at 600 μbar yielded a compressive stress of ~ 30 MPa. If the same layer was grown in steps of 2 μm thick layers, where the deposition was stopped periodically, the initial 5 MPa tensile stress could also be recovered for the thicker layer. The most probable reason for this effect is increase of the substrate temperature as well as heating of the entire deposition system, which also affects plasma conditions in the chamber. A higher deposition temperature causes an increase in the compressive stress component. A linear relationship was found between temperature and compressive stress for deposition conditions where the net stress was already compressive. The increase in the compressive component with higher temperature could also be observed for the net tensile stress regime but was less pronounced, as shown in Figure 5.8. Similar effects have been reported for other layers grown by plasma deposition, especially with high deposition rates [90].

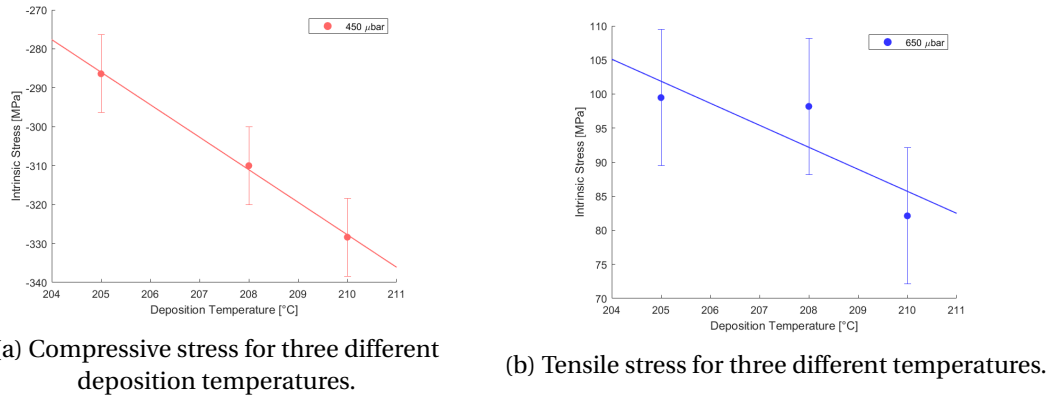


Figure 5.8: Intrinsic stress of a-Si:H as a function of temperature for two different pressure values. In the compressive regime, the stress increases linearly with the increase in temperature. In the tensile regime, the increase is considerably slower.

Finally, the thick layer was deposited at a pressure of 650 μbar . At this pressure, the layer started with a relatively high tensile stress but then decreased over time and stabilized at a much lower value. To further decrease the net stress, the temperature was increased from 205 °C to 208 °C after fifty minutes and finally to 210 °C after ninety minutes when the first few μm of layers have been deposited. Increasing the temperature at the start of the deposition would again cause hydrogen blisters. With this recipe, layers with an average stress of 20 MPa could be deposited. To further decrease the bending of the wafer due to stress, the substrate was changed to a 1 mm thick silicon wafer since the bending is proportional to the inverse square of the substrate thickness according to Equation 5.2. After the deposition of the main a-Si:H layer, a chemical/mechanical polishing step has been introduced to provide a smooth surface for the final photolithography. The unevenness (lowest to highest point) of the surface was around 200 nm due to the buried steps underneath. Figure 5.9 gives the process flow details.

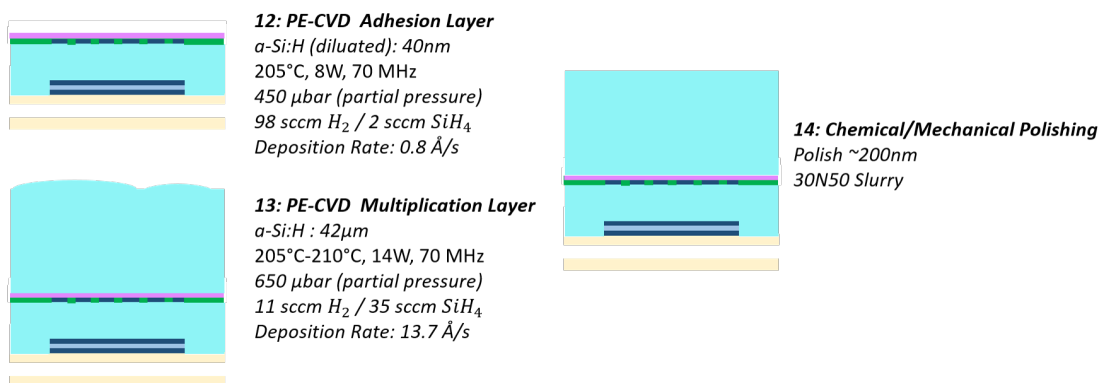


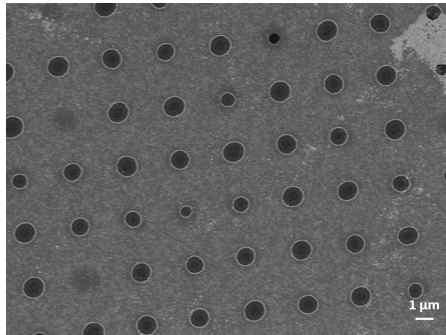
Figure 5.9: Process flow steps for the main a-Si:H multiplication layer. The layer is deposited by PE-CVD to a final thickness between 40- 50 μm . The wafer is then polished in preparation for the last photolithography step.

Top electrode

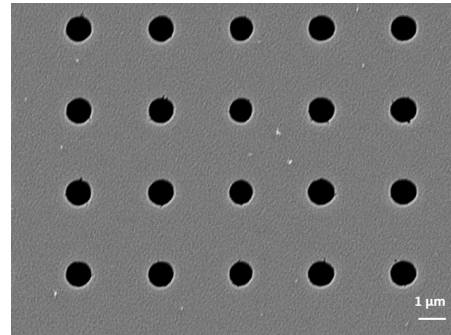
An 80 nm thick aluminum layer was sputtered on the wafer to fabricate the top electrode. No hillock formation was observed at the Al/a-Si:H interface since process temperatures stay way below 200 °C for the final steps. In order to achieve high aspect ratios, the channel diameters for the final lithography were designed to be 1 μm . Such a high resolution is close to the limit of standard UV lithography. The diffraction of the light limits the lateral resolution d of the transferred image according to:

$$d = (\lambda g)^{\frac{1}{2}}, \quad (5.4)$$

with the wavelength of the light λ and the gap between the mask and the resist surface g . The resolution is limited even without a gap ($g = 0$) due to the non-zero resist thickness. From this, it is clear that even a tiny gap of a few μm is enough to lose the required resolution. Because of the many layers deposited during the whole fabrication process, the wafer usually exhibits a bow of around 5- 10 μm at this point. For this reason, the final photoresist exposure was performed by direct laser writing rather than a mask exposure. Thus, the laser's focus was automatically adjusted over the wafer surface. Another issue was caused by the high reflectivity of the aluminum layer. During exposure, the incident light interferes with the light reflected from the surface. In the case of highly reflective substrates, these two intensities become comparable, causing an inhomogeneous light exposure that is especially problematic for small feature sizes. To minimize the substrate reflectivity, an bottom anti-reflective coating (BARC) was spin-coated before the photoresist. A comparison between exposure with and without BARC is shown in Figure 5.10. Without the additional BARC coating, the exposed holes varied in size and showed uneven edges.



(a) 1 μm holes achieved without BARC coating



(b) 1 μm holes achieved with BARC coating

Figure 5.10: Comparison between small holes achieved with and without an antireflective coating.

Since the alignment of the holes with the ones underneath is quite critical (± 500 nm precision), additional alignment markers were added to the middle electrode. The vernier markers at the edges allowed to estimate the alignment error so that the lithography could be redone if the error was bigger than the margin.

The design of the top electrode, as well as the alignment markers, are shown in Figure 5.11. After the lithography, both the BARC and the metal were dry-etched. All the detailed process steps are shown in Figure 5.12.

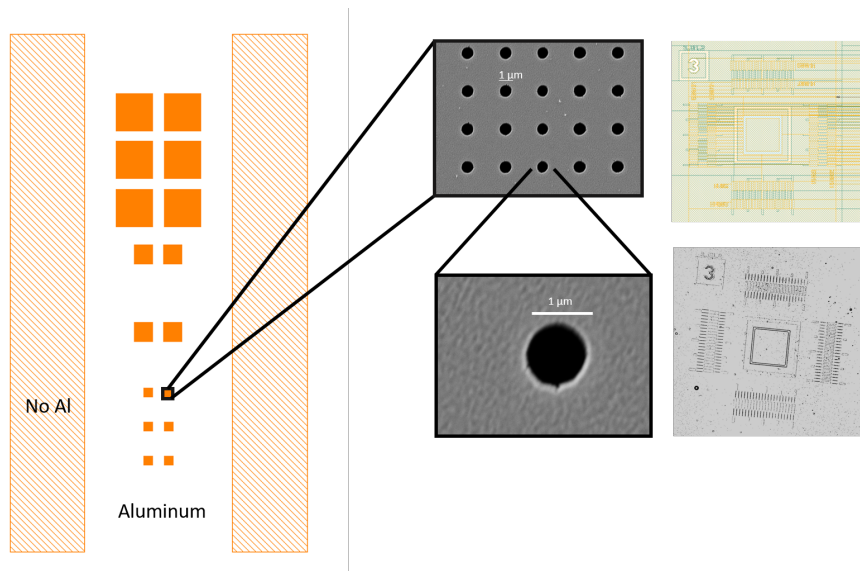


Figure 5.11: Design of the top electrode made out of aluminum (white). The metal is removed at the edges (orange area) to access the bonding pads underneath.

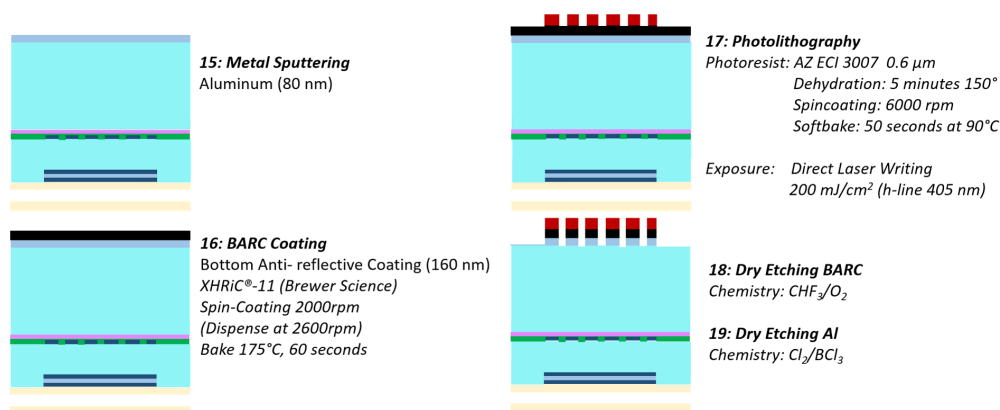


Figure 5.12: Process steps for fabricating the top electrode. Aluminum is sputtered on top, and an antireflective coating is added before the photoresist. The exposure is performed using direct laser writing. Finally, the coating layer and metal are dry-etched.

Microchannels

Another critical step in the AMCP fabrication process is the deep reactive ion etching of the microchannels. In all dry etching processes, etching is done by molecules in the gas phase. A wafer is placed in a dry etching reactor, and a plasma can be created by a high voltage radio frequency field. A typical gas used for silicon etching is sulfur hexafluoride (SF_6). The created fluoride radicals in the plasma state are very reactive and quickly etch the silicon. To achieve an etching process with a high anisotropy (etching in the vertical direction with little or no horizontal etching) and hence high channel aspect ratios, a so-called Bosch Process is used [91]. In this process, two etching gases SF_6 and octafluorocyclobutane (C_4F_8) are used in a consecutive pulsed manner during the etching. The SF_6 gas etches the silicon while the more carbon-rich C_4F_8 causes CF_3 radicals to be adsorbed on the silicon surface, leading to the generation of fluorocarbon-type polymer chains. Figure 5.13a schematically shows the process sequences.

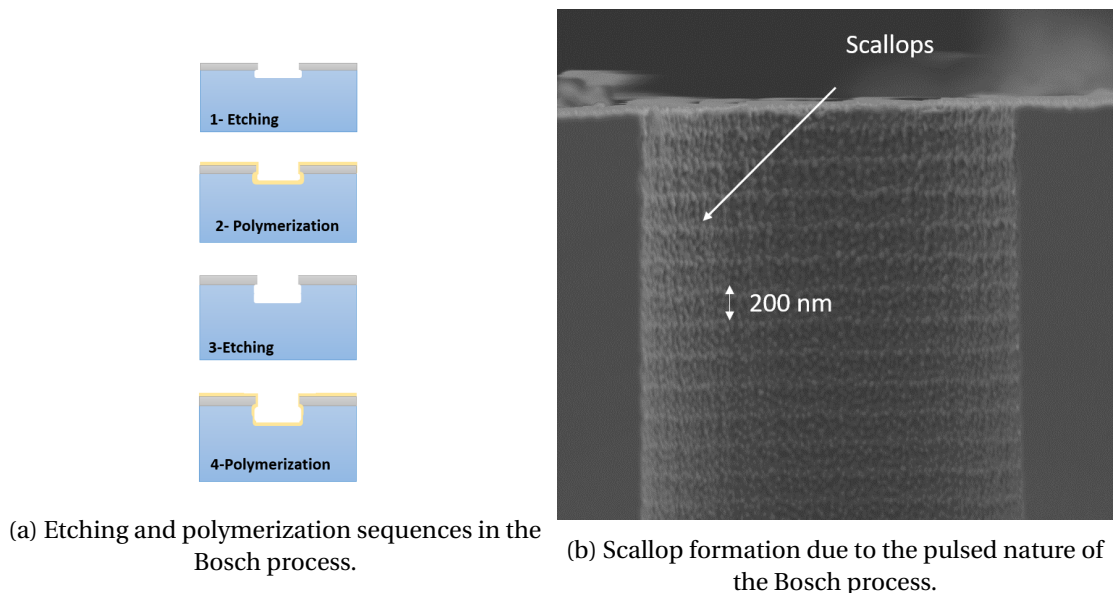


Figure 5.13: Schematic explanation of the Bosch process and typical scallop formation.

In the beginning, chemical etching with an SF_6 is performed for a few seconds. Then the etching gas supply is switched off, and C_4F_8 is introduced, leading to polymerization. During a few seconds, a thin polymer layer is deposited. The next step in the process is again an etching sequence. Due to the substrate bias, the polymer film on the horizontal faces of the structure is quickly removed, and silicon is etched in that direction.

Because there is no electrical field in the horizontal direction, the etching in this direction is a lot slower. Nevertheless, the polymerization step is optimized so that all polymer has disappeared at the end of this second etching cycle. A variation of the Bosch process includes an additional third step where an oxygen plasma removes all polymer residues before each polymerization step, decreasing sidewall defects. This pulsed sequence can be repeated many times resulting in deep holes. The pulsed nature of this process is immediately recognizable by the formation of scallops on the walls shown in Figure 5.13b. The difficulty of etching long and narrow channels lies in restricted gas access. If the mask opening is wider, the etching gas easily goes deeper, and the etching rate increases. This effect is called aspect ratio dependent etching (ARDE). Thus, the total etching time increases significantly for high aspect ratio structures, and a good mask selectivity is needed. A metal mask has been introduced in the previous AMCP generation [54], which can sustain longer etching times without being consumed than the more standard photoresist or oxide masks. The very low etch rate of the metal mask also allows to keep the masking material very thin (<100 nm), so that small features can be implemented. The main drawback of using hard metal masks lies in the problem of micro masking [92]. Small parts of the metal can be sputtered away and may deposit on the bottom of the cavity, generating a local micro mask that is very hard to remove. Also, micro-loading effects exist, which means that two identical structures can have a different etch rate depending on their local environment on the wafer. A hole in a dense pattern where more silicon has to be etched away locally, and therefore more competition for the gas to be consumed, will have a smaller depth than a more isolated hole.

Deep etching of silicon is challenging since the etching recipe has to be optimized for the given geometry to be etched. The maximum achievable aspect ratio and profile of a channel depend on the etching parameters (gas flow rates, RF power, pressure, temperature, substrate bias, and cycle times) as well as the masking material and the type of etching equipment used. Figure 5.14 shows a few examples of typical etching defects encountered during the DRIE process. To prevent striations on the sidewalls of the channels, irregular mask openings must be prevented. This kind of defect was observed when the holes in the mask were fabricated by wet etching. Using a plasma etching with a high anisotropy entirely prevented striations. Another problem is narrowing the channel with depth due to the restricted gas access with higher aspect ratios. This eventually causes an "etch stop" where the etching gas can not entirely remove the passivation layer at the bottom of the channel and thus defines the maximum reachable aspect ratio. Such maximum aspect ratio could be increased by using longer cycle times of the individual etching and passivation gases. Increasing the ion momentum by either decreasing the process pressure or increasing the substrate bias also helps etch the bottom of the channel. Visible bowing in the upper part of the channel is caused by negative charging of the sidewalls near the mask opening [93] and could be minimized by using a low substrate temperature. An unfavorable ratio between the etching and passivation fluxes or cycle times can cause various sidewall defects.

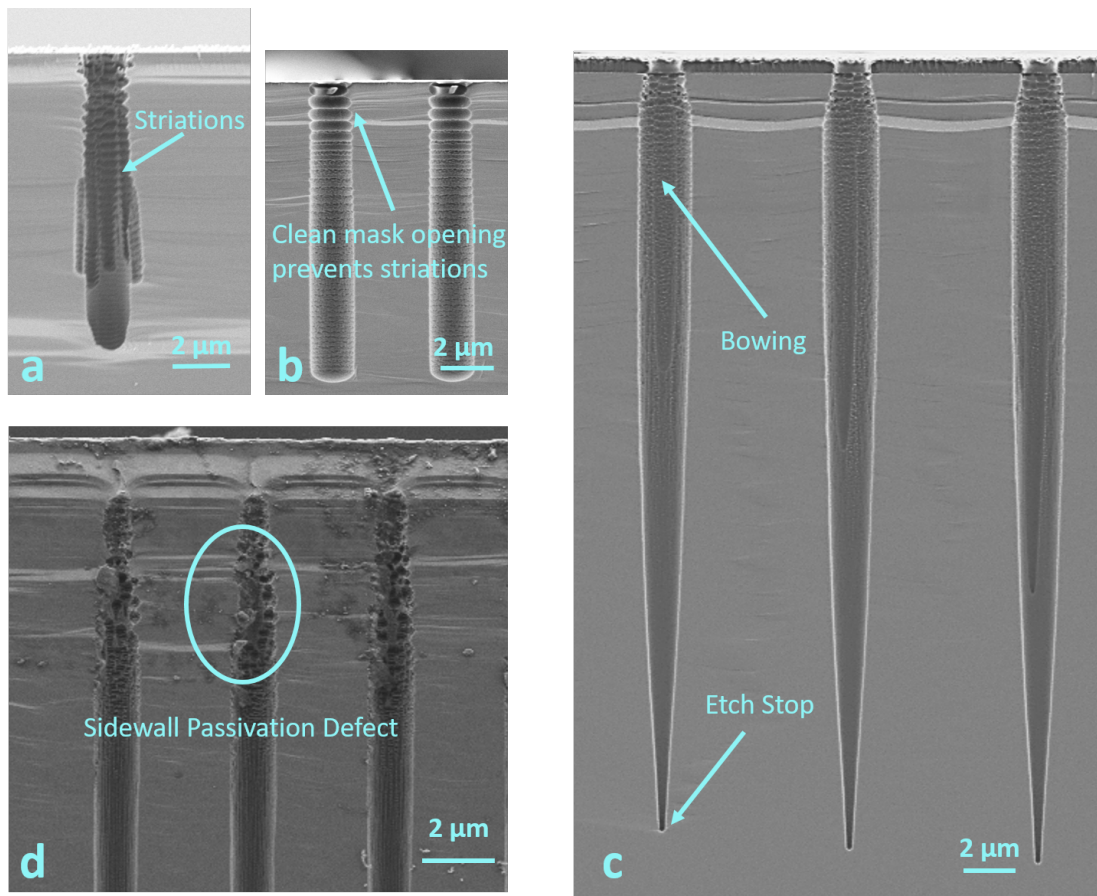


Figure 5.14: Commonly encountered DRIE problems. Striations are formed when slight irregularities in the mask opening are present (picture a)- this typically happens when the mask is etched by a wet etching process. It can be entirely prevented by using a plasma etching step with high anisotropy for the mask openings, as shown in picture b. Image c shows a bowling of the channel and channel narrowing, eventually causing an etch stop. In image d sidewall passivation, defects are shown caused by uneven wall passivation.

The etching recipe used in our process has relatively long cycle times (10 s of etching and 4 s of passivation), allowing the gases to reach the bottom of the channels, and a relatively low substrate bias to minimize the damage to the masking material and preventing micro masking effects. Aspect ratios up to 30 and a small channel diameter between 1.3 and 1.6 μm could thus be achieved. However, the long cycle times of the etching and passivation steps increased the surface roughness inside the channels, an effect usually unwanted in other DRIE applications such as through silicon vertical electrical connection (TSV). In the case of AMCPs, this roughness is thought to be unproblematic and might even be beneficial for the production of secondary electrons. Finally, the etching time had to be calibrated carefully as overetching causes an unnecessary broadening of the channel due to the scattering of the ions. For this reason, the channel diameter within one wafer was kept constant to keep the etching rate as uniform as possible. Figure 5.15 presents the detailed recipe used.

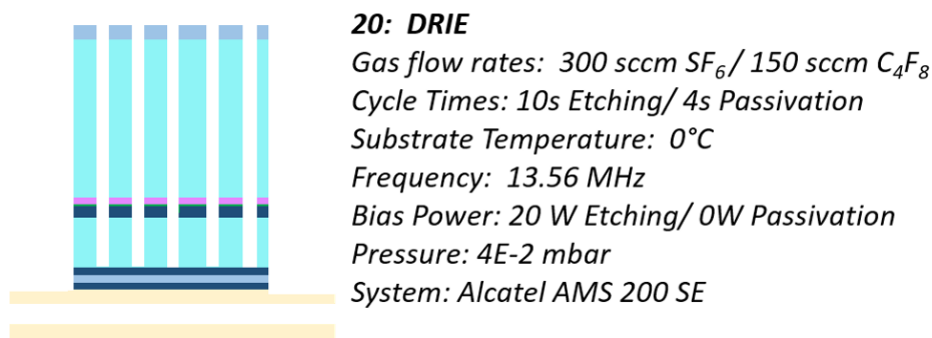


Figure 5.15: Deep reactive ion etching of the channels.

AMCP chip

After the channels have been etched, the wafer was cleaned in an oxygen plasma for 2 minutes to remove all residues from the DRIE process. A photoresist layer was then applied all over the wafer as a protective layer during the dicing process. After dicing a final cleaning step was performed to remove the resist and the chips were then wirebonded to the measurement board. With the improved fabrication process presented in this chapter samples with aspect ratios up to 25 and channel diameter down to $1.6\mu\text{m}$ could be successfully fabricated. A cross-section of the final channels can be seen in Figure 5.16.

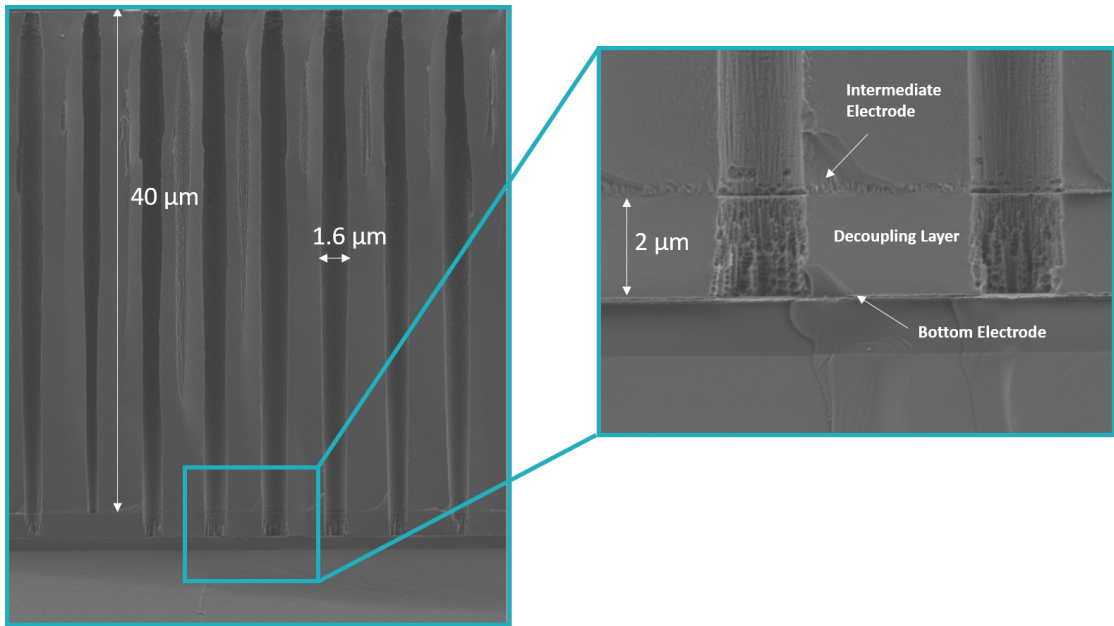


Figure 5.16: SEM image of a final AMCP with an aspect ratio of 25 and channel diameter of $1.6\mu\text{m}$.

5.1.3 High secondary emission layers

In order to increase the gain of AMCPs, one has to either increase the aspect ratio of the channels or increase the number of secondary electrons produced per collision. The maximum secondary yield of hydrogenated amorphous silicon at normal incidence δ_m is around 1.33 to 1.65, depending on the surface morphology [54]. Comparing this with the yields measured for Al_2O_3 ($\delta_m=2.5$) and MgO ($\delta_m=4.8$) [94] illustrates the vast potential of increase in gain by applying channel wall coatings. Al_2O_3 coated samples already proved to boost the gain of AMCP by a factor of two for the same aspect ratio [39].

ALD is used to get a conformal coating of the channel walls. In ALD processes, the thin film is grown by sequential deposition of atomically thin layers of two types of materials. The characteristic of this process is that each of the two reaction steps is self-limiting. This means that the reaction stops once all reactive sites on the wafer surface are occupied. The deposition mechanism comprises four steps, the first precursor is pulsed into the reactor and reacts at the sample surface by chemisorption. Afterward, the reaction chamber is purged with an inert gas (N_2) and the excess precursor removed. The second precursor enters the chamber and reacts with the first precursor already present on the sample's surface. Finally, any byproducts and the excess precursor are purged from the reactor. This cycle can be repeated until the desired thickness is reached.

A 5 nm thick layer of Al_2O_3 is deposited by ALD after the etching of the channels using the two precursor gases tri-methyl aluminum (TMA) and water H_2O . The Al_2O_3 also covers the bottom of the channel where the electrons arrive on the anode, which can affect collection of the electrons. For this reason, an additional dry etching step was performed to remove the layer on the horizontal areas. The process details are given in Figure 5.17.

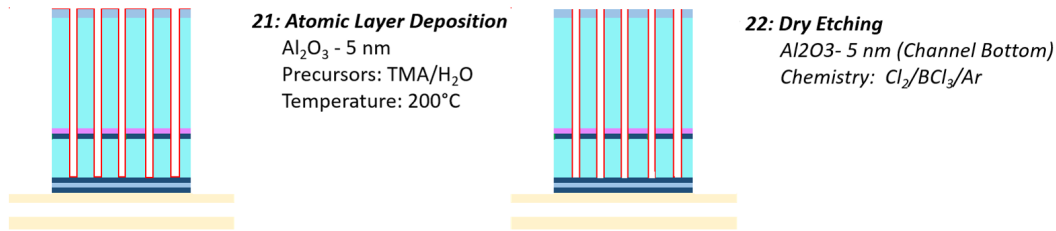


Figure 5.17: Process steps to fabricate Al_2O_3 coated samples. A 5 nm thick layer of alumina is deposited by an ALD process. Afterwards an an-isotropic dry etching step is performed to remove the layer on top of the anode and prevent blocking the signal.

ALD of MgO was not available in our cleanroom facilities at the time of this thesis. A first test deposition was done at the Laboratoire des Matériaux et du Génie Physique (LMGP) in Grenoble using spatial atomic layer deposition (SALD). SALD is an alternative to conventional ALD in which the precursors are continuously injected in different reactor locations, separated by a flow of inert gas, leading to higher deposition rates compared to standard ALD. Figure 5.18 shows a channel with an aspect ratio of 25 coated with a MgO layer of 300 nm thickness. The thickness was increased so the layer conformality could be easier checked under the electron microscope. These first tests resulted in channels covered to the bottom with an increase in thickness towards the top of the channel. As ALD processes for high aspect ratios remain challenging further recipe optimization is currently being performed, and the first samples to be measured should be available in the near future.

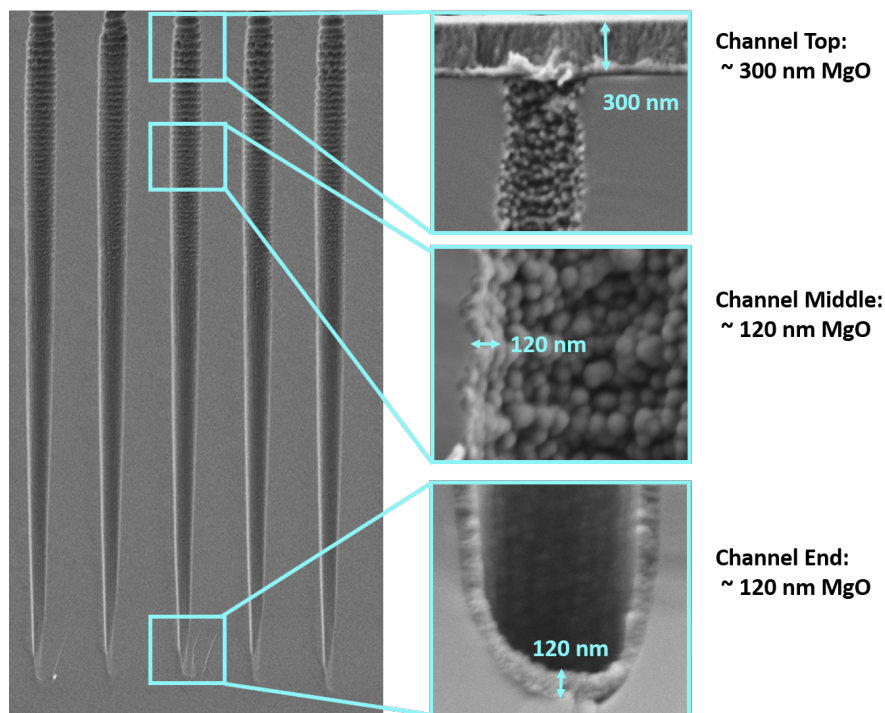


Figure 5.18: MgO layer deposited by SALD. The layer is thicker on top (300 nm) and then quickly decreases in thickness (120 nm) due to the restricted gas access inside the channel.

5.2 Alternative channel geometries

One of the main advantages of AMCPs over conventional glass-based ones is the flexibility of the fabrication process, allowing to adjust the channel shapes to cater to specific applications. In this next section, the fabrication of alternative channel shapes is presented.

5.2.1 Funnel openings

The idea of fabricating channels with a funnel-shaped opening was already introduced in Chapter 3. The collection efficiency of an AMCP is limited by the active area of the sensor. To achieve an open area of around 95 % the channel entrance can be broadened until they start overlapping. From simulation results described in Chapter 4, we know that the funnels should resemble a triangular shape to avoid re-absorption of the produced secondary electrons. To fabricate such structures an isotropic etching step is performed after the DRIE of the channels. Keeping the gas pressure relatively high during the etching prevents the gas from entering too deep into the channels and keeps the lower part of the channels narrow. This is important to retain a high enough gain and optimal timing performance of the detector. To obtain the desired triangular shape the metal mask needs to be removed before this final etching step. The difference in shape between the etching with and without the metal on top is shown in Figure 5.19.

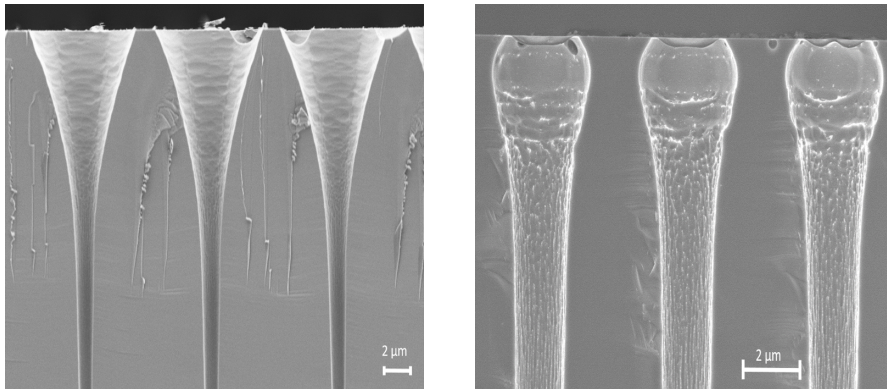


Figure 5.19: Left: Etched funnels with an optimized isotropic etching step. The top metal mask was removed before the funnel etching. The lower part of the channels is only minimally broadened (about 300 nm) during the etching of the funnels to keep aspect ratio and hence multiplication gain high. Right: Same etching recipe with the metal mask still intact. The metal blocks the access for the etchant from the top creating an undesirable rounded shape.

After the etching, an aluminum electrode is again put back on top of the channels. Two different methods have been tested to achieve this. The first option is to directly sputter the aluminum, which results in a nicely covered area, ensuring good conductivity of the electrode. The drawback of this is that the aluminum also enters partially into the funnel. The second method is to use a tilted evaporation process. In this way, the metal layer is more confined to the top of the channel top but risks not having a uniform coverage. The exposed bottom contacts are protected with a layer of P70 resin during the evaporation/sputtering process. Afterward, a 10 nm thick layer of magnesium oxide was sputtered inside the funnels to ensure a high secondary emission at the first impact. Figure 5.20 displays the difference between a sputtered and evaporated electrode for two funnel samples. The process steps details are summarized in Figure 5.21.

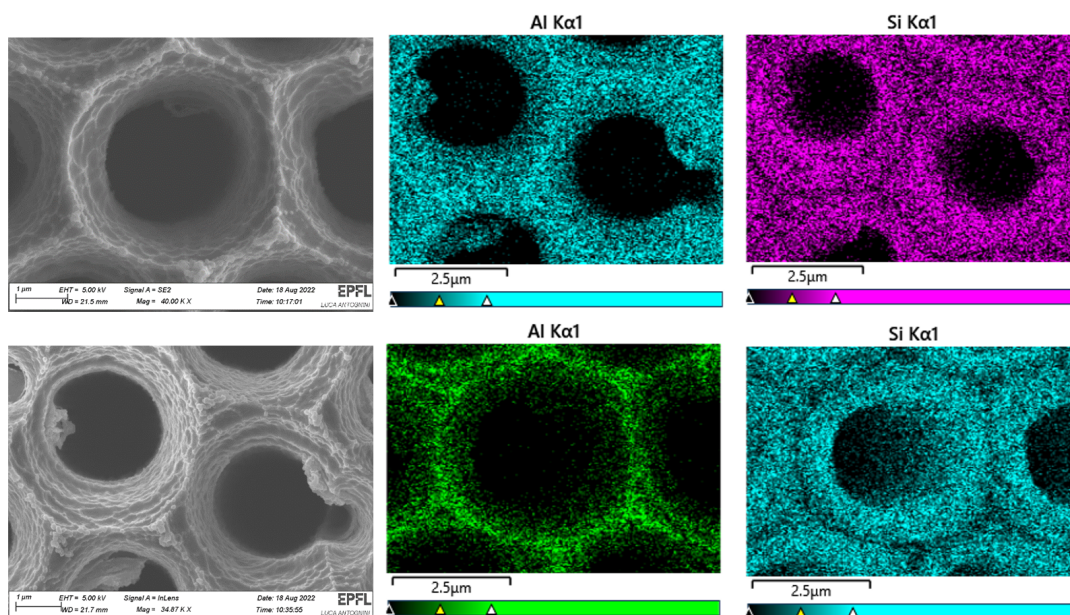


Figure 5.20: Top electrode of two funnel samples. The top row shows a sample where the aluminum was sputtered onto the a-Si:H. For the sample in the bottom row, the metal was evaporated at an angle. The images on the left show the surface of the funnels from the top (SEM image). The images in the middle and on the right show the elemental distribution maps of aluminum and silicon recorded by energy-dispersive X-ray spectroscopy (EDX). It can clearly be seen that aluminum enters deeper into the funnel when it is sputtered. (Images provided by Luca Antognini).

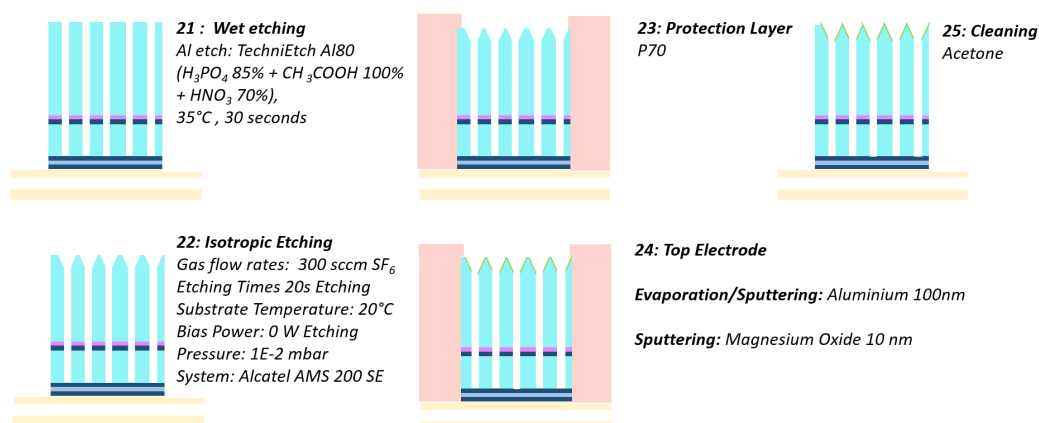


Figure 5.21: Process steps to fabricate funnel shaped openings. First the metal mask needs to be removed, then an isotropic etching step is performed. To make the top metal contact aluminum is sputtered/evaporated onto the funnels. Finally, a MgO layer is sputtered to ensure a high secondary yield at the first impact.

The total thickness of the amorphous silicon stack decreased during the isotropic etch since the layer was exposed to the etching gas from all directions. To minimize this decrease in channel length the pitch of the channels was chosen to be as small as possible so that total isotropic etching time can be kept short. A pitch of 4 μm (center to center) was chosen for the first batch of prototype detectors with a funnel architecture. Resulting in a funnel width of 4 μm . The broadening of the channel (funnel depth) is constrained to the top ~6 μm . The total channel length is 40 μm . An open area of around 95 % could be achieved. The resulting structure is shown in Figure 5.22.

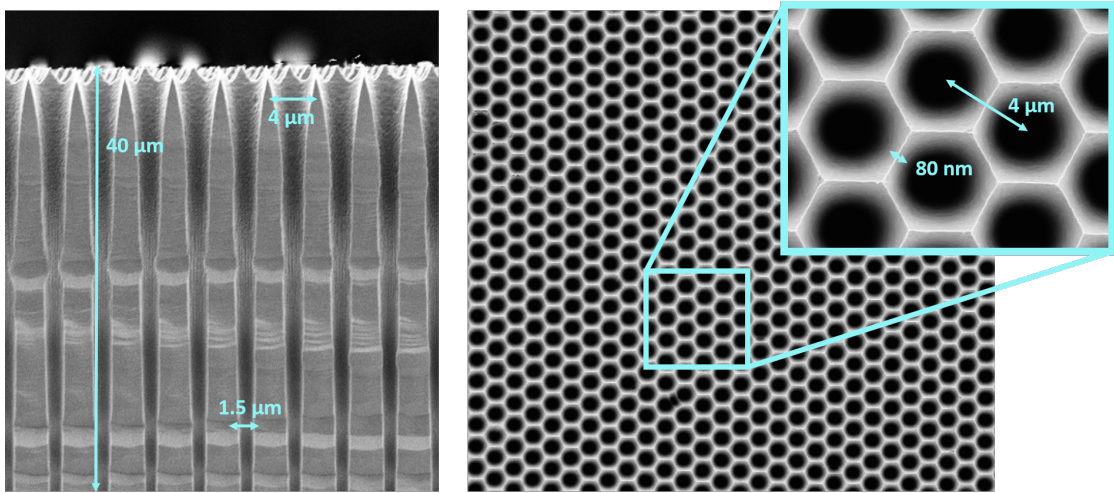


Figure 5.22: Final funnel architecture- Cross-section view (left) and top view (right). Funnels with a width of $4\text{ }\mu\text{m}$ and a depth of around $6\text{ }\mu\text{m}$ have been fabricated. Resulting in an active area of around 95 %. (Note the image shows a test chip that was processed in the same way as the real sample rather than the actual chip. This was done to not destroy any of the actual funnel devices).

5.2.2 Trench AMCPs

The problem with etching high aspect ratios is that at some point the etching will stop at a maximum achievable aspect ratio. This etch termination happens due to the increasingly restricted gas access. At this critical aspect ratio the polymer etch rate is too low to completely remove it during the etching phase. The underlying silicon is not exposed to the etching gas and the etching eventually stops. The aspect ratio at which this happens is determined by the etching parameters but also the geometry of the structure to be etched. Another problem when etching narrow structures stems from ion scattering effects causing sidewall damages and eventually widens the channels. Once the vertical etch rate has slowed down too much, longer etching times only result in significantly damaged sidewalls with only little increase in depth. For the hole geometry used in AMCPs a maximum aspect ratio around 30 could be reached. This value can still be increased by carefully adjusting the parameters during the etching process. To increase the aspect ratio further a test sample was fabricated using a trench geometry shown in Figure 5.23. The gas can reach the bottom of the trench much easier for this geometry and aspect ratios over 40 could be achieved. Simulation results presented in Chapter 4 have shown that the loss in gain due to the larger opening to the side is around 10 % with respect to a regular round channel with the same aspect ratio. Because the achievable aspect ratio is considerably larger than for holes an AMCP using this kind of geometry could result in a much higher multiplication gain. The main drawback of this design is the loss of spatial resolution in one direction, given by the length of one stripe. For holes the spatial resolution is given by the pitch between the channels and can be as low as 2- 3 μm . However, since the spatial resolution is in any case limited by the electronic readout below the AMCP, this sort of geometry could be a plausible option. The trench geometry could also be further optimized to limit the length of the stripes in the other direction.

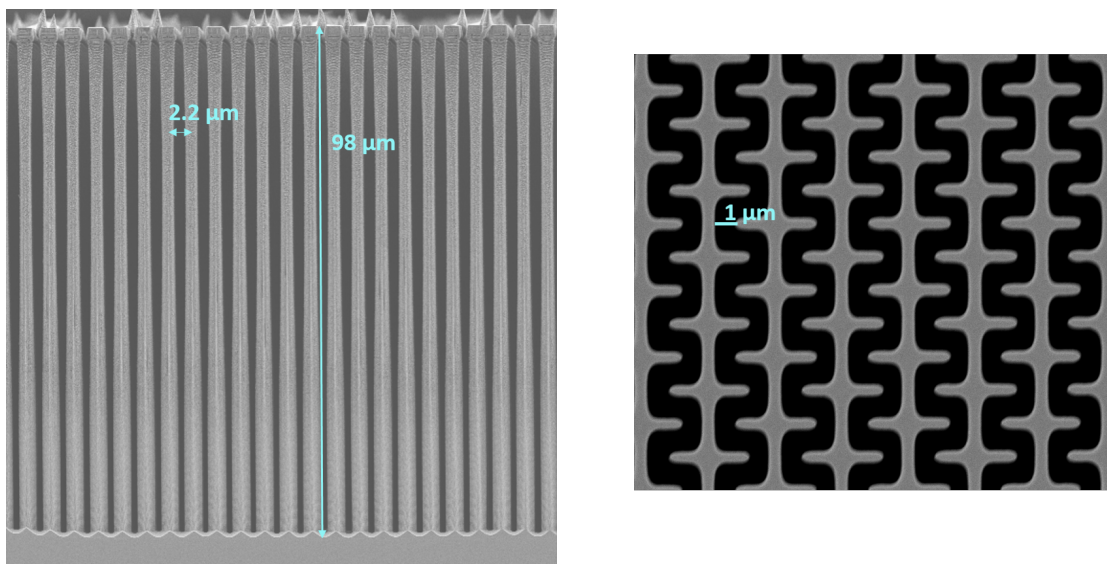


Figure 5.23: AMCP with trench channels. The easier gas access allows etching aspect ratios over 40.

5.2.3 Low capacitance samples

For specific applications, for instance when fast timing properties are required, it is crucial to keep the detector capacitance as low as possible. In AMCPs, the total capacitance is dominated by the one arising from the decoupling layer and the grounded intermediate electrode. This adds a parallel capacitance to the signal output. Its value can be estimated in a first approximation as the capacitance of a parallel plate detector:

$$C_{AMCP} = \frac{\epsilon_0 \epsilon_D A}{d}. \quad (5.5)$$

In our case, A is the area of the anode, and d is the thickness of the decoupling layer. The vacuum permittivity ϵ_0 is equal to $\approx 8.85 \cdot 10^{-12} \text{ F m}^{-1}$. The dielectric constant ϵ_D of silicon is 11.8. For a-Si:H, this value may vary depending on the deposition conditions. More details on the capacitance calculations are given in Chapter 6. It is clear from equation 5.5 that the capacitance can be decreased by increasing the thickness of the decoupling layer. One issue when increasing the decoupling layer is a decrease in the effective channel length. Since no electric field exists between the middle electrode and the anode, this part of the channel does not contribute to the multiplication avalanche but still needs to be etched during the DRIE process. Another problem is the potential increase in charging effects when the decoupling layer thickness is bigger. To reduce these issues, the channel openings in the decoupling layer were etched separately from the upper part of the channel. With the channel diameter being small, the gases do not enter the etched openings during the growth of the main a-Si:H layer. The duration of the polishing step after the PE-CVD deposition of the thick amorphous silicon layer had to be increased to remove the steps formed in the larger openings on the step. Besides that, all the other process steps stayed the same as described earlier. Figure 5.24 illustrates the additional process steps.

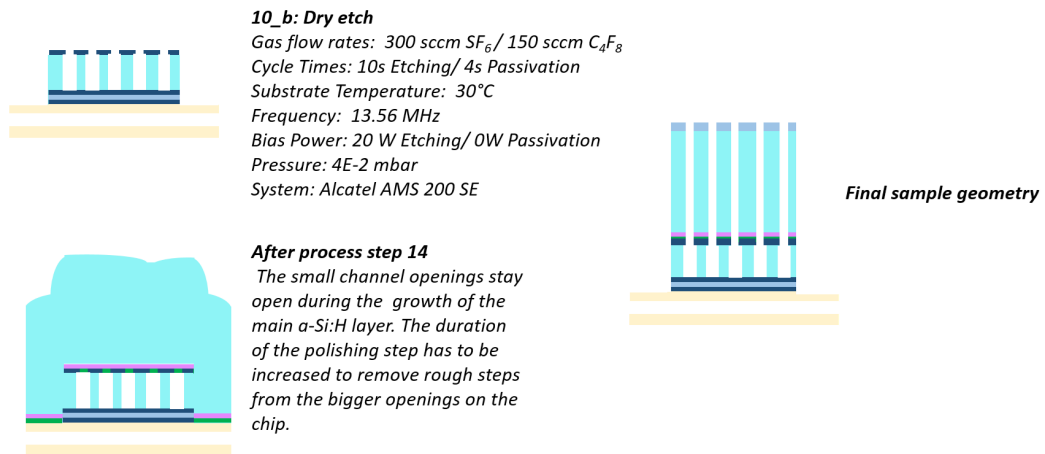


Figure 5.24: Process steps to fabricate AMCPs with a decreased capacitance. The decoupling layer is etched before the deposition of the multiplication layer, resulting in broader channel openings at the bottom and the possibility of increasing the thickness of the decoupling layer.

With the end of the channels already etched, the decoupling layer can be increased to 3- 4 μm without causing a decrease in the final aspect ratio. Additionally, the lower diameter of the channel can be increased, lowering the chances of the electron avalanche colliding with the decoupling walls and hence reducing potential charging effects. The resulting channels are shown in Figure 5.25. The decoupling layer in this sample was increased from 2 μm to 3 μm , reducing the capacitance by a factor of 1.5. The channel diameter in the decoupling layer is 2.5 μm , whereas the upper part of the channel maintains an opening of 1.6 μm . The effective aspect ratio is 26.8. This low capacitance fabrication process was eventually used for the first set of chips designed to be implemented into a Planacon tube. A further increase to a 4- 5 μm thick decoupling layer is possible as long as no raise in wall charging is observed and should be investigated for future AMCP generations.

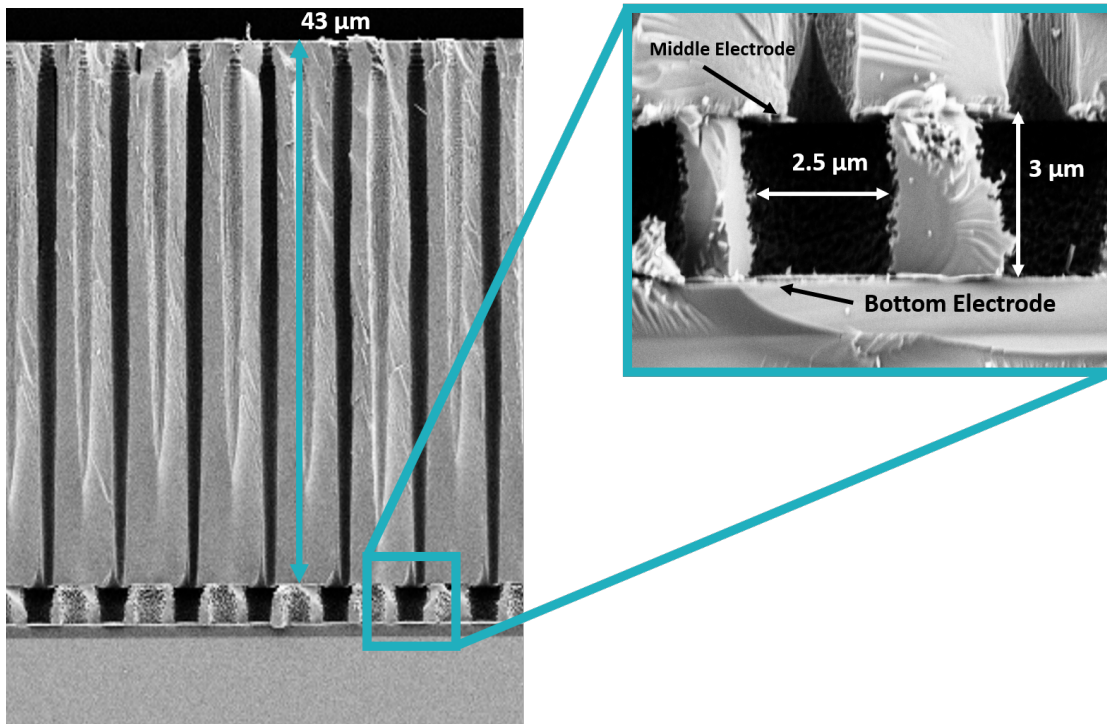


Figure 5.25: AMCP with a thicker decoupling layer that was pre-etched before growing the main multiplication layer.

Other possibilities to further decrease the capacitance of the AMCPs include changing the shape of the intermediate electrode to only be present in a small area around the channel, as illustrated in Figure 5.26. Designing the middle electrode this way would effectively reach a very low capacitance of only a few pF, even for larger anode areas. However, the effect of this change on the leakage current evacuation needs to be carefully investigated. Another possibility would be to exchange the a-Si:H decoupling layer with a material that has a lower dielectric constant such as silicon carbide (SiC) or silicon oxide (SiO). Both of these options should be explored in the further optimization of the AMCP architecture.

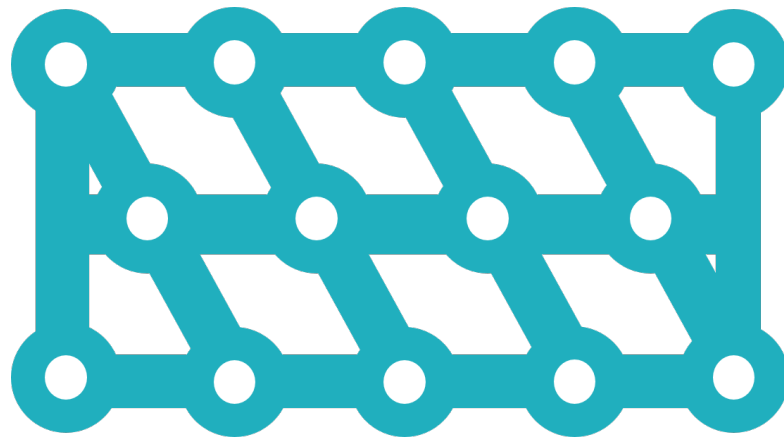


Figure 5.26: Example of an alternative design of the intermediate electrode to decrease the capacitance. The effect of the design change on the leakage current needs to be further investigated and the width of the metal area adjusted accordingly.

5.2.4 Tilted channels

One big disadvantage that AMCPs still have in comparison to conventional MCPs is the absence of a bias angle of the channel. Having tilted channels improves both detection efficiency as well as the overall gain by preventing electrons from passing straight through the channels without colliding. Although not standard, different possibilities have been reported to achieve tilted channels. A faraday cage inside the chamber can modify the ion trajectories and cause etching at an off-normal angle [95]. Another interesting solution was found by attaching a piece of glass close to the pattern to be etched. The glass will get charged during the etching, which also affects the direction of the incoming ions [96]. A very easy way to achieve a slight tilt is by purposely causing a slight bow to the wafer (this can be achieved by depositing a high stress layer on the backside of the wafer). The wafer surface will then have a slight angle with respect to the ion flux, causing a channel tilt angle of a few degrees. An example of a channel with a 3° tilt is shown in Figure 5.27. Although this method is very straightforward the maximum tilt angle is limited by the maximum bow of the wafer. If the wafer bends too much other etching conditions might be affected. Additionally, the angle of the channels is not the same for the whole wafer surface. Nevertheless, tilted channels should be investigated further in future device optimization.

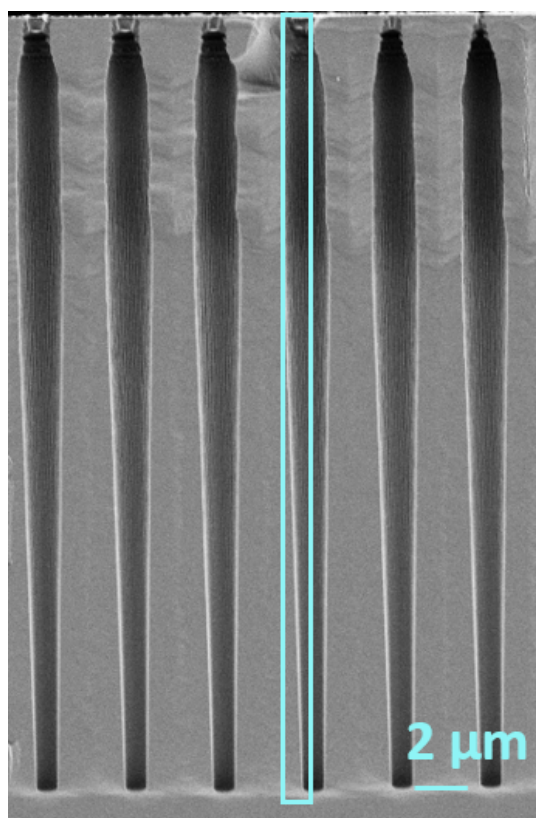


Figure 5.27: Example of etched channels with a bias angle of around 3° , achieved by slightly bending the wafer.

5.3 Conclusion and outlook

This chapter presented the improved fabrication process for the 5th generation of AMCP. By optimizing the a-Si:H deposition to grow layers with less structural defects and lower stress value and improving the DRIE process, the aspect ratio could be increased to 25. Channel diameters were reduced down to 1.6 μm to achieve an optimum timing resolution of the AMCPs. Replacing the $\mu\text{c-Si}$ intermediate electrode with a chromium-based one helped to prevent a voltage rise on this electrode. High aspect ratio samples (25) with an ALD deposited alumina coating were also fabricated, and the first steps in achieving MgO coated samples were taken. In the second part of the chapter, alternative AMCP geometries were explored. Introducing an isotropic etching step after the DRIE process allows the channel openings to be broadened to achieve a funnel-shaped appearance. A first device with funnel shaped openings was fabricated. The open area of the detector was increased from ~5- 10 % to around 95 % while maintaining a reasonable channel length of 40 μm . A first test was done using a trench geometry instead of holes. Like this, aspect ratios over 40 could be achievable, making this channel geometry an alternative for applications where high gain values are needed. After this initial proof of concept the trench geometry should be further optimized to fabricate a fully functioning device. Lastly, detectors with a decreased output capacitance were fabricated by etching the holes in the decoupling layer separately. These devices were later used for the integration in the planacon phototube and to perform the timing resolution measurements due to their reduced capacitance.

For future AMCP generations the aspect ratio can still be increased to around 35- 40 by adjusting the parameters during the etching. This will be especially important for the funnel-shaped samples, where the total layer thickness is decreased by 2- 3 μm during the isotropic etching step. The capacitance can additionally be further decreased by redesigning the intermediate electrode. Using a material with a lower dielectric constant, such as SiC or SiO for the decoupling layer could also be envisioned. To achieve higher gain values the ALD deposition of magnesium oxide needs to be optimized. Alternatively, trench shaped AMCPs with high aspect ratio could also help to significantly enhance the gain. To take full advantage of the flexible fabrication process, the possibility of directly depositing a photocathode on top of the AMCP should also be explored in future devices. Efficiencies of integrated photocathodes can be much higher than having the standard arrangement with a vacuum gap between AMCP and photocathode. Having the photoelectrons produced close to the channel entrance results in higher spatial and temporal resolution since the travel distance until the start of the electron multiplication process is short. Additionally, photocathodes operated in reflective mode are usually more efficient than in the semitransparent mode and are better protected from erosion due to ion fluxes from the channels. Potential photocathodes include gallium nitride (GaN) and metallic-based ones (gold, aluminum, chromium) that can be easily deposited directly on the AMCP. Lastly, possibilities to etch channels with a bias angle relative to the top electrode should be investigated. Having tilted channels could further increase the gain and detection efficiency by avoiding to have electrons passing through the channels without colliding.

6 Characterization of AMCPs

In this chapter, the characterization of the fabricated samples is presented. The first part of the chapter discusses the capacitance between the intermediate electrode and the anode and conductivity measurements of the multiplication layer between top and intermediate electrode. The second part of the chapter consists of the multiplication gain measurements for devices from the 3rd and 5th AMCP generations.

6.1 Capacitance measurement

The problem of the AMCP capacitance was already introduced in Chapter 5. The grounded intermediate electrode causes a parallel capacitance C_1 to the anode, as illustrated in Figure 6.1, which affects the outgoing signal.

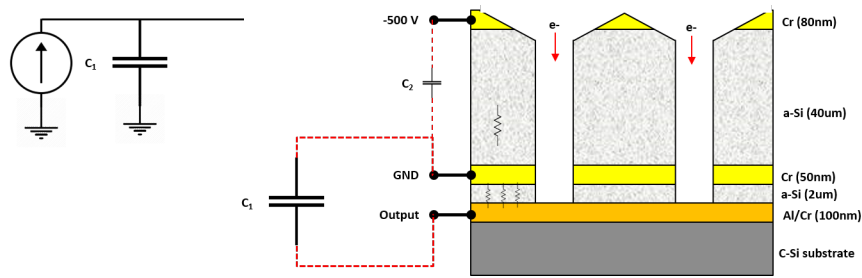


Figure 6.1: Parallel capacitance caused by the presence of the grounded intermediate electrode.

This capacitance is not problematic for the characterization methods discussed in this thesis. However, in the final envisioned TOF/PET detector, a high capacitance increases the signal rise time and negatively affects the achievable time resolution. It is therefore important to investigate possible options to minimize this capacitance. The most straightforward one is to increase the thickness of the decoupling layer as it was done for a set of fabricated devices (referred to as the Planacon2 series).

For that series, the decoupling layer thickness T_D was changed from the standard $2\mu\text{m}$ to $3\mu\text{m}$ in these chips. The capacitance between the ground and the signal anodes was then measured for chips from the Planacon2 series and devices that were fabricated using the standard process and with a decoupling layer thickness of $2\mu\text{m}$ (referred to as MCP152 series). The measurements were conducted with an impedance analyzer (Agilent 4294) over a wide range of frequencies. A typical measurement for the mid-size pixel ($500\mu\text{m}^2$ area) of the MCP152 series is shown in Figure 6.2. The results of all the measured pixels are summarized in Table 6.1.

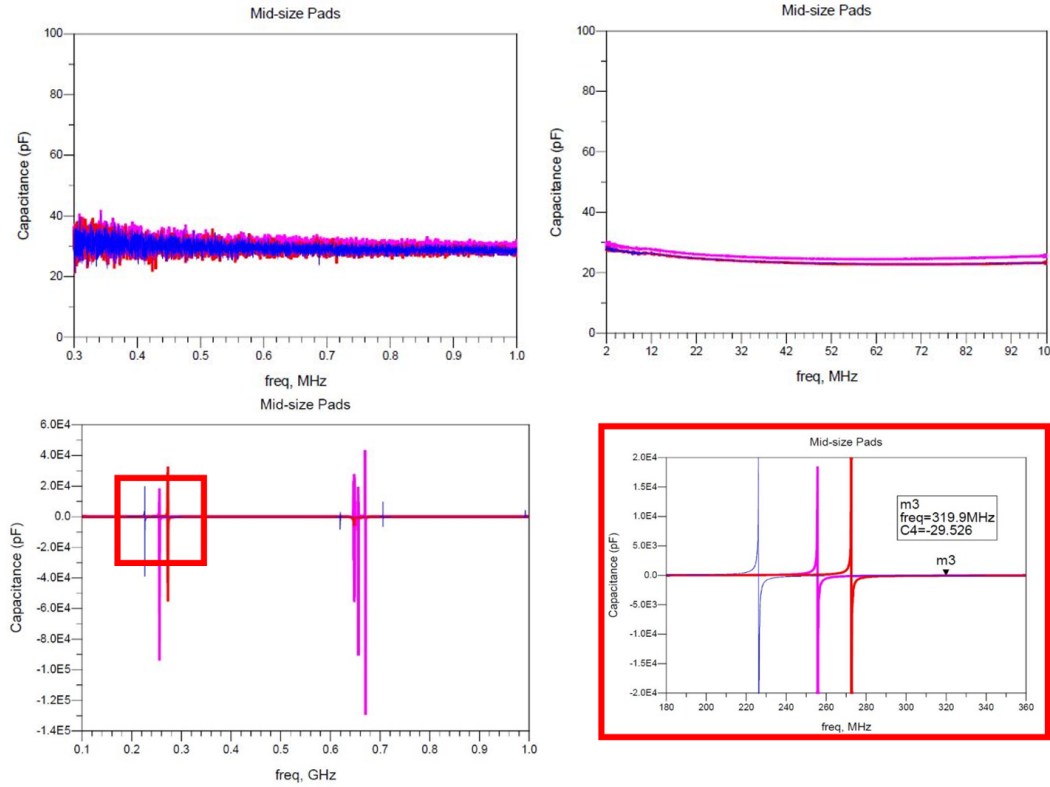


Figure 6.2: Capacitance measured for a medium-sized pad ($500\mu\text{m}^2$) of the MCP152 series over a range of frequencies. A capacitance of (29.5 ± 0.2) pF was measured for three different pixels. Some resonances are present at high frequencies that are most likely caused by contributions of the pins and wirebonds.

First the capacitance of the cables and printed circuit board (PCB) was measured without the chip and saved as the zero reference on the system to subtract their contributions to the final measurement. Comparing the measurements in Table 6.1 between the two device sets shows an inverse proportionality between the capacitance and the decoupling layer thickness ($C_1 \propto 1/T_D$) that was expected from the parallel plate approximation (Equation 5.5). It does however not scale with the area of the pads. Most likely the capacitance does not behave exactly like a parallel plate capacitor due to the presence of the channels.

There was also a contribution of the wirebonds that could not be separated from the sensor capacitance in this measurement. Some resonances could be observed at high frequencies. They were already observed during the zeroing of the system with just the cables and the measurement board and are hence most likely caused by the pins and other components on the PCB.

Table 6.1: Measured capacitance

Measured capacitance for different devices and pad sizes			
Device	T_D	Area	Capacitance
MCP152	$2\text{ }\mu\text{m}$	$500\text{ }\mu\text{m}^2$	$(29.5 \pm 0.2)\text{ pF}$
		$1000\text{ }\mu\text{m}^2$	$(45 \pm 2)\text{ pF}$
Planacon2	$3\text{ }\mu\text{m}$	$500\text{ }\mu\text{m}^2$	$(19.8 \pm 0.2)\text{ pF}$
		$1500\text{ }\mu\text{m}^2$	$(95 \pm 2)\text{ pF}$

Given the lower capacitance value of the Planacon2 devices makes this fabrication geometry is the best choice for the integration inside the Planacon vacuum tubes and the first timing measurements described in Chapter 7.

6.2 AMCP conductivity

The conductivity of the amorphous silicon layer is a critical parameter for its application in AMCPs. The layer needs to be conductive enough to replenish the lost charges during the multiplication phase but still needs to sustain large bias voltages without the risk of causing an electrical breakdown. The dark conductivity of an intrinsic a-Si:H layer strongly depends on the deposition parameter and impurity content and can vary between $\sigma_{dark} = 10^{-10} - 10^{-12}\text{ }\Omega^{-1}\text{cm}^{-1}$. First, the dark conductivity of an a-Si:H layer deposited on a glass substrate was measured as a function of temperature under a nitrogen atmosphere of 1 mbar. Two aluminum electrodes were evaporated on the layer for the contacts. The temperature was first increased to 180°C and then slowly cooled down to ensure accuracy of the temperature measurement and to guarantee defect thermal equilibrium. The dark conductivity at room temperature was extrapolated from the cooling part of the curve. From this measurement a conductivity of $\sigma_{dark} = 6.1 \cdot 10^{-11}\text{ }\Omega^{-1}\text{cm}^{-1}$ was found. The measurement plotted in an Arrhenius plot can be seen in Figure 6.3 (left). This value is representative of the conductivity of the a-Si:H layer with the current deposition parameter used in the AMCPs fabricated during this thesis. In the final AMCP device, the conductivity is influenced by the presence of the channels inside the layer. As mentioned in Chapter 2, conductivity on the surface of an a-Si:H material can be enhanced due to the additional localized states existing near the surface. Previous publications already presented an indication of a preferential conduction path along the channel surface [19]. The conductivity between the top electrode and the grounded intermediate electrode for an AMCP with a layer thickness of $40\text{ }\mu\text{m}$ was calculated from the I-V characteristics.

Figure 6.3 (right) shows the current on the intermediate electrode as a function of the applied bias voltage. The resistance R of the multiplication layer can then be estimated from the slope of the linear portion of the curve. From this $R=35\text{ M}\Omega$ was found. The conductivity can be calculated by taking into account the thickness $T_{aSI}=40\text{ }\mu\text{m}$ and the area $A=51.3\text{ }\mu\text{m}^2$ of the amorphous silicon layer (entire area minus the area of the channels):

$$\sigma_{IV} = \frac{T_{aSI}}{R \cdot A}. \quad (6.1)$$

From this, a conductivity of $\sigma_{IV} = 2.21 \cdot 10^{-10} \text{ }\Omega^{-1}\text{cm}^{-1}$ was found, which is, in fact, considerably larger than the measured dark conductivity. This supports the hypothesis of enhanced conduction along the channel walls. Another thing worth noting is the more than linear increase in current for voltages larger than -200 V. This behavior was also observed in earlier measurements [19] and was attributed to an additional conduction mechanism for large electric fields, most notably the Poole-Frenkel effect [97], which describes the field-enhanced thermal emission of trapped carriers in a resistive element. The behavior could also be connected to the space-charge-limited current (SCLC) effect [98], [99]. The here-found values for the conductivity can serve as a reference point for future optimizations of the AMCP layer stack and can help to estimate the maximum bias voltage that can safely be applied to an AMCP.

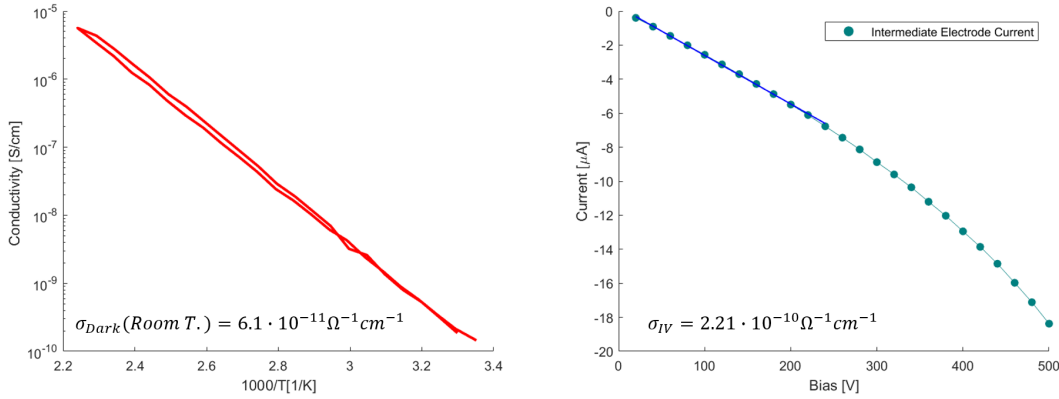


Figure 6.3: Left: Measurement of the a-Si:H layer conductivity in the dark as a function of temperature. A dark conductivity at room temperature of $\sigma_{dark} = 6.1 \cdot 10^{-11} \text{ }\Omega^{-1}\text{cm}^{-1}$ was found. Right: I-V characteristics of the multiplying stack, the conductivity can be estimated from the ohmic resistance at biases below 200 V. From this measurement a conductivity of $\sigma_{IV} = 2.21 \cdot 10^{-10} \text{ }\Omega^{-1}\text{cm}^{-1}$ was calculated.

6.3 Gain characterization

One of the most crucial parameters is the multiplication gain inside the channels. As discussed earlier, this gain depends on the aspect ratio of the channels, the secondary emission coefficient of the material on the channel walls, and the maximum bias voltage that can be applied. In this section, the gain measurements of the fabricated AMCP devices are described in detail.

6.3.1 Setup description

To allow for a convenient characterization AMCPs were fabricated in chip-like test structures. Each chip had several independent pixels of three different sizes. The test design was further updated for the 5th generation to include smaller sensor areas and shorter connection paths. Additionally, a grounded area around the anode pads was added to serve as a guard ring. These changes were motivated by the planned gain measurements in transient regime. These chips were then wire-bonded to a double-sided interface board. The interface board itself was also redesigned to use subminiature version A (SMA) connectors, instead of the previous connection pins, to better shield the outgoing signal. The two test designs (AMCP and related interface board) for the previous generation and the latest one are shown in Figure 6.4.

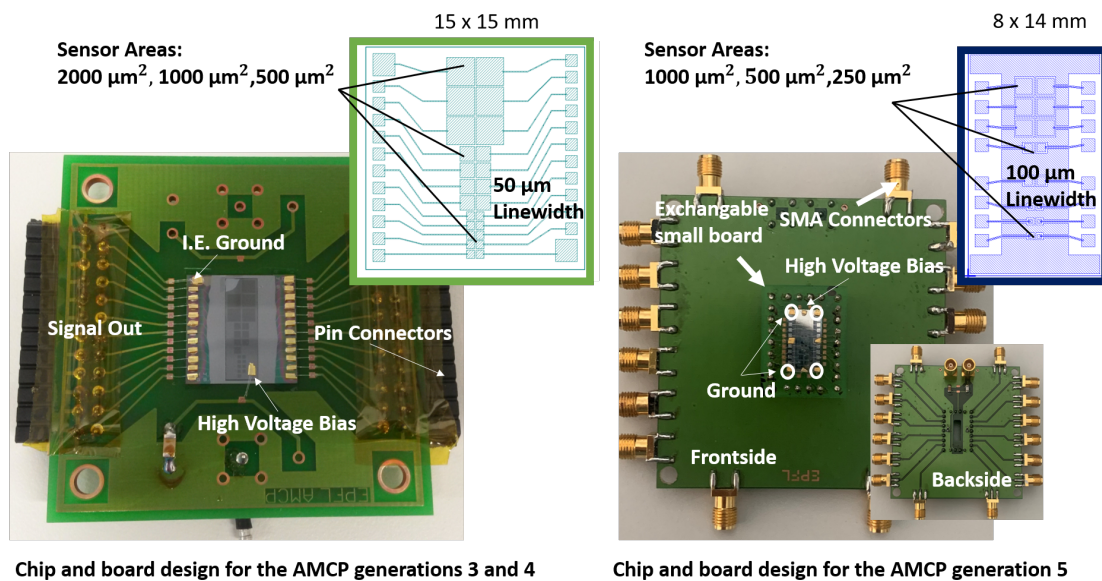


Figure 6.4: Chip design and interface board for the characterization measurements. Left: Previous structure that was used for the measurements up to the last generation. Right: New design of the test chip and board that was optimized for transient measurements.

A custom-designed setup was used to test the multiplication gain of the AMCPs under similar conditions to possible applications of the detectors. The full details of the setup are described in a previous thesis [19]. A schematic of the system is shown in Figure 6.5. It consisted of a vacuum vessel with an optical window made of fused silica. The device to be tested was then placed on a rotatable support rod. A rotary dry pump and a turbomolecular pump allowed reaching a residual pressure of $5 \cdot 10^{-6}$ mbar. Two feed-through connectors were implemented to provide the electrical connections. Two different illumination sources could be used for the characterization. A Pen-Ray mercury-vapor lamp provided continuous or chopped UV light with the main emission peak at 254 nm. To test the AMCP response in the transient regime, a pulsed laser source (neodymium-doped atrrium aluminum garnet (Nd:YAG)) was used with a wavelength of 266 nm, a pulse duration of 7 ns (FWHM), and a tunable repetition rate between 1 and 4 kHz. The laser beam was directed into the vacuum chamber by a set of optical mirrors. A thin (16 nm) gold film that was sputtered on a quartz glass served as a photocathode and was placed above the AMCPs at a distance of around 2 mm. This gold photocathode was chosen because of its longevity and stability in air in contrast to most high efficient photocathodes like caesium iodide (CsI), whose efficiency vanishes quickly upon exposure to air. Additionally, a thin metal plate with an opening in the middle, used as photoelectron screen (or mask), was places between the photocathode and the AMCP to shield the bonding pads and wires from stray electrons.

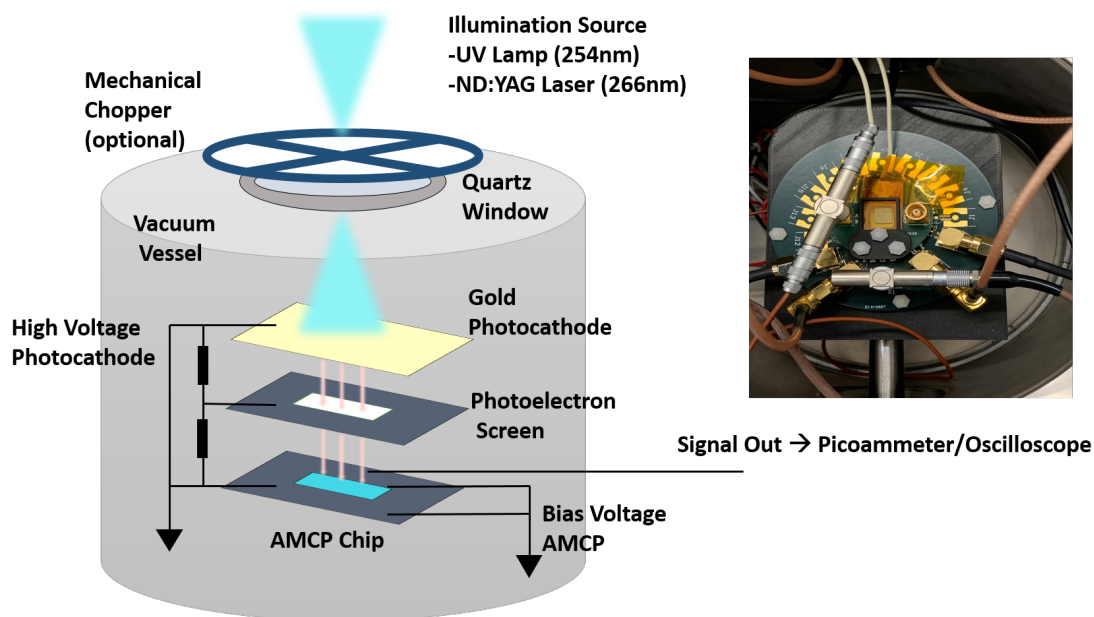


Figure 6.5: Schematic representation of the AMCP test setup (left). The AMCP board was placed in a vacuum vessel. Either a UV lamp or a laser was used as an illumination source. The light entered the chamber through an optical window onto a gold photocathode. A photoelectron screen shielded the bonding pads and wires from the incoming photoelectrons. Photograph of the inside of the chamber (right).

The work function of gold has been reported to be between 4.25 to 5.1 eV [100], [101]. This means that photons with a wavelength of 254 nm (4.88 eV) and 266 nm (4.66 eV) have only a minimal energy to produce photoelectrons, resulting in a low quantum efficiency (maximum 0.1 % at 254 nm). A potential difference could be applied between the photocathode and the AMCPs to accelerate the generated photoelectrons towards the AMCP. The photoelectron screen bias was set right between the AMCP and the photocathode bias to ensure a homogeneous field. The voltage for both the photocathode and the photoelectron screen was provided by a Stanford Research Systems PS310 high-voltage supply. The bias voltage for the AMCPs was supplied by a Keithley 617 picoammeter. The anode signal was then measured either by the same Keithley 617 picoammeter for the measurements under continuous illumination or with an oscilloscope (Teledyne LeCroy wavesurfer 510) for the pulsed measurements. For the measurements of the 3rd generation devices a mechanical chopper was additionally placed between the UV-pen and the optical window. The chopper frequency was then coupled to a lock-in amplifier to read out the anode signal. This step was necessary due to the low gain of these samples and hence low SNR ratio. For the measurements of later generations this step was no longer necessary.

6.3.2 Calibration of the photocathode

Before the gain of the AMCPs could be evaluated, the incoming electron flux from the photocathode needed to be measured. As the quantum efficiency of the photocathode is dependent on the fabrication parameters this flux had to be recalibrated whenever the photocathode was exchanged. Additionally, a decrease in the efficiency of the photocathode has been observed over a timespan of a few months that was most likely caused by physical handling during the exchange of test devices. For this reason the photocathode was replaced at regular intervals. In this following segment the calibration procedure of the photocathode is briefly described. To calibrate the incoming flux a test sample consisting of several aluminium pads of different sizes was used. The photocathode was then placed about 2 mm away from the calibration sample and illuminated either by the mercury lamp or the laser source. The current arriving on the different pads was measured as a function of the applied bias between photocathode and the metal pads. The resulting flux of electrons per second and m^2 under continuous illumination is shown in Figure 6.6.

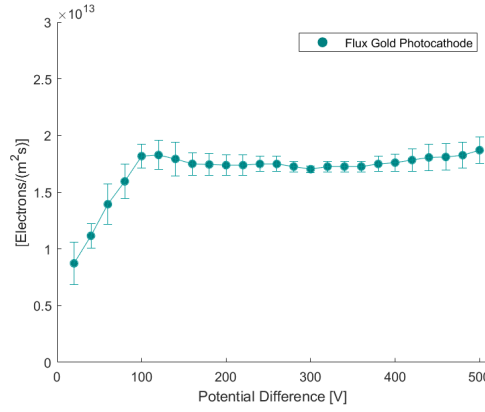


Figure 6.6: Measured flux of photoelectrons from a gold photocathode. A UV lamp was used as a continuous illumination source. The potential difference between the photocathode and the calibration sample was changed between 500 V and 20 V.

The applied electric field helped to steer the photoelectrons onto the pads. An average flux of $1.79 \pm 0.05 \cdot 10^{13} \text{ e}^- \text{ m}^{-2} \text{ s}^{-1}$ was found for voltage differences between 100 V and 500 V. Below 100 V the flux started to decrease and became more unstable. From this flux measurement a quantum efficiency of around 0.0014 % was estimated for a wavelength of 254 nm, which is lower than the 0.0042 % from previous measurements. This difference could be related to the fabrication process of the photocathode, such as the layer thickness uniformity or the presence of impurities.

A similar procedure was performed to calibrate the response to a laser pulse. The laser pulse had a beam spot diameter of around 2 mm that was focused on the photocathode on top of the calibration pads. A typical recorded signal is shown Figure 6.7(left). Physical damage on the gold photocathode was observed at the positions where the laser beam had been focused. A variable intensity filter was used to attenuate the beam during measurements to increase the lifetime and flux stability of the photocathode. During all the measurements under laser illumination the voltage was measured rather than the current. The equivalent current was roughly estimated from the voltage pulse and assuming a 50Ω resistance. With this a photocathode quantum efficiency of only $3 \cdot 10^{-8}$ was estimated, which is significantly lower than the calculated value for the continuous illumination source despite of the small difference in wavelength ($\lambda_{Laser} = 266 \text{ nm}$).

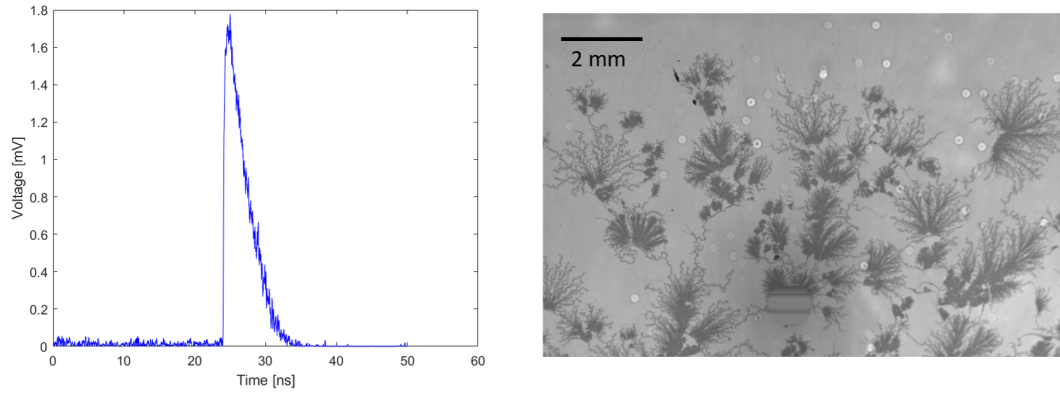


Figure 6.7: Left: Measured laser signal on the calibration sample (signal was inverted for the image). Right: Optical microscope image of the damage on the photocathode caused by the laser beam.

Once the incoming current had been properly calibrated the gain was then defined as the ratio between the output current (I_{Out}) and the incoming photoelectron flux (PF_{In}) times the OAR of the device:

$$Gain = \frac{I_{Out}}{PF_{In} \cdot OAR} \quad (6.2)$$

The resulting gain then represents the average multiplication factor of one channel.

6.3.3 Gain measurements of the third generation of AMCPs

A series of devices from the third AMCP generation (see Table 5.1 for further explanations of the different generations), fabricated back in 2014 and not fully characterized, were measured using the described setup. Their aspect ratios were relatively low (between 11.5 and 13.6). One of the chips had been additionally coated with a thin (5 nm) layer of alumina that was deposited by ALD. Due to their low gain a mechanical chopper and Lock-In amplifier was used to reduce the noise in the measurements. The characteristics of the measured devices and the measurement conditions are summarized in Table 6.2.

Table 6.2: Properties of characterized AMCPs and measurement conditions

	MCP40cc2	MCP40rc3	MCP34cc2
Generation	3	3	3
Notes	Year- 2014	Year-2014	Year-2014; ALD
Layer Thickness	89.9 μm	89.9 μm	73.5 μm
Hole Diameter	6.6 μm	7.7 μm	6.4 μm
Aspect Ratio	13.6	11.7	11.5
Open Area Ratio	13.25 %	29.29 %	14.82 %
Pressure	$3.1 \cdot 10^{-6}$ mbar	$4.2 \cdot 10^{-6}$ mbar	$3.5 \cdot 10^{-6}$ mbar
Lock-In Frequency	125 Hz	125 Hz	125 Hz
Photocathode Bias	-1000 V	-1000 V	-1000 V
Flux [$\text{e}^{-}\text{s}^{-1}\text{m}^{-2}$]	$6.7 \pm 0.05 \cdot 10^{13}$	$6.7 \pm 0.05 \cdot 10^{13}$	$6.7 \pm 0.05 \cdot 10^{13}$

Between each measurement the samples were annealed for 30 minutes at 90 °C. This was done to speed up the release of trapped charges in the localized states of a-Si:H. The electron-hole pairs created during the multiplication phase drift along the applied electric field and are eventually trapped in those localized states. The traps gradually fill up, allowing the charges to drift for longer distances and increasing the conductivity of the amorphous-silicon layer. The leakage current arriving at the intermediate electrode therefore increased slowly over time. This progressively growing leakage current eventually causes a voltage raise on the intermediate electrode with respect to ground, which weakened the anode isolation and increases the residual leakage current. Having an unstable residual leakage current can lead to errors in the gain calibration. Once the illumination source is turned off the trapped charges will slowly get released. The annealing step helps to speed up this process by providing thermal energy.

Hydrogenated amorphous silicon can sustain strong electric fields. Local defects in the layer, such as cracks or bubbles can however lower the breakdown voltage. The maximum bias voltage that could be safely applied to an AMCP can hence differ for each device. For the three measured devices a maximum bias of 500 V was applied, corresponding to an electric field of $5.6 \cdot 10^4$ V/cm for the chips MCP40cc2 and MCP40rc3 and $6.8 \cdot 10^4$ V/cm for MCP34cc2 that had a thinner a-Si:H layer. Although no electrical breakdown was observed for these devices the bias was not further increased as the residual leakage current on the bottom anode was already increasing over time due to the voltage rise on the intermediate electrode.

The incoming flux from the photocathode was measured to be $6.7 \pm 0.05 \cdot 10^{13} \text{ e}^- / \text{s}^{-1} \text{ m}^{-2}$. The gain was then calculated as the ratio of the measured anode current under illumination and the calibrated input current, with the latter being defined as the photocathode current multiplied by the open area ratio of the device. The gain was evaluated as a function of the applied electric field for three different sensor areas on each device. Figures 6.8, 6.9 and 6.10 show the gain measurements for the three samples with aspect ratio 11.5, 11.7 and 13.6, respectively. The graphs on the right show the $\log(\text{Bias})$ versus $\log(\text{Gain})$ relationship. A maximum gain of 104 could be measured for the sample with aspect ratio 13.6 whereas the 11.7 aspect ratio produced a gain of 16 at 500 V bias. The sample with 11.5 aspect ratio that had additionally be coated with a thin layer of alumina resulted in a maximum gain of 54, which demonstrates that the gain can be significantly increased by applying wall coatings. All samples showed the log-linear relationship that was predicted from both the Eberhardt model and simulations done with the FEM model that was described in Chapter 4.

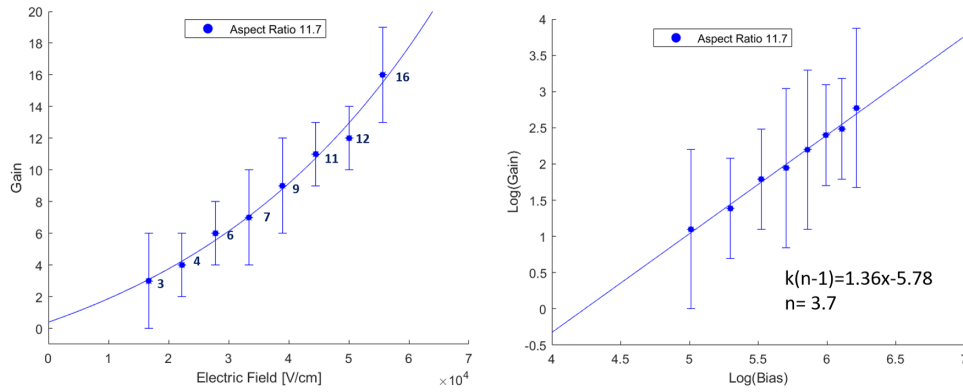


Figure 6.8: Left: Measured gain as a function of the applied electric field for a sensor with aspect ratio 11.7. Right: Same measurement in a Log-Log graph to illustrate the log-linear dependence of the gain and the bias voltage (resp. electric field).

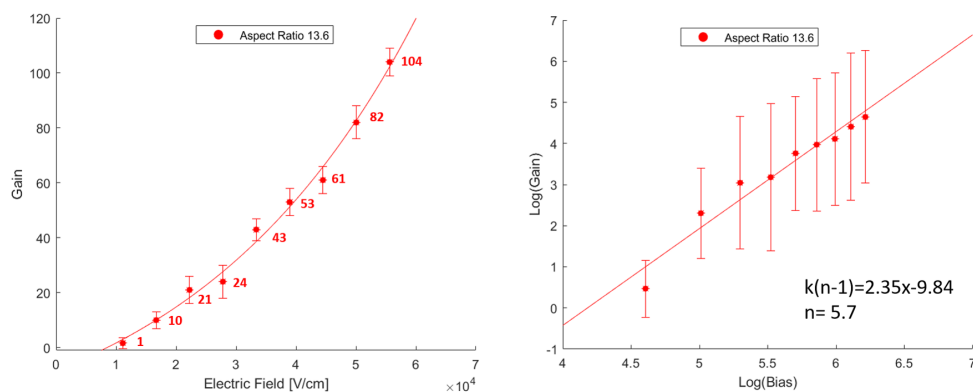


Figure 6.9: Left: Measured gain as a function of the applied electric field for a sensor with aspect ratio 13.6. Right: Same measurement in a Log-Log graph to illustrate the log- linear dependence of the gain and the bias voltage (resp. electric field).

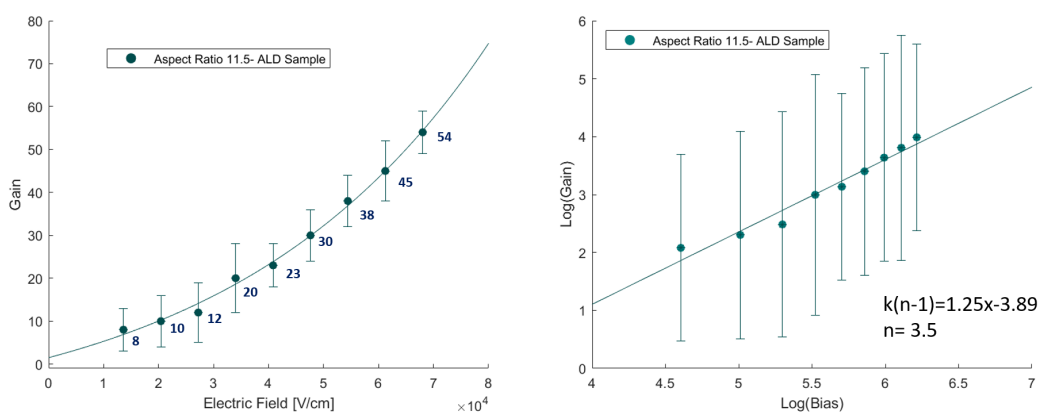


Figure 6.10: Left: Measured gain as a function of the applied electric field for a sensor with aspect ratio 11.5 and a wall coating of alumina. Right: Same measurement in a Log-Log graph to illustrate the log-linear dependence of the gain and the bias voltage (resp. electric field).

The number of dynodes n , representative of the average number of collisions, were then calculated from the slope of the log-linear bias/gain dependence according to equation 2.7 and assuming a value of $k = 0.5$ to describe the curvature of the function $\delta(V)$ as it was proposed by Eberhardt. For the sample with an aspect ratio of 11.7 this resulted in $n = 3.7$ and $n = 5.7$ for the higher aspect ratio of 13.6. For the ALD coated sample with an aspect ratio of 11.5 a value of $n = 3.5$ was found. This seems reasonable since the aspect ratio was almost the same as in the MCP40rc3 sample (11.7) so the number of average collisions should be similar. The overall gain however is higher due to the bigger secondary emission coefficient of alumina in comparison to the amorphous silicon one. The results of the gain measurements from the 3rd AMCP generation are summarized in table 6.3. No gain could be measured in the pulsed regime for all of the samples as the resulting signal was too small to be measured by the oscilloscope.

Table 6.3: Gain measurements generation 3 AMCP

	MCP40cc2	MCP40rc3	MCP34cc2
Aspect Ratio	13.6	11.7	11.5
Maximum Field [V/cm]	$5.6 \cdot 10^4$	$5.6 \cdot 10^4$	$6.8 \cdot 10^4$
Gain Continuous	104	16	54
Collisions n ($k=0.5$)	5.7	3.5	3.7

6.3.4 Electron energy inside the channels

The energy of the electrons between collisions inside a channel is expected to be rather low (<100 eV). The kinetic energy of the released secondary electrons is rarely more than a few electronvolts as it was discussed in the simulation part of this thesis. The following measurement was conducted to get a rough idea of the maximum energy of the produced electrons at the end of the channels. For this a voltage difference was applied between the intermediate and bottom electrode as illustrated in Figure 6.11. The AMCP was then operated under the standard conditions as it was done for the gain measurements described in the previous section. The output current was measured as a function of the potential difference between the intermediate and bottom electrode. Once the potential difference between the two electrodes became larger than the energy of the electrons, they were no longer able to reach the anode.

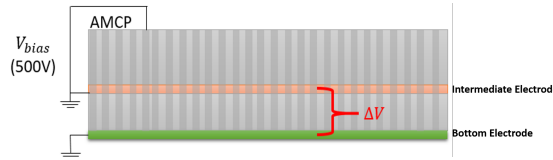


Figure 6.11: Illustration of the measurement setup to estimate the maximum energy of the secondary electrons at the end of the channel.

The measurement was done on an AMCP device of the third generation with an aspect ratio of 13.6. The sample was illuminated with a mercury UV lamp (254 nm). The applied bias on the AMCP was kept at -500 V with respect to the intermediate electrode. From the measurements shown in Figure 6.12 the maximum energy of the electrons at the end of the channel of around 40 eV was determined which is in agreement with values found in simulations.

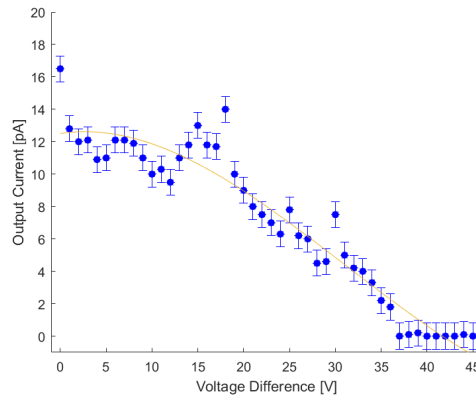


Figure 6.12: Output signal as a function of the applied potential difference between intermediate and bottom electrode. A maximum energy of around 40 eV was found for electrons at the end of the channel.

6.3.5 Gain measurements of the fifth generation of AMCPs

This next section presents the characterization of the AMCP gain of the 5th generation (see Table 5.1 for further explanations of the different generations). The characterization setup had been updated between these and the previous measurements as it was described in Section 6.3.2. The specifications of the tested samples and the measurement conditions are summarized in Table 6.4. Both chips, MCP152C9 and MCP152C3, had been fabricated on the same wafer, with the latter having an additional 5 nm alumina coating. Both chips have aspect ratios around 25. Planacon2C5 is a chip from the series sent to Photonis to be integrated inside a Planacon tube. This device was fabricated to exhibit a lower capacitance. The aspect ratio of 26.2 was similar to that of the other two chips.

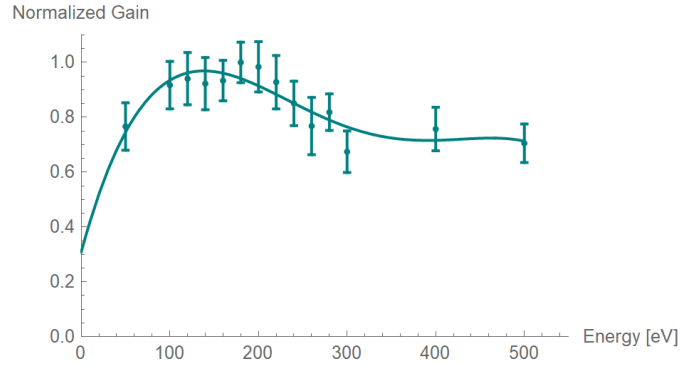
Table 6.4: Properties of characterized AMCPs and measurement conditions

Properties of characterized AMCPs and measurement conditions			
Device	MCP152C9	MCP152C3	Planacon2C5
Generation	5	5	5
Notes	Standard Process	ALD Coated	Low Cap. Structure
Layer Thickness	40 μm	40 μm	42 μm
Hole Diameter	1.6 μm	1.6 μm	1.6 μm
Aspect Ratio	25	25	26.2
Open Area Ratio	4.49 %	4.49 %	3.5 %
Pressure	$5.1 \cdot 10^{-6}$ mbar	$8.2 \cdot 10^{-6}$ mbar	$8.5 \cdot 10^{-6}$ mbar
Bias Photocathode	-700 V	-700 V	-700 V
Flux [$\text{e}^- \text{s}^{-1} \text{cm}^{-2}$]	$2.4 \pm 0.1 \cdot 10^9$	$2.4 \pm 0.1 \cdot 10^9$	$2.4 \pm 0.1 \cdot 10^9$

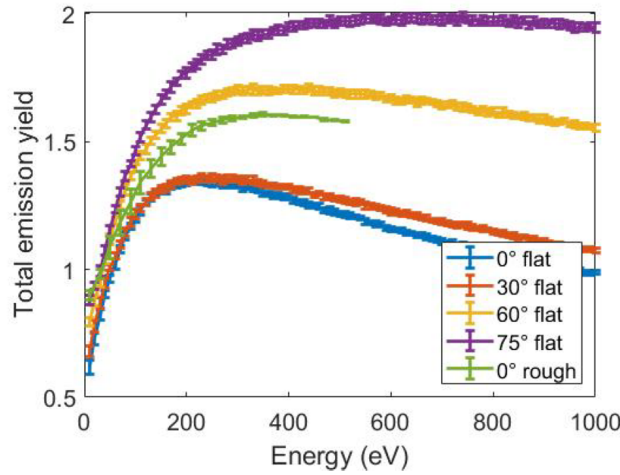
All samples were measured both under continuous illumination as well as with a pulsed laser source.

First impact energy

In a first round of measurements, the potential difference between the photocathode and the AMCP top electrode was varied between -50 to -500 V, and the anode current from the device was measured. By changing this bias, the energy of the incoming particle at the first collision also changes, which can significantly impact the final measured gain. The normalized gain as a function of the energy of the primary electron is shown in Figure 6.13a. From this, a broad maximum could be observed between 120 to 200 eV where the gain was roughly 20 % higher than outside this range. Measurements of the total emission yield of a-Si:H as a function of the energy of the incoming particle have been conducted by [54] and are shown in Figure 6.13b.



(a) Normalized gain as a function of the energy of the primary electron. A broad maximum was found between 120 to 200 eV.



(b) Total emission yield of an a-Si:H layer as a function of energy for different incident angles. (Figure taken from [78]).

Figure 6.13: Measurement of the gain as a function of the incident energy (left). Measured emission yield of a-Si:H as a function of incident energy (right).

By comparing the two graphs, the measured gain resembles mostly the curve of a flat a-Si:H sample with a low incident angle of the electrons. The maximum seems, however, to shift towards lower energies. The most plausible explanation is that the electrons did not collide at the channel's entrance but rather a bit further down. Consequently, their energy at this first collision was higher than the potential difference between the photocathode and the top electrode. Another factor to consider is that the surface morphology of the channel walls is very different from that of the measured flat samples. Although a sample with higher roughness was measured (green curve in Figure 6.13b), this might not necessarily be a good representation of the surface inside a channel. For all the following gain measurements, the bias between AMCP and photocathode was set to 200 V to achieve the highest gain while maintaining a stable flux of electrons from the photocathode. This optimum potential difference may likely differ for samples with wall coatings and for other channel geometries and must be readjusted.

Gain measurements

The gain was then measured again as a function of the applied bias voltage. A typical measurement is shown in Figure 6.14. The measurement procedure was the same as for previous devices. The samples were annealed for 30 minutes at 90 °C before the measurements. A waiting period of around 10 minutes was kept after a change in the bias voltage to ensure stable working conditions. In materials with a large density of localized bandgap states (such as a-Si:H) a certain time is needed to ensure a new equilibrium of trapped carriers after a change in bias voltage [102]. The gain was again calculated as the ratio between the anode current and the calibrated input current. For the measurements in the transient regime, the voltage was measured rather than the current, but the principle stayed the same.

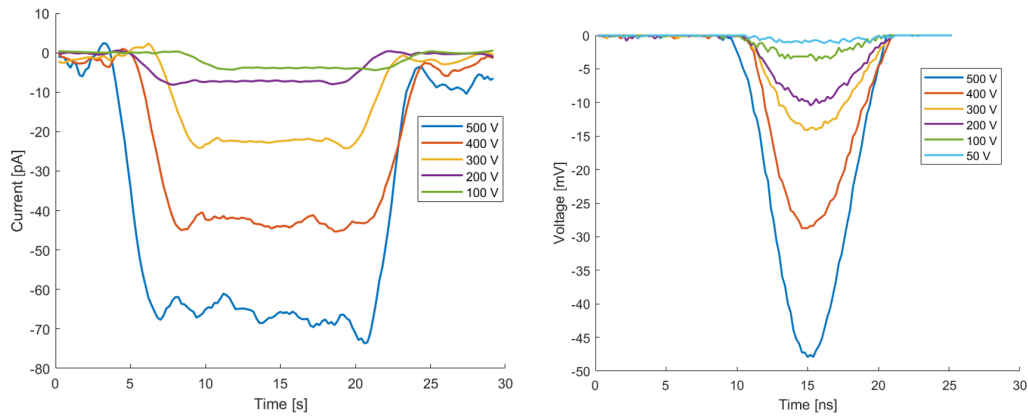


Figure 6.14: AMCP response for different applied bias voltages. Left: Measured output current when the AMCP was illuminated by a mercury lamp for a few seconds. Right: Measured voltage in response to a laser pulse.

The measured gain as a function of the applied bias voltage respective to the electric field for the sample MCP152C9 is shown in Figure 6.15. This sample has an aspect ratio of 25. A maximum gain of around 1500 (1460 ± 54 under continuous illumination and 1494 ± 85 under pulsed illumination) was measured. Four pads were measured in total- two with $500 \mu\text{m}^2$ and two with $250 \mu\text{m}^2$ sensor areas. The largest pads ($1000 \mu\text{m}^2$) were excluded from the measurements- partially because of some localized defects, where a few holes were missing in parts of the area, and because the laser spot did not uniformly illuminate the whole area. No dependence of the gain on the sensor area was observed. Also, no significant difference was observed between the measurements under continuous and pulsed illumination at high bias voltages and strong electric fields. For lower biases, the pulsed gain appeared to decrease more slowly than the gain under continuous illumination.

It is not entirely clear whether this discrepancy was due to a measurement uncertainty or caused by something else. The gain dynamics will be further discussed after all the measurements were presented. The right image in Figure 6.15 shows the log-linear relationship between the bias voltage and the measured gain as predicted by both the Eberhardt model and the Monte-Carlo Simulations presented in Chapter 4.

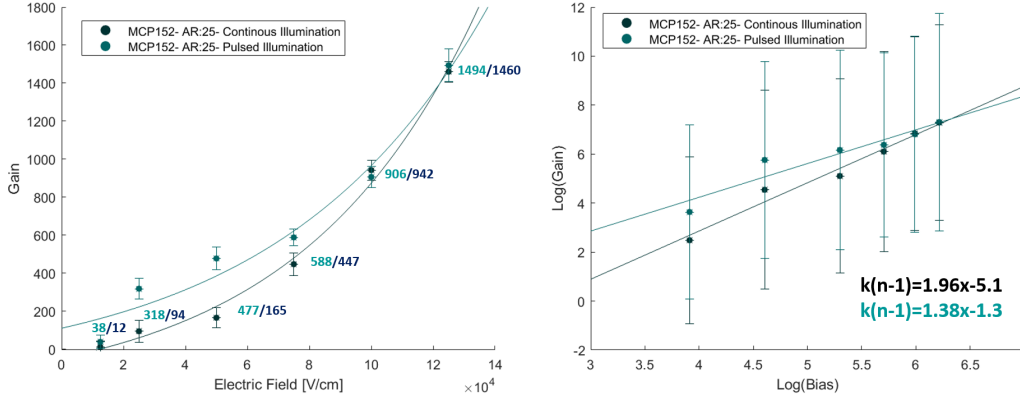


Figure 6.15: Left: Measured gain as a function for the applied bias voltage (respective electric field) of the sample MCP152C9 with an aspect ratio of around 25. The gain was measured as a response to a continuous illumination as well as a pulsed laser source. A maximum gain of around 1500 could be achieved. Right: Log-log plot of the gain- bias behavior. The sample showed the expected log-linear behavior that was also observed for previous devices.

The second chip, Planacon2C5, was measured in the same way. The results are displayed in Figure 6.16. This device has an aspect ratio of 26.2 and was fabricated to exhibit a lower capacitance, as described in Chapter 5. A maximum gain of around 1350 was measured (1361 ± 95 under pulsed illumination and 1325 ± 51 under continuous illumination). The maximum applied electric field was $11.9 \cdot 10^4$ V/cm, slightly lower than for the previous measurement. Two pads were measured, both with a sensor area of $500 \mu\text{m}^2$. For this chip, no significant difference was observed between the transient and the continuous gain for all the applied bias voltages. Again a log-linear relationship was found between the applied bias voltage and the measured gain. Finally, no gain could be measured for the ALD-coated sample MCP152C3. The device showed a positive current under illumination independent of the applied bias voltage. The same effect was observed for another chip coated with 5 nm of alumina. It is reasonable to suspect that the issue is related to the ALD layer. The most probable cause is that the alumina covering the bottom anode could affect the charge collection. An attempt was made to dry etch the alumina on the horizontal surfaces, but the problem remained. Most likely, the ALD layer could not be removed from the bottom pad due to the high aspect ratios of the channels. Further investigation is needed to explain and resolve this issue entirely.

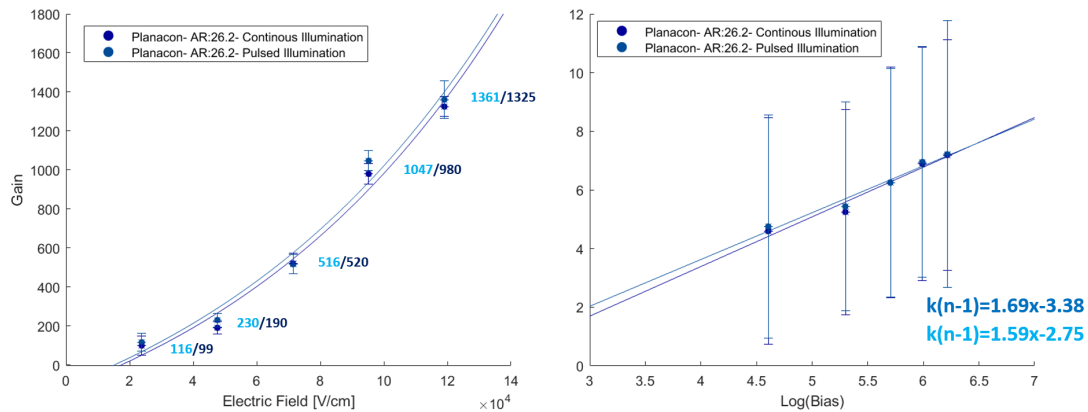


Figure 6.16: Left: Measured gain as a function for the applied bias voltage (respective electric field) of the sample Planacon2C5 with an aspect ratio of around 26.2. The gain was measured as a response to a continuous illumination as well as a pulsed laser source. A maximum gain of around 1350 could be achieved. Right: Log-log plot of the gain- bias behavior. The sample showed the expected log-linear behavior that was also observed for previous devices.

Gain measurement discussion and comparison with simulations

The gain measurements are summarized in Table 6.5. One aspect that needs to be addressed is that the device Planacon2C5 showed a lower maximum gain than MCP152C9 despite having a slightly higher aspect ratio (26.2 rather than 25). There are several possible explanations for this. One difference is the slightly lower applied field. Because the layer of the second device was thicker ($42\text{ }\mu\text{m}$ compared to $40\text{ }\mu\text{m}$ for MCP15C9), the maximum applied bias voltage of 500 V resulted in the lower field strength. Nevertheless, even when extrapolating the gain as a function of the electric field, the expected gain is still lower than the one measured for the sample with aspect ratio.

Table 6.5: Summary of the measured devices from AMCP generation 5

Summary of the measured devices from AMCP generation 5		
Device	MCP152C9	Planacon2C5
Aspect Ratio	25	26.2
Layer Thickness	$40\text{ }\mu\text{m}$	$42\text{ }\mu\text{m}$
Maximum Field	$12.5 \cdot 10^4\text{ V/cm}$	$11.9 \cdot 10^4\text{ V/cm}$
Gain Continuous	1460 ± 54	1325 ± 51
Gain Pulsed	1494 ± 85	1361 ± 95

Another possible reason could be minor differences in the channel geometries of the two samples. The aspect ratio is calculated from the channel length divided by the average channel diameter. Due to the etching process, the channels usually do not have perfectly straight channel wall profiles. The sample MCP152C9 exhibits a more pronounced narrowing towards the end of the channel. Even though the average aspect ratio is lower, the narrower channel diameter towards the bottom could significantly increase the resulting gain. A similar argument can be made about the tilt of the channels. As mentioned in Chapter 5, some devices can have slightly tilted channels of a few degrees due to residual layer stress and the bowing of the wafer. This tilt is, however, very uneven over the wafer; depending on the position of the measured chip on the wafer, this effect can be more or less pronounced. These differences in geometry, although minor, can affect the gain due to the minimal channel diameter. A comparison between channels from chips of the two wafers is shown in Figure 6.17. The images are from test structures from the same wafers as the respective measuring devices, not the same samples (the devices would have to be destroyed to analyze the exact channel geometry).

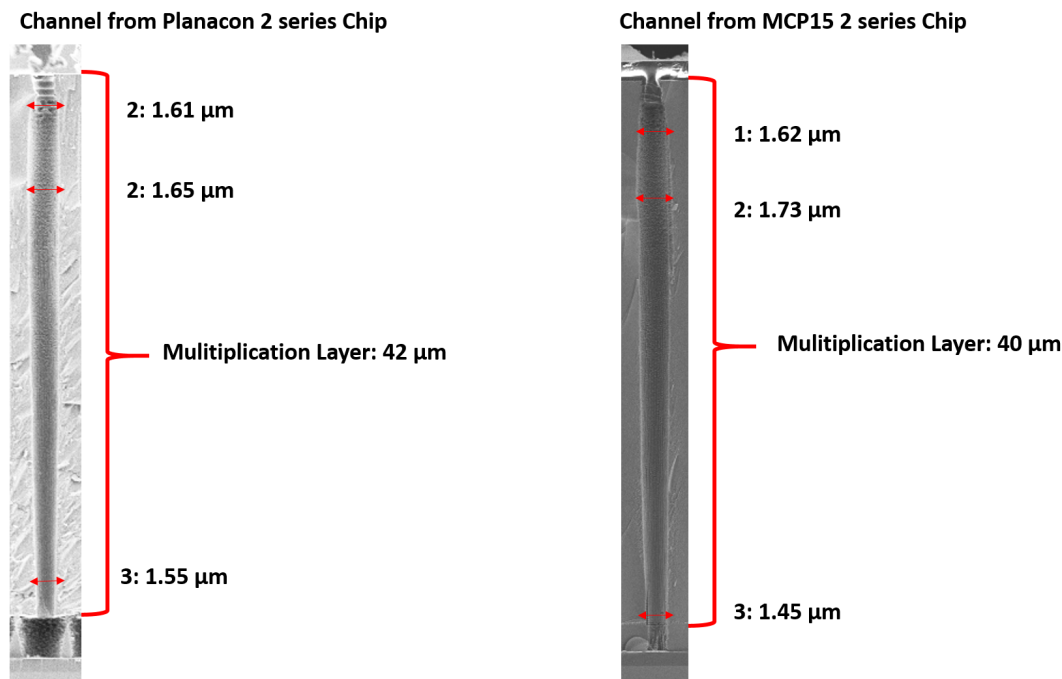


Figure 6.17: Comparison between a channel from the Planacon2 series and one from the MCP152 series. Minor difference in the channel geometry could possibly be responsible for the observed difference in gain. Channels from the MCP152 series (right image) show a slightly more bowing than the channels from the Planacon2 series (left).

The next observation to be addressed is the apparent difference between the transient and continuous gain observed in the measurements of MCP152C9. The behavior was observed for all measured sensors on this chip which minimized the possibility of the difference stemming from measurement uncertainties such as laser instabilities. The discrepancy was, however, not present in the measurement of the chip from the Planacon series. The devices from this fabrication series differ by having a thicker decoupling layer. The opening of the decoupling layer is also slightly larger than the channel diameter to minimize collisions of the electron avalanche in this area. Since this is the main difference between the two chips, the observed phenomenon could be related to the charging effects of this decoupling stack which could modify the electric field in that area. The simulated gain behavior for the given aspect ratios also predicts lower gain values for a weaker field as shown in Figure 6.18. The presence of the decoupling layer and its possible influence on the electric field was also excluded from these simulations, which further supports this hypothesis. However, further investigation is needed to understand the phenomenon entirely.

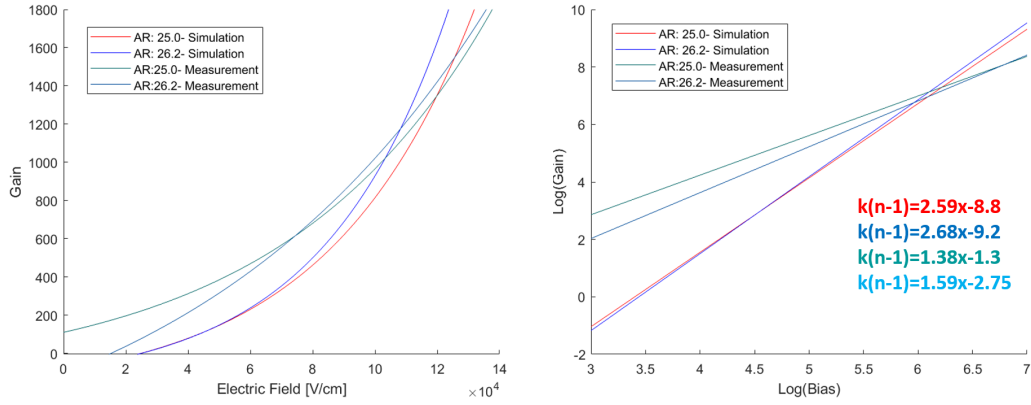


Figure 6.18: Left: Measured gain as a function for the applied bias voltage (respective electric field) of the sample Planacon2C5 with an aspect ratio of around 26.2. The gain was measured as a response to a continuous illumination as well as a pulsed laser source. A maximum gain of around 1350 could be achieved. Right: Log-log plot of the gain- bias behavior. The sample showed the expected log-linear behavior that was also observed for previous devices.

Again the log-linear relationship between gain and applied bias voltage was analyzed for the two measured samples and compared to the simulated value. The simulated curves show a steeper slope than what was measured. Again the number of dynodes or collisions n can be extracted from the slope according to Eberhardt 2.7 as it was done for the measurements of the third generation of AMCPs. However, using the same value of $k = 0.5$ (as a reminder, k is a curvature coefficient relating the secondary emission yield δ to the average voltage difference between two impacts V/n) results in an average number of collisions between 4-5 for the measured data and around 6 for the simulated values, which is too low given the aspect ratio and in comparison to the number of collisions calculated for the generation 3 devices (5.7 for an aspect ratio of 13.6).

The value of k does most probably depend on the electric field strength, so that no single value can be used to analyze all the gain measurements. As the electric fields applied in AMCPs are generally much stronger than those in conventional MCPs, this dependence becomes more critical. Since the value of k can not be readily estimated, using the Eberhardt model for AMCPs is somewhat impractical and underlines the need for more sophisticated simulation tools like the ones presented in Chapter 4.

The last point that should be addressed here is the accuracy of the presented gain measurements. The biggest uncertainty in the gain measurements stems from the calibration of the incoming flux. The estimated quantum efficiency of the used gold photocathode is very low ($\sim 0.0014\%$) and might even be lower when used with a pulsed laser source. The photocathode also appeared to be easily damaged under laser illumination. Another problem arises from the additional photoelectrons produced by the metallic top electrode itself. Although the calibration sample used was fabricated with the same metal and thickness as the AMCP electrode, the calibrated flux might not necessarily be precisely the same due to the different surface morphology of the two layers. The setup should be further upgraded to increase the accuracy of future measurements. A conventional MCP installed between the photocathode and the AMCP would provide a larger incoming flux, reducing the measurement error since the number of photoelectrons produced on the AMCP itself would be significantly smaller than the electron flux stemming from the MCP. Additionally, this would allow us to test the AMCP response as a function of the incoming current. The gain response is expected to be linear up until the point when saturation effects become non-negligible. Further, the gold photocathode should be exchanged or its fabrication process improved to ensure a more stable operation. More efficient photocathodes such as CsI are highly hygroscopic and hence unsuitable for this setup. Other metallic photocathodes, such as Cu or Mg-based ones, could be envisioned.

6.3.6 Gain dynamics

The gain behavior over time was analyzed and compared between the AMCP generations 3 and 5. The output current measured over several minutes for an AMCP of the third generation is shown in Figure 6.19. The graph shows that the output current first spikes to a maximum and then slowly decreases before increasing again. This measurement agrees with previous observations of the gain behavior of AMCPs reported in [19].

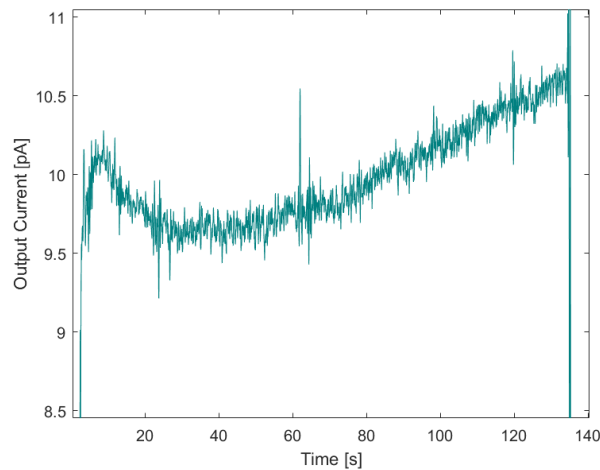


Figure 6.19: AMCP output current measured for several minutes under continuous illumination of the photocathode for an AMCP of the third generation. After an initial spike the gain decreases before slowly increasing again.

The devices of the 5th AMCP generation show a similar initial increase and decrease shown in Figure 6.20. After a few minutes, the current stabilizes and does not exhibit another increase in the output current as the older devices. Once a stable gain has been reached, it could be reproduced when the illumination was switched off and back on again. The gain dynamics can be explained in the following way. The initial spike in gain could be related to a residual water film on the channel walls. The usual residual pressure of around $6 \cdot 10^{-6}$ mbar might not have been low enough to remove all the water molecules inside the channels. During the initial multiplication phase, these molecules can get ionized by the electron avalanche and removed from the channels by the electric field. The time for this initial stabilization phase varies between one and 10 minutes.

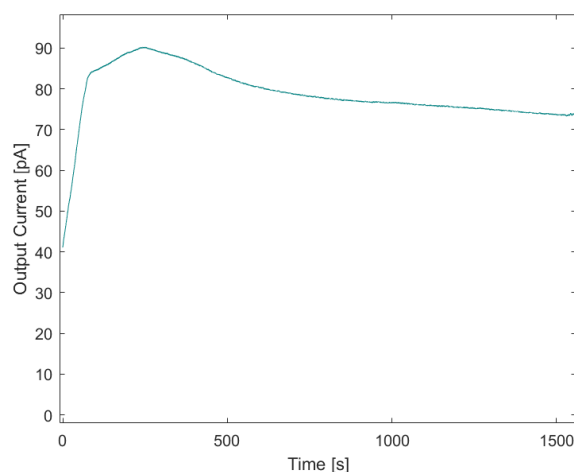


Figure 6.20: AMCP output current measured for several minutes under continuous illumination of the photocathode for an AMCP of the fifth generation. After an initial spike the gain decreases and takes several minutes to reach a stable value.

The increase in current for the older AMCP generations has been investigated in the past and found to be related to a voltage rise on the $\mu\text{c-Si}$ based intermediate electrode. As explained in Chapter 2, the conductivity of the thick amorphous silicon layer can increase under prolonged illumination. This again causes a larger leakage current to be evacuated on the intermediate electrode, which eventually leads to a voltage rise on this electrode. The voltage rise on this electrode also increases the residual leakage current on the anode, which makes the output current grow. Although this effect is expected to saturate at some point, reaching equilibrium conditions might take a long time. The growing leakage current can eventually cause problems reading out the signal, especially for low incoming fluxes. This instability in the output current was one of the main motivations for exchanging the previous $\mu\text{c-Si}$ based intermediate electrode with a chromium based one. Even though the leakage current arriving at the intermediate electrode will still grow under illumination, the chromium electrode is conductive enough to prevent a significant rise in voltage on the electrode, keeping the residual leakage current stable over time. In the future, these gain stabilization studies should be extended to include various input fluxes and gain values of the AMCPs.

6.3.7 Characterization of funnel-shaped AMCPs

A first set of funnel-shaped devices have been fabricated. They had a channel length of 40 μm and funnel opening of 4 μm . The depth of the funnel was about 6 μm . A cross-section image of the funnel channel can be seen in Chapter 5 Figure 5.22. A first characterization was done on one of the samples. The specificities and measurement conditions of this sample are given in Table 6.6.

Table 6.6: Properties of funnel AMCP

Device:	Funnel AMCP- FAMCPOE1
Channel length:	40 μm
Funnel diameter:	4 μm
Funnel depth:	~6 μm
Channel diameter (lower part):	1.7 μm
Top Electrode :	Al- Evap.
Open Area Ratio:	~95%
Pixel Size:	1500 μm^2
Design :	Planacon2
Funnel Coating :	MgO (10 nm)
Pressure:	$5 \cdot 10^{-5}$ mbar
Max. Bias:	350 V
Gain (350 V):	451 ± 15

Two pixels with an area of 1500 μm^2 each were measured under pulsed illumination. A few adjustments had to be made for these measurements. Firstly, as the flux from the photocathode seemed to have further decreased, the gold photocathode was removed, and the top electrode of the chip served as a photocathode. This means that the energy of the first impact could not be optimized, and that the measured gain was most likely lower than the maximum achievable gain. Secondly, the absence of the additional photocathode makes the calibration of the incoming flux more complicated. To calibrate the incoming signal, the laser beam was focused on one pixel, and the resulting voltage on the top electrode was measured when there was no bias applied and used as the incoming reference. Figure 6.21 shows the measured gain for one of the fabricated funnel AMCP. A gain of 451 ± 15 was measured for an applied bias of 350 V (corresponding to an electric field of $8.75 \cdot 10^4 \text{ V/cm}$). The bias voltage could not be further increased for this device because of an electrical breakdown. The expected gain for an applied bias of 500 V could, however, be extrapolated from the fitted exponential function- for this, a value of 1578 was found. This is lower than the 1912 that was simulated for this channel geometry. However, in the simulation model, the energy of the first impact was assumed to be 200 eV. Due to the missing gold photocathode, the first impact energy in this measurement was significantly lower, which explains the decrease in gain. Additionally, the simulation parameter used for a MgO layer might not be perfectly accurate since secondary emission yield can strongly depend on the deposition parameter of a given layer.

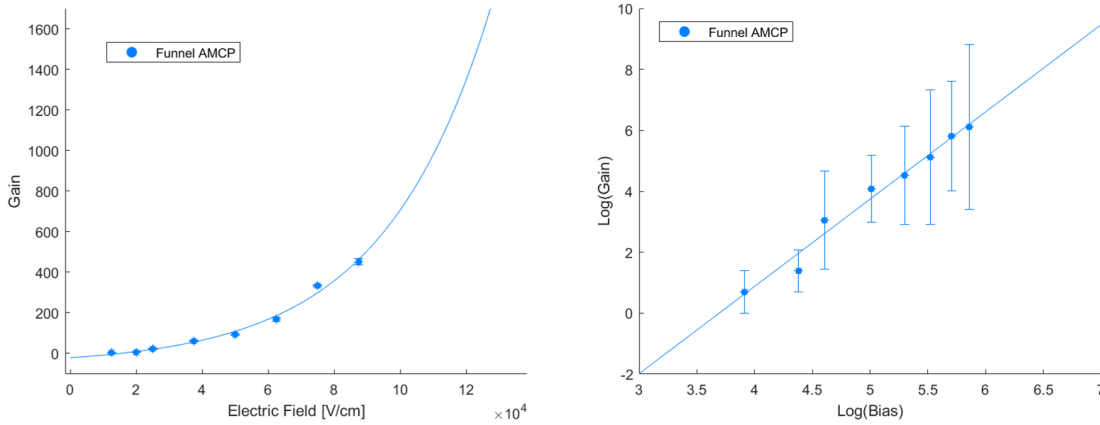


Figure 6.21: Left: Measured gain as a function for the applied bias voltage (respective electric field) for a funnel AMCP. The gain was measured as a response to a pulsed laser source. A gain of around 451 was measured for an applied bias of -350 V (an electric field of $8.75 \cdot 10^4 \text{ V/cm}$).

Right: Log-log plot of the gain-bias behavior. The sample showed the expected log-linear behavior observed for previous devices without funnels.

There are a few observations that need to be addressed. First, the chip could only be biased with -350 V before electrical breakdown occurred. The resistance between the top electrode and ground was measured beforehand. It yielded $\sim 30 \text{ M}\Omega$, which is in the same range as previously measured samples ($35 \text{ M}\Omega$ for the MCP152 series chips) that could sustain a bias voltage of -500 V. The problem of electrical breakdown can either be related to the different chip design- the funnel samples used the same design as the Planacon2 series chips where similar issues also occurred at some point- or it could be linked to the metallization process of the top electrode. Especially for the samples where the electrode was evaporated onto the funnels, the metal might not evenly cover the entire area. This could also enhance the chances of an electrical breakdown due to an uneven voltage distribution. Alternatively, the metal might also have entered too deeply into the channels. Another thing noted during the measurement was that the leakage current flowing through the a-Si:H stack took an unusually long time to stabilize after the voltage was changed. Usually, this current stabilizes after a few minutes following a voltage change. For the funnel sample, this time increased to up to an hour for a voltage step of 50 V until equilibrium conditions were reached. The reason for this is not fully clear yet but could be related to the larger channel surface area due to the funnel openings or shunting paths inside the channels. The characterization setup should also be upgraded to include a glass MCP and a new photocathode, ensuring a more accurate calibration of the incoming current and, consequently, of the AMCP gain. This setup would also allow investigating the exact detection efficiency of the sensors. All the mentioned points need to be addressed and further investigated in the next batch of funnel-shaped AMCPs. Nevertheless, despite these issues, the first working funnel-shaped AMCP could be successfully fabricated and characterized and can serve as a reference for further optimization steps.

6.4 Electron Beam Induced Current Measurements

An additional setup based on the electron beam induced current (EBIC) technique was used to check the AMCP sensors qualitatively. The EBIC technique is conventionally used to investigate semiconductor devices. The electron beam of a microscope generates charge carriers that are then collected by an electric field within the material. The resulting current is then connected to the SEM video board. In this way, areal inhomogeneities in the electrical properties of the material can be revealed [103]. In our case, the technique was used to check if the electron multiplication was homogeneous over the sensor area and to localize potential defects in the layer.

6.4.1 Setup description

For the characterization of the AMCP with an electron beam, the sample was placed inside the SEM chamber (Zeiss Merlin). The anode of the detector was connected back to the SEM video board over a current-to-voltage amplifier. When the SEM beam was swept over the detector, the produced current arriving at the bottom electrode was visualized on the video board as a function of beam position. This provided a qualitative overview of the electrically active areas of the device and allowed for a fast and visual inspection. To have multiplication inside the channels, the sample was biased during the measurement with a high-voltage supply (Stanford Research Systems PS310). The measurement setup is shown in Figure 6.22.

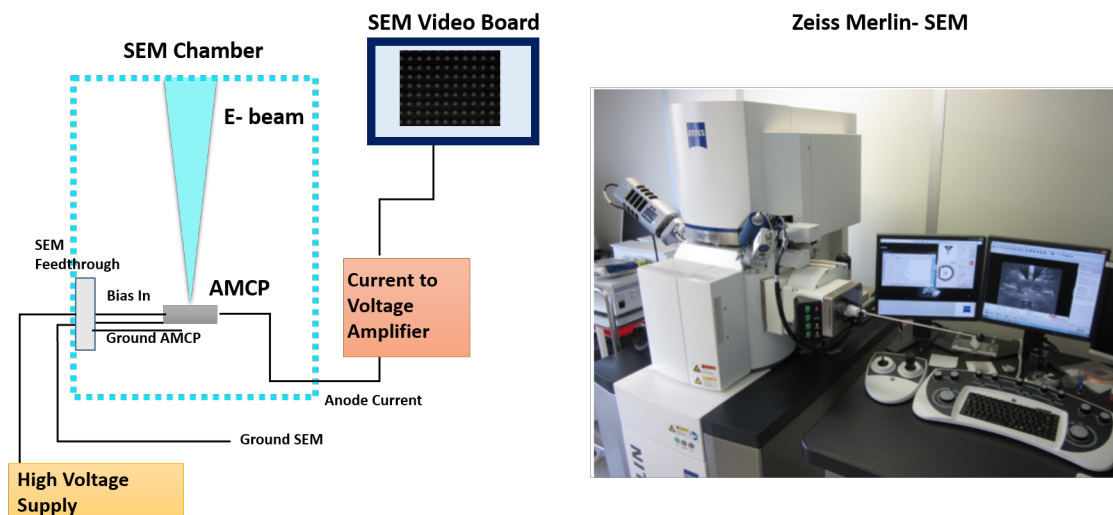


Figure 6.22: EBIC Setup: The current arriving at the anode was fed into the video board of the SEM over a current-to-voltage amplifier when an electron beam was swept over the AMCP. A high voltage supply was used to bias the AMCP up to 300 V inside the SEM chamber.

6.4.2 Measurements on third generation AMCPs

EBIC maps were acquired using an AMCP of the 3rd generation. The used device, MCP40CC2, had an aspect ratio of 13.6 and a measured gain of 104 for an applied bias of 500 V. To record an EBIC image, the beam was swept over the sample at a slow scan speed to reduce the noise in the image, and each EBIC image represents a single scan. The beam energy was set to 1 kV, and a beam current of 280 pA was used. The device was tilted by 5° during the measurement to ensure the incoming electrons collide with the channel walls. First, the influence of the bias voltage applied to the AMCP on the EBIC image was investigated. The left image in Figure 6.23 shows the EBIC map when no bias was applied to the device. The end of the channels can be vaguely identified from electrons passing directly through them, but the resulting signal is low since no multiplication is taking place inside the channels. Afterward, a bias of -200 V was applied. The channels then showed a bright signal in sharp contrast to the surrounding area, shown in the right image of Figure 6.22. All channels in the irradiated area could be clearly identified, which proved that electrons were multiplied in the channels and that the bias voltage was evenly spread across the investigated AMCP surface.

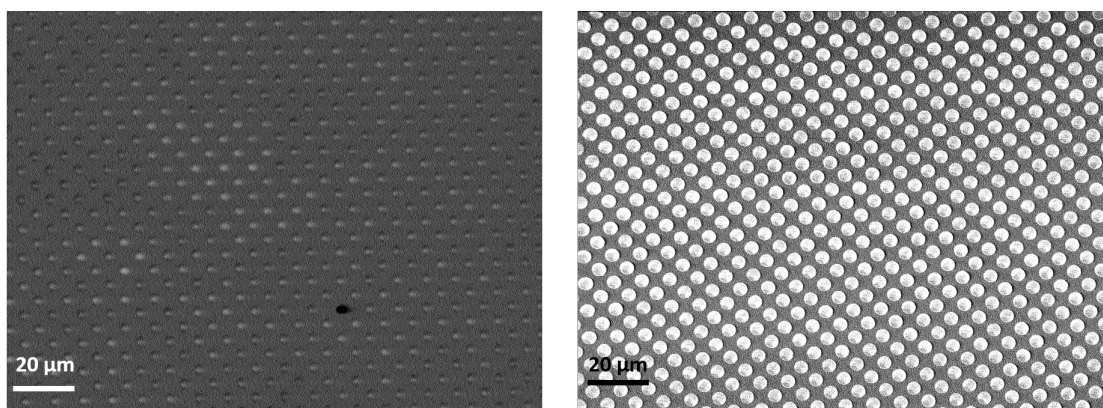


Figure 6.23: Acquired EBIC maps showing the difference between the non-biased (left) and biased device (right). Once a bias was applied the channels showed a much brighter signal than the surrounding area, demonstrating that a multiplication process was taking place. The measurement was done with 280 pA beam current and 1 kV electron energy.

In a subsequent test, shown in Figure 6.24 the influence of the tilt angle between the electron beam and the sample on the produced current was investigated. In the first case, no tilt was applied, resulting in a brighter signal only from a small annular area around each channel. In the second case, with an 8° tilt, the signal comes from the whole channel area. This suggests that if no tilt was applied, a portion of the electrons was travelling through the channels without actually colliding with the channel walls. Conventional glass-based MCPs have channel bias angles between 8- 20°. Since the AMCPs do not have a bias angle, their axis is perpendicular to the sample surface. A tilt with respect to the incoming electron beam thus increases the detection efficiency. Galanti and Renaud found maximum efficiency at a 13° tilt [57].

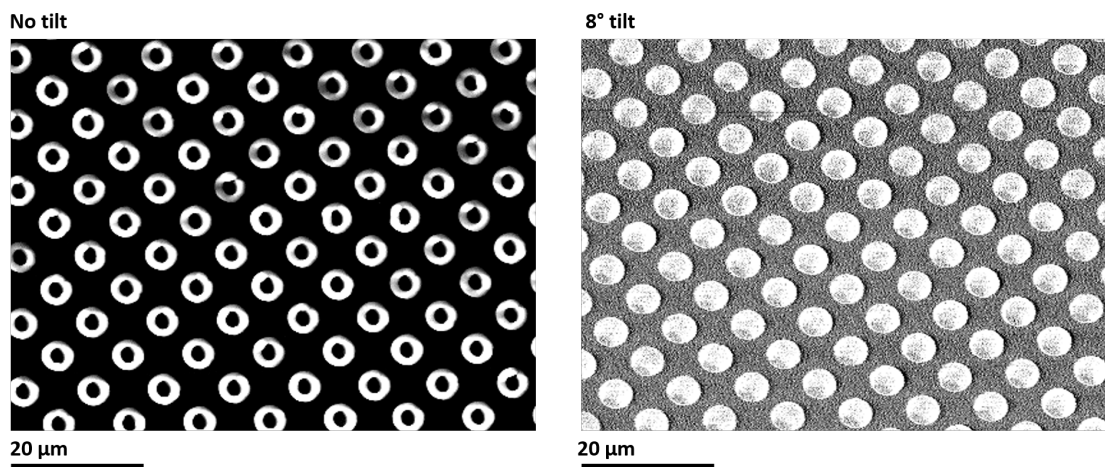


Figure 6.24: Acquired EBIC maps showing the difference between normal incidence of the electron beam (left) and a 8° tilt between beam and device (right).

In a final measurement, shown in Figure 6.25, with the generation 3 devices, the beam was focused on a smaller area (higher magnification of the image). With the scan speed staying the same but the pixel being smaller, the total current entering one channel was significantly larger. During the first scan, the area showed the usual bright channels observed in previous images (the sample was still biased with -200 V and tilted by 8°). When the same area was scanned again, the contrast between the channel and the surrounding area was drastically reduced, indicating that the signal inside the channels decreased. After fifteen minutes, the same area was mapped again (the magnification of the image was decreased again to include channels that had not yet been scanned), and the darkened area could still be identified. This observation indicated that the decrease in signal at high input current is related to localized charging effects, most likely of the decoupling layer between the grounded intermediate electrode and the anode. Since both these electrodes are at ground potential, the charges in this layer are not (or only very slowly) replenished. During a multiplication event, the surface of the decoupling layer gets increasingly depleted of electrons and hence attains a positive charge. This positive charge then modifies the electric field at the bottom of the channel, affecting electron multiplication. Saturation due to insufficient charge replenishment can be excluded as an explanation because the effect was still visible after a recovery time of fifteen minutes.

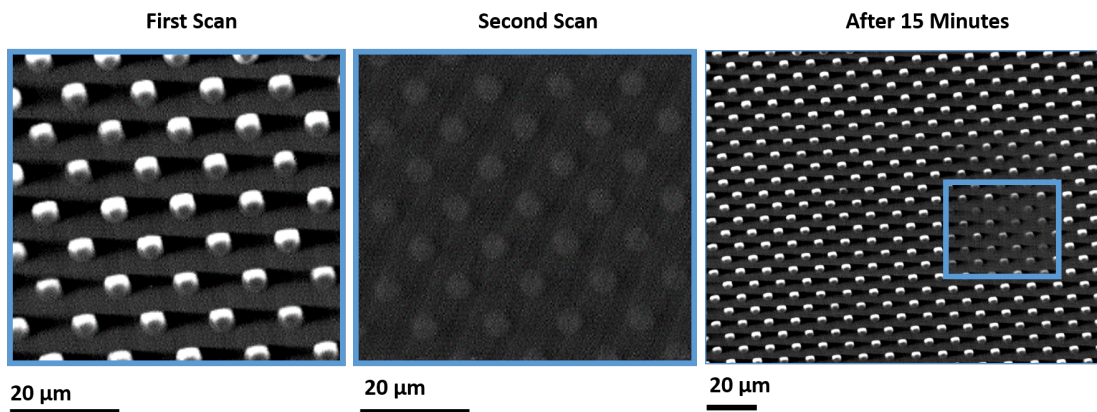


Figure 6.25: Charging effects locally decrease the induced current over time. After the observed decrease, the beam was focused on a different spot on the AMCP. Fifteen minutes later, the first area still appear dark.

6.4.3 Measurements on forth generation AMCPs

EBIC measurements were again carried out on the 4th generation of AMCPs. These devices had a chromium top electrode and higher aspect ratios between 18- 22. However, no gain could be measured for these samples due to their high leakage current. An EBIC map from these samples, shown in Figure 6.26, displayed a low contrast between the signal from the channel and the surrounding area at a bias of -100 V. This means that a current flows through the decoupling layer towards the anode of similar amplitude to the generated current inside the channels. This observation is in agreement with the high leakage current observed during the gain measurement. No structural defects in the layer were visible during the EBIC mapping, and the leakage current appeared to be homogeneous over the analyzed area. Hence, the problem is most likely caused by an insufficient current evacuation at the intermediate electrode. The electrode might be too thin or not conductive enough.

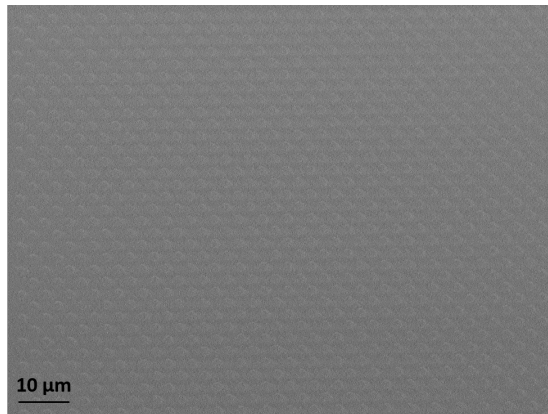


Figure 6.26: Acquired EBIC maps showing a low contrast between channels and the surrounding area. The high leakage current on the anodes is most likely due to an insufficient current evacuation at the intermediate electrode.

6.5 Summary and conclusion

In this chapter, the characterization of the fabricated devices was presented. First, the gain was measured on generation 3 devices fabricated in 2014 but not yet characterized. For these samples, a maximum gain of 104 ± 5 was measured for channels with an aspect ratio of 13.6 and an applied electric field of $5.6 \cdot 10^4$ V/cm. The samples were only measured under continuous illumination (254 nm mercury lamp) as the response to a pulsed laser (266 nm) was too low to be measured. After these measurements, the characterization setup was updated in preparation for the transient measurements. Two chips from the newest generation of AMCPs were then characterized. One was fabricated using the standard procedure, while the other was designed to have lower capacitance and widened decoupling layer. As expected a higher gain was measured with the increased aspect ratio. A maximum gain of 1494 ± 85 was measured for the chip with the standard design, an aspect ratio of 25, and an applied electric field of $12.5 \cdot 10^4$ V/cm. The second chip resulted in a slightly lower maximum gain of 1361 ± 95 despite having a higher aspect ratio of 26.2. This difference can be related to minor differences in the exact channel morphology, as the narrow channels are usually not perfectly straight. A slight narrowing of the channels towards the bottom of the first chip could be sufficient to result in a higher gain despite the lower average aspect ratio. The gain dynamic over time was compared between the two generations. It showed a more stable behavior for the newer samples due to the metallic intermediate electrode being more conductive than the previous μ c-Si one. The first funnel-shaped AMCP was characterized, and a gain of 451 ± 15 could be measured for an applied electric field of $8.75 \cdot 10^4$ V/cm. Several issues were identified during the measurement, such as electrical breakthrough at high bias voltages and long stabilization time of the leakage current, and need to be addressed in the next series of funnel AMCP. Finally, the sensor functionality was analyzed qualitatively with the EBIC technique. This showed the importance of the angle of the incoming beam on the gain. Charging effects with high incoming fluxes were also observed. Now that the gain of AMCPs has reached a value sufficient for real applications, their other properties will have to be further examined. For this purpose, as already mentioned above, it would be helpful to equip the characterization setup with a conventional MCP for testing the AMCP response under much higher incoming fluxes. This would allow for testing the linearity of the detector response and the eventual onset of saturation effects. Having a higher input current for the characterization would also reduce the calibration errors of the incoming flux and allow to quantify the detection efficiency accurately. The latest AMCP devices have not yet been analyzed with the EBIC technique. This measurement would provide information about the influence of the improved intermediate electrode on the charging effects observed earlier. A final parameter that has not yet been discussed for AMCPs is their dark noise count. A low dark count is crucial for applications with low incoming fluxes. A typical dark count rate for MCPs is in the order of 0.2- 1 counts/cm²s. The dark count rate in AMCPs is expected to be low but could be affected by sharp edges inside the channels that could, combined with the strong electric field, lead to a localized increase of dark counts.

7 AMCP Integration

The following chapter presents the first steps toward the final integrated detector. As introduced in Chapter 3, the complete TOF-PET detector will consist of an AMCP grown on top of the readout electronics and sealed inside a vacuum tube. The first section in this chapter focuses on the AMCP integration within a vacuum tube (Planacon). The integration was done step-wise to ensure that the final detector would be successful. In the second part of the chapter, the AMCP was tested together with an electronic readout to have a first assessment of the timing characteristics of the detector.

7.1 Planacon integration

One of the main limitations in detecting Cherenkov radiation is the low quantum efficiency of most photocathode materials. For the final envisioned PET scanner prototype to be successful, this quantum efficiency needs to be as high as possible. For this purpose, the sensors are planned to be integrated with a commercially available vacuum tube called Planacon, provided by Photonis, that will be sealed with a highly efficient photocathode. A sketch of the Planacon structure is shown in Figure 7.1. In a first integration step, three AMCP chips were placed inside individual Planacons. At this stage, the readout electronics were still located outside the Planacons. The primary purpose of this first integration step was to ensure the compatibility of the AMCP devices with the assembly procedure and to provide the first proof of concept for detecting Cherenkov radiation, even though timing properties and active area were not yet optimized. In the final integration, the AMCP chip and the integrated electronic readout will be placed inside the tube. The following section describes the steps taken to realize the first integration.

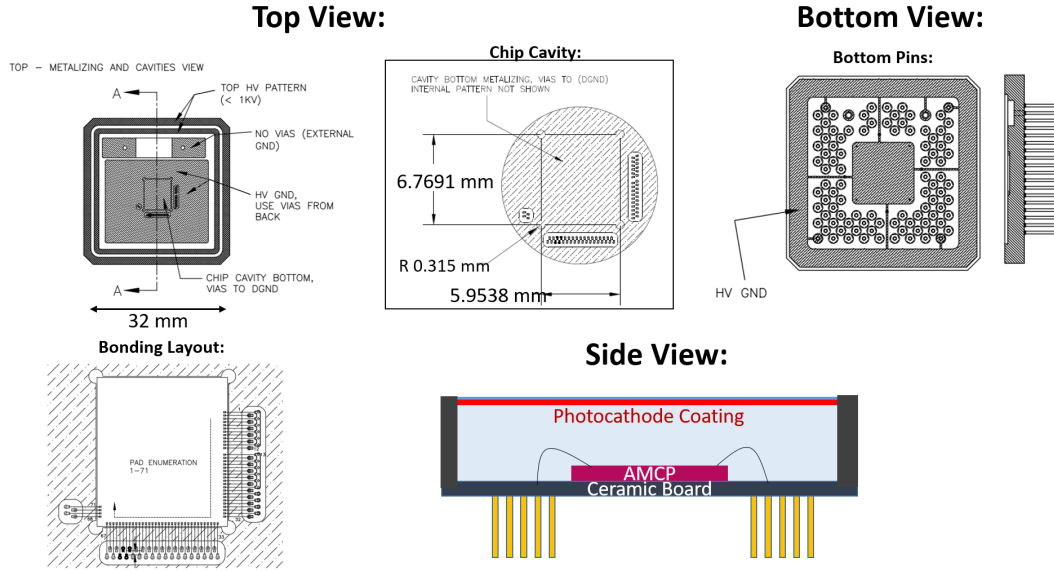


Figure 7.1: Planacon structure, showing the top view of the ceramic PCB with the cavity where the AMCP is placed, the bonding pads, the bottom view with the pins connecting to the bonding areas inside, and the side view of the whole tube.

7.1.1 AMCP chip design

The design of the AMCP test structure had to be adapted for the Planacon tube integration. Firstly, the chip size and the wire bonding pad locations had to match those of the available ceramic PCB hosting the AMCP and providing the electrical connections outside of the Planacon. Additionally, as no electron screen can be placed inside the tube, the transmission wires had to be shielded on the chip itself as much as possible, and wire bonding pads were kept small to minimize the effect of stray electrons reaching them. The devices were fabricated according to the steps described in Chapter 5, to keep the capacitance as small as possible. Two different designs were implemented- one with four bigger individual sensor areas of $1500 \mu\text{m}^2$ each and one with 12 individual sensors with an area of $500 \mu\text{m}^2$ each. The idea behind this choice was to compare the influence of the bigger capacitance on the timing properties of the architecture. Both designs are shown in Figure 7.2 and further explained there. The channels were placed $4 \mu\text{m}$ away from each other in a hexagonal pattern, just as in the standard design, and the final aspect ratio was 26.2. The specifications of the chips are given in Table 7.1. Characterization of these chips was presented in Chapter 6.2.5. It should be noted that although chips from the same wafer were tested beforehand, the chips used in the assembly were only visually inspected, as testing would have damaged the small wire bonding pads.

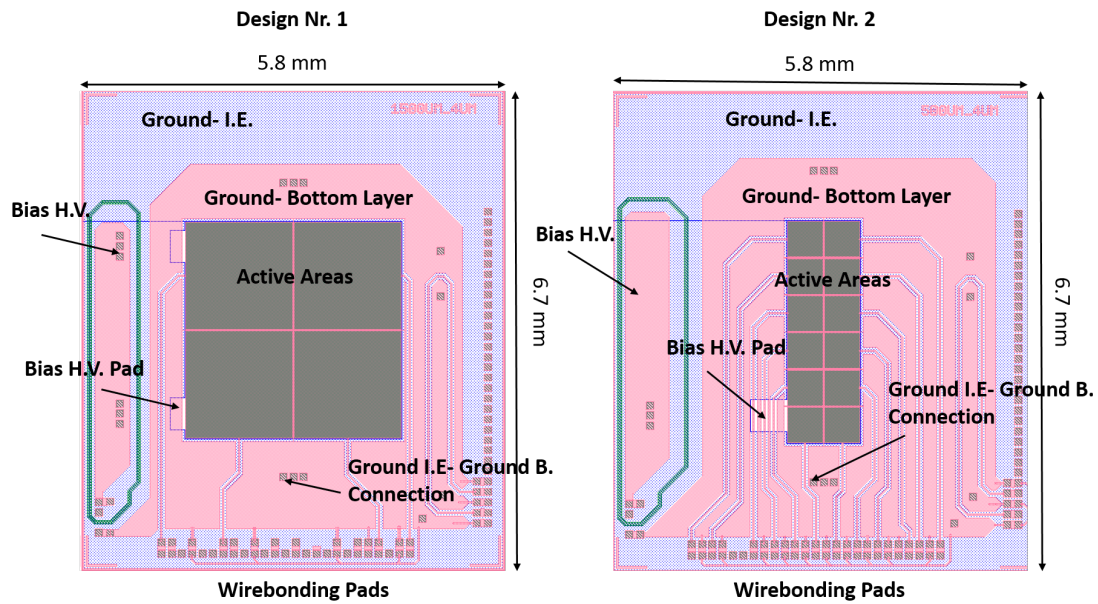


Figure 7.2: Designs of the AMCP chips for Planacon integration. The area in pink represents the lowest layer, showing the grounded area surrounding the pads and transmission wires. The grounded area of the intermediate electrode covers most of the visible chip area. The two grounds (mid. ground and bottom ground) are connected by small openings in the metal where a wirebond is later placed. Wirebonding pads are kept small and are placed on the lower part of the chip. The active area is shown in dark green in the middle of the chips. The first design has four individual sensors with an area of $1500 \mu\text{m}^2$ each and the second design has 12 individual sensors with an area of $500 \mu\text{m}^2$ each.

Table 7.1: Specifics off the integrated chips.

Properties of characterized AMCPs and measurement conditions			
Device	Planacon2LB3	Planacon2LS3	Planacon2LS5
Aspect Ratio	26.2	26.2	26.2
Pad size	$1500 \mu\text{m}^2$	$500 \mu\text{m}^2$	$500 \mu\text{m}^2$
Capacitance	95 pF	19.8 pF	19.8 pF
Active Area	3.5 %	3.5 %	3.5 %
Gain (500 V)	1350	1350	1350

An additional back metallization had to be performed on the chips so they could later be attached to the ceramic PCB of the Planacon by an eutectic die bonding. This attachment was necessary to ensure compatibility with the high vacuum inside the Planacon tube. In this process, two metallic areas are rigidly bonded together by heating the metals above the melting temperature of the eutectic bond. For this purpose a 500 nm thick gold layer was sputtered on the back surface of the chips. A thin (5 nm) layer of chromium was used as an adhesion layer for the gold. The standard die attach process performed by "Photonis" was set at 350 °C. Because of the possibility of hydrogen diffusion out of the amorphous silicon layer, the process temperature was lowered to 300 °C after confirming that good adhesion could still be achieved at this lower temperature. Figure 7.3 shows an AMCP die attached to a Planacon structure and with the added wire bonds.

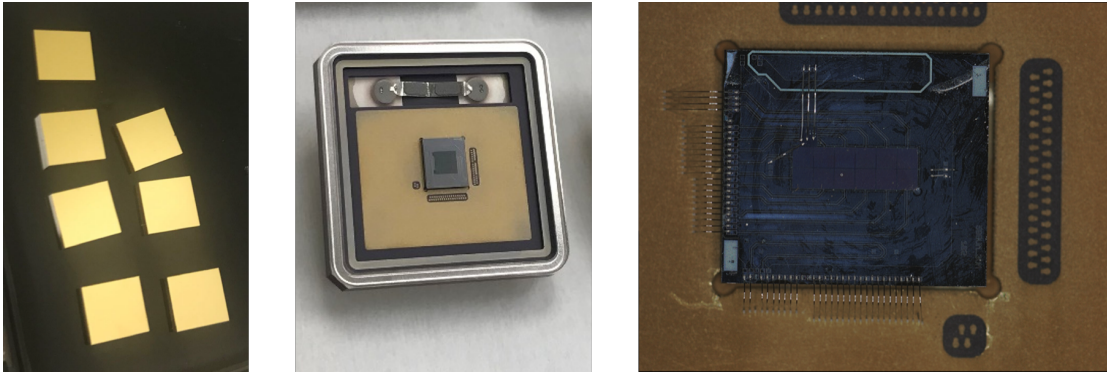


Figure 7.3: Chips with a gold back metallization (left). AMCP bonded to a Planacon board by eutectic die attach (middle). AMCP chip with the added wire bonds (right).

As mentioned before, having a highly efficient photocathode is crucial for detecting Cherenkov radiation. Besides that, other factors such as the dark count rate and response time are essential for the overall detector performance. The dark count of the final detector architecture is expected to be dominated by thermionic emission from the photocathode. Since these counts can not be separated from actual events, this value should be as low as possible. The time response of the photocathode influences the timing properties of the detector, as the traveling time of a photoelectron inside the photocathode can limit the time resolution of the device [104].

The photocathodes developed by "Photonis" have been optimized to have high efficiencies close to or above 30 % for a tuneable spectral range and a low dark count rate down to ~ 30 Hz/cm², making them ideal for applications where a low number of photons need to be detected. The photocathode was grown on a sapphire substrate, extending the spectral sensitivity range down to 150 nm [105]. The quantum efficiency of the implemented photocathode is shown in Figure 7.4.

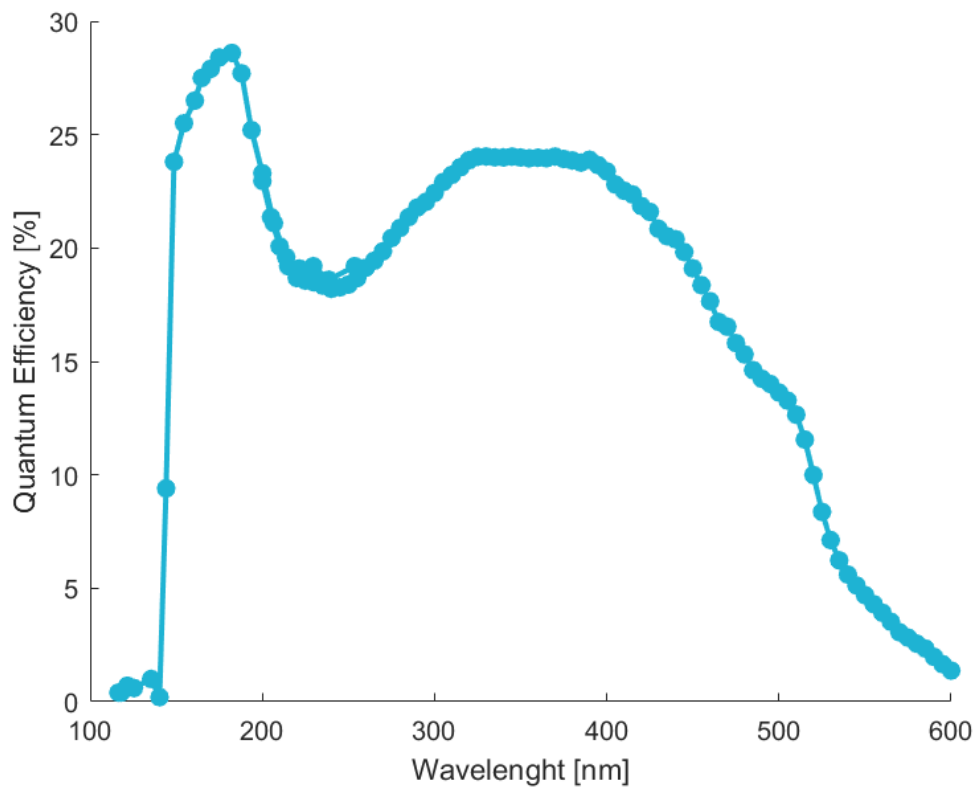


Figure 7.4: Quantum efficiency of the provided photocathode as a function of wavelength (measurement data provided by Photonis).

A connection was provided to apply a bias on the photocathode. Figure 7.5 shows the final assembled chips inside the Planacon tubes. At the time of this thesis three AMCP chips have been assembled into Planacon tubes. Their functionality will be tested in the near future to ensure the compatibility of the chips with the assembly process. A first measurement of the coincidence time resolution with a gamma source and a scintillator will be carried out as well.



Figure 7.5: AMCP chips integrated into a Planacon tube, front (left) and backside (right).

7.2 Electronic integration and timing properties

The second part of this chapter presents the first integrated tests of the AMCP with the readout electronics. AMCP chips were connected to an amplifier, and their response to a fast laser source was observed. This arrangement allowed to characterize the timing characteristics of the AMCP/amplifier configuration separately from the Planacon configuration, where the photocathode and its distance to the chip might influence the time resolution of the complete architecture. As mentioned in Chapter 3, an excellent coincidence time resolution down to 10 ps is needed to increase the SNR of TOF-PET scanners. MCPs are known for their fast timing properties below 100 ps, depending on pore size, bias angle, the applied voltage over the MCP and the used readout. This section first discusses the theoretical aspect governing the time resolution in MCPs and AMCPs, respectively, and then presents the first measurements of the AMCP time resolution.

7.2.1 Theoretical aspects

Two main components govern the time resolution in MCPs: The avalanche process itself causes an intrinsic spread in the arrival times, and an additional time jitter stems from the way the signal is collected and read out at the anode. The avalanche formation in a channel suffers from fluctuations in response to an incoming particle. The leading cause is given by the arrival position of the primary particle inside the channel. The principle is illustrated in Figure 7.6. Two photoelectrons arrive at the channel entrance at the height of z_1 at the same time; one of them collides right at the top, causing the release of secondary electrons. These secondary electrons are released with energies of a few electronvolts and accelerated towards position z_2 by the potential difference $V_{z1} - V_{z2}$ between the two positions. The second photoelectron collides at position z_2 directly, starting with an energy of E_{In} at z_1 . The second photoelectron will reach the height z_2 faster than the first one, causing a difference in the arrival time of a few picoseconds. The larger the area of the potential first hit, the bigger this time difference becomes. Hence, it can be reduced by decreasing the pore diameter and increasing the bias angle in the case of straight channels. For channels with a funnel-shaped opening most of the incoming electrons collide inside the funneled area. In this case the time resolution will then be mostly determined by the depth and width of the funnel opening and the bias angle of the straight part of the channel becomes less important. Other time differences are caused by the statistical nature of the secondary electron yield and release angles.

The larger the number of produced secondary electrons, the more these fluctuations will average out. Having a high yield at the first impact, by optimizing the energy of the first impact and using a high secondary emissive coating, help to further reduce this jitter component.

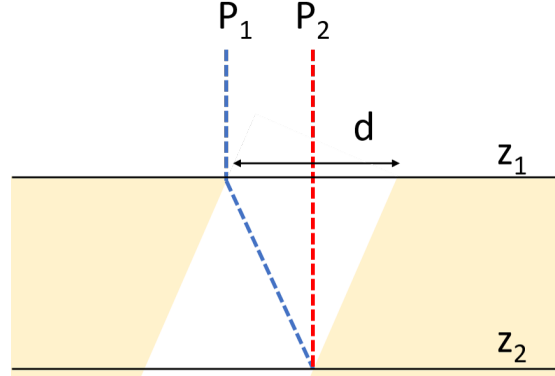


Figure 7.6: Jitter component caused by the position of the first impact. Two incoming particles P_1 and P_2 reach a height z_2 at two different times because of the difference in trajectories and velocities.

Ideally, the resulting current leaving the pores would then be recorded without adding any additional timing uncertainties. In reality the maximum achievable time resolution depends on the shape of the signal and the noise present, both of which are also affected by any parallel capacitances and signal attenuation as the electric pulse travels through the transmission lines. There are various methods to measure the arrival time of fast electrical pulses. Typically the time at which a pulse crosses a certain threshold is recorded. The jitter Δt of a signal at a given threshold can then be described by [106]:

$$\Delta t = \frac{\sigma_N}{\left. \frac{dA}{dt} \right|_t} \approx \frac{\sigma_N}{A_{Max}} \tau_{rise}, \quad (7.1)$$

where A stands for the signals amplitude, σ_N is the standard deviation of the noise and τ_{rise} is the rise time. Figure 7.7 illustrates how noise and rise time influence the uncertainty of the threshold crossing time. The overall measured time resolution is always lowest for single photoelectron detection due to the statistical variance of the avalanche process. For a large number of incoming photoelectrons the variances will average out and the time resolution increases [107].

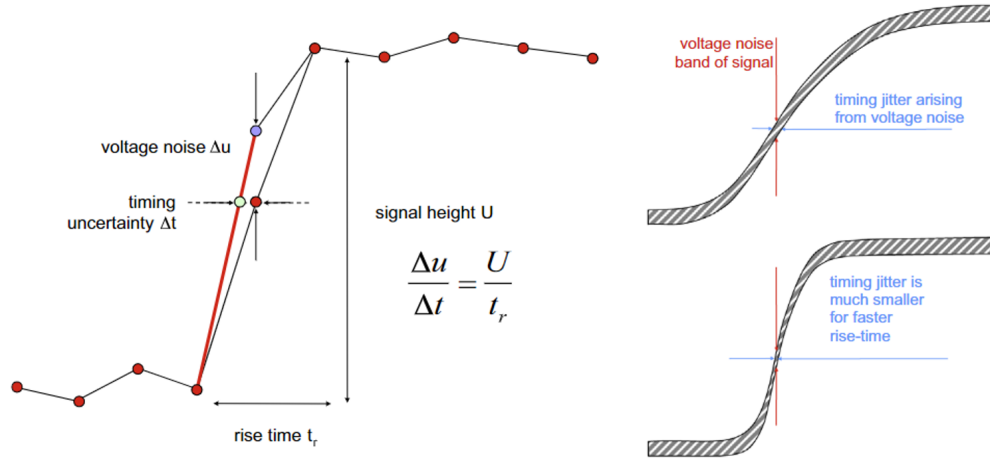


Figure 7.7: Left: Schematic showing how noise in the signal translates into a timing uncertainty Δt . Right: Illustration on how the rise time of the signal influences the impact of noise on timing. U is the signal height, Δu the voltage noise, t_r the rise time. (Figure taken from [107].

7.2.2 Measurement setup and procedure

The characterization setup described in Chapter 6 was adjusted to measure the timing properties of the AMCPs. A titanium sapphire laser was used as a pulsed laser source. The laser delivered pulses with an average pulse duration of ~ 200 fs. This ensured that the laser pulse's jitter was negligible compared to the expected detector resolution. The repetition rate of the laser was 1 kHz with a maximum pulse energy of 1 mJ. The initial beam was split, and half of it was sent to a fast photodiode, with a time resolution of ~ 2 ps, that was used for a reference signal. The remaining light was sent to a harmonic generator (STORC harmonic generator). The produced third harmonic at 258 nm was then guided into the vacuum chamber by an optical mirror. The initial beam diameter of around 1 mm was expanded to about 5 mm to cover the whole area of the AMCP sensor as evenly as possible. A thin gold photocathode was placed around 2 mm away from the AMCP sensor pads. An electron screen was placed between the detector and the photocathode to shield the wires and bonding pads from the incoming photoelectrons. The produced pulses were then recorded using a fast oscilloscope.

Two different AMCP chips were used during the testing. During the first part of the experiment, a chip with the standard design described in Chapter 5.1 was measured. An additional amplifier was connected outside the vacuum chamber. For the second round of measurements, the chip was replaced by one from the Planacon series and a specific board was designed with the AMCP directly connected to a LNA on the board. The setup is shown in Figure 7.8 and the measurement equipment and chip specifications are detailed in Table 7.2. Figure 7.9 shows the design of the test board.

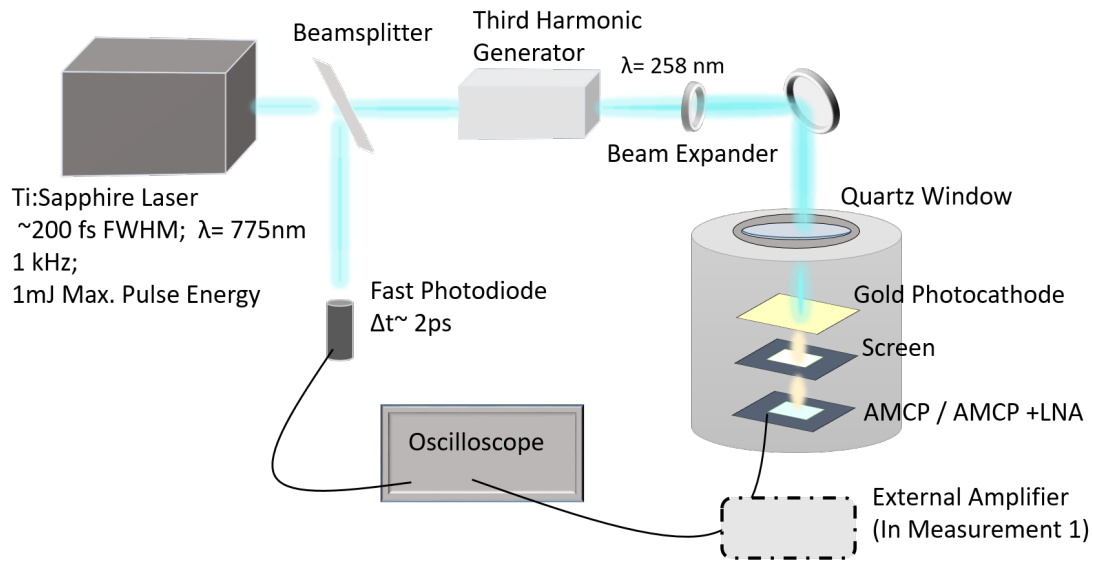


Figure 7.8: Schematic of the measurement setup used to determine the time resolution of the AMCPs. A fast laser (~200 fs pulse width) was used as an illumination source. A photodiode with a time resolution of around 2 ps served as a reference signal. The initial wavelength of 775 nm was converted by a third harmonic generator to 258 nm so that the same gold photocathode could be used as in previous characterization measurements. The laser beam then entered the vacuum chamber where the incoming photoelectrons generated a signal on the AMCP sensors. The outgoing signal was then connected to an amplifier (either outside the chamber or directly on the board) before being recorded by the oscilloscope.

Table 7.2: Equipment and specifications of the AMCP chips used in the time resolution measurements (AMCP Chip1 uses the standard AMCP design and AMCP Chip2 the Planacon design).

Equipment		
Laser (Ti-Sapphire)	Pulse duration	180 fs
	Pulse frequency	1 kHz Maximum
	Wavelength	775 nm / 258 nm (3 rd Harmonic)
	Pulse Intensity	1 mJ Maximum
Voltage Supply	Keithley 6487	-500 V (AMCP Bias)
	PS310	-700 V (Photocathode)
	RND 320-KA3005D	1.6 V (LNA)
Oscilloscope (WaveMaster 813 Zi-B)	Sampling rate	40 GS/s
	Bandwidth	13 GHz
Photodiode (Silicon)	Time Jitter	2 ps
	Rise time	<40 ps
	Bandwidth	7 GHz
	Spectral Range	630-1620 nm
Amplifier	Amplification	10 dB (ZFL-1000LN+) / 10 dB (LNA)
AMCP- Chip1/Chip2	Aspect Ratio	25 / 26.2
	Active Area	4.49% / 3.5%
	Sensor Area	500 μm^2 / 500 μm^2
	Capacitance	33 pF / 19 pF
	Gain	1500(at 500 V) / 1350(at 500 V)

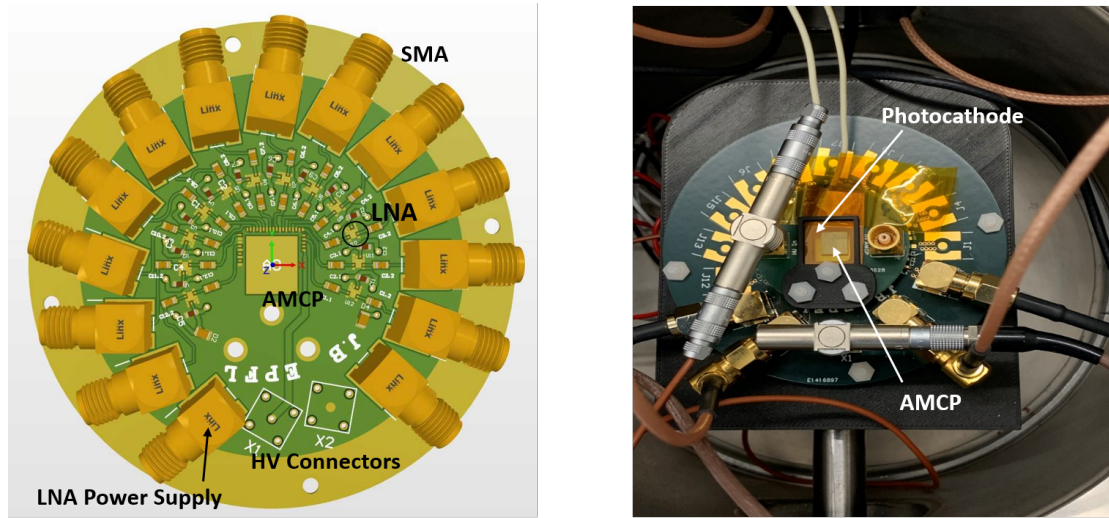


Figure 7.9: Design of the PCB used for the timing measurement. The AMCPs are directly connected to a LNA. (Board and LNA design were done by Jad Benserhir).

7.2.3 Time resolution with and without an external amplifier

In the first round of measurements the temporal response of the AMCP Chip1 was measured against the photodiode signal. First, the detector was measured alone and afterwards with an additional amplifier connected outside the chamber. For these measurements the laser beam was expanded to about 5 mm in diameter to fully cover the sensor areas. The AMCP with an area of $500 \mu\text{m}^2$ was biased at -500 V. The arrival time distribution was then measured under illumination of many photons. The initial laser pulse contained in the order of 10^{13} photons of which around 10^{10} ended up on the photocathode on top of the chip area. The exact quantum efficiency of the photocathode at this wavelength is not known; it is assumed to be around 0.0014 % based on previous measurements done with an UV lamp at a similar wavelength. This means that around 200 000 photoelectrons reached the detector surface and, taking into account the low active area of the used chip (4.49 %), that $\sim 10\,000$ electrons entered into the channels. This estimate could however easily be off by an order of magnitude depending on the exact quantum efficiency of the gold photocathode, losses along the path and inhomogenities in the beam intensity. Additionally, the metallic top electrode of the AMCP chip was expected to also produce a low number of photoelectrons in response to the residual light that passed through the gold photocathode.

The exact number of incoming electrons is not needed to measure the time resolution. However, the resolution of the sensor is expected to decrease with a lower number of incoming particles. A total of 5403 waveforms were accumulated, shown in Figure 7.10.

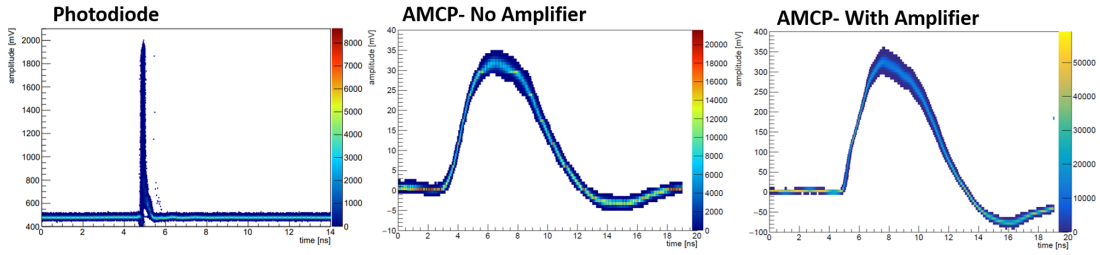


Figure 7.10: Recorded waveforms of the first measurement round. A total of 5403 waveforms were accumulated, showing the response of the photodiode (left), the AMCP without external amplifier (middle) and the AMCP with external amplifier (right).

The arrival times for each waveform at a given threshold (10 mV for the measurement without an amplifier and 50 mV for the measurement with an amplifier) were then plotted in a histogram and the resulting distribution fitted with a Gaussian function. The time resolution was then defined as the FWHM of the resulting Gaussian (occasionally the σ of the curve is mentioned, the two values are related by $\text{FWHM} = 2.35 \cdot \sigma$ as long as the distribution is actually gaussian shaped). Like this, a time resolution of (56.6 ± 0.3) ps for the AMCP without amplifier and (18.2 ± 0.1) ps for the AMCP with external amplifier was measured. The time distributions are shown in Figure 7.11.

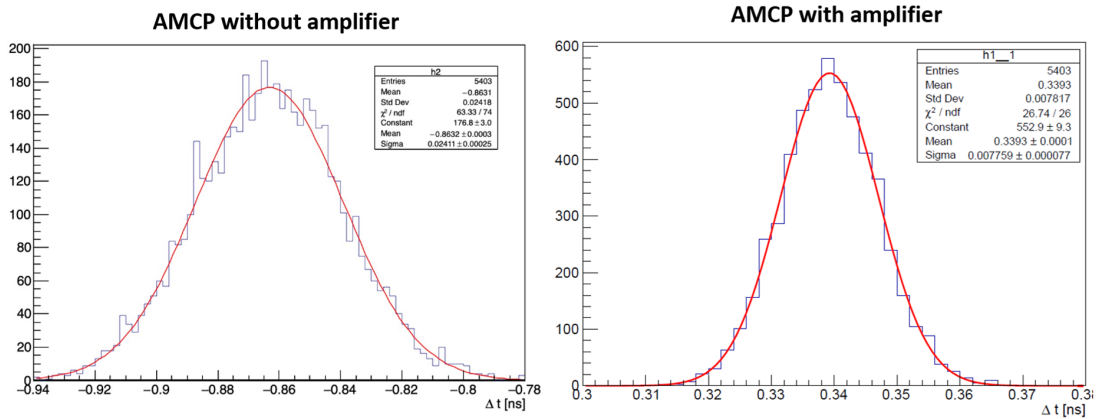


Figure 7.11: Distribution of arrival times and fitted Gaussian- without and with external amplifier.

The better time resolution for the the AMCP with an additional amplifier with respect to the on without is directly related to the bigger signal amplitude and, consequently, a higher signal-to-noise ratio. For the consequent measurements, the focus was put on the AMCP+ amplifier combination since, in the final detector architecture, the AMCP signal will be amplified by a low-noise amplifier.

Time walk correction

The measurement of the arrival time at a fixed threshold suffers from time walk errors- an error caused by the difference in signal amplitudes of the various waveforms. A time walk correction can be performed by plotting the arrival time difference of each waveform (Δt) versus the AMCP pulse charge (Q) and fitting a linear dependence $dt(Q)$. The corrected time resolution $\Delta t'$ can then be calculated according to:

$$\Delta t' = \Delta t - dt(Q). \quad (7.2)$$

With the applied correction, the time resolution of the AMCP+ amplifier configuration improved to (13.86 ± 0.1) ps. The distribution Δt vs. Q and the corrected arrival time distribution are shown in Figure 7.12.

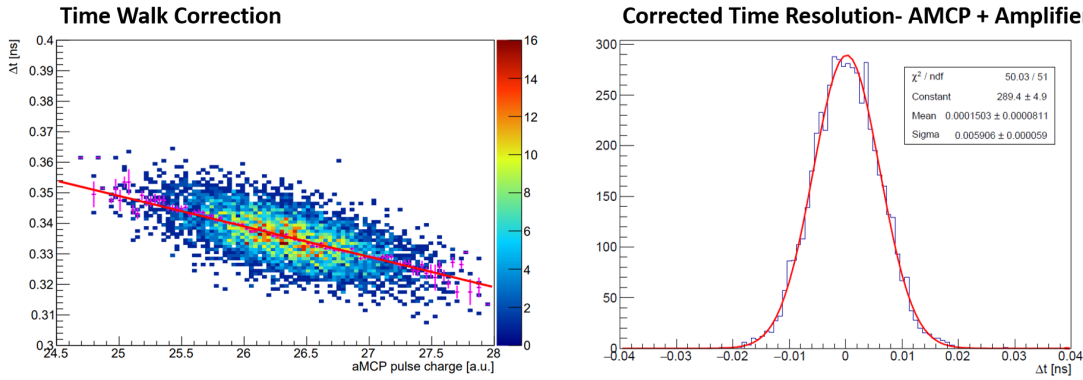


Figure 7.12: Plotting the arrival time difference versus the AMCP pulse charge shows a linear dependence between the two values (left). This can be used to correct for the time walk error, improving the time resolution of the AMCP with amplifier to (13.86 ± 0.1) ps.

7.2.4 Time resolution without additional photocathode

The first measurements were conducted with the standard gold photocathode placed above the AMCP chip. Even with the expanded laser spot, the photocathode appeared damaged after the first measurements, and its quantum efficiency was consequently reduced. For this reason, the gold photocathode was removed for the subsequent measurements. The metallic top electrode of the chip itself acted as a photocathode, although with an unknown quantum efficiency. Having the photoelectrons produced right at the channel's entrance can also help to achieve a better time resolution as no additional time spread is added from the photoelectrons crossing the gap between generation point to the sensor surface. On the downside, the gain of this architecture is lower since the energy of the first impact can not be optimized. The measurement is shown in Figure 7.13.

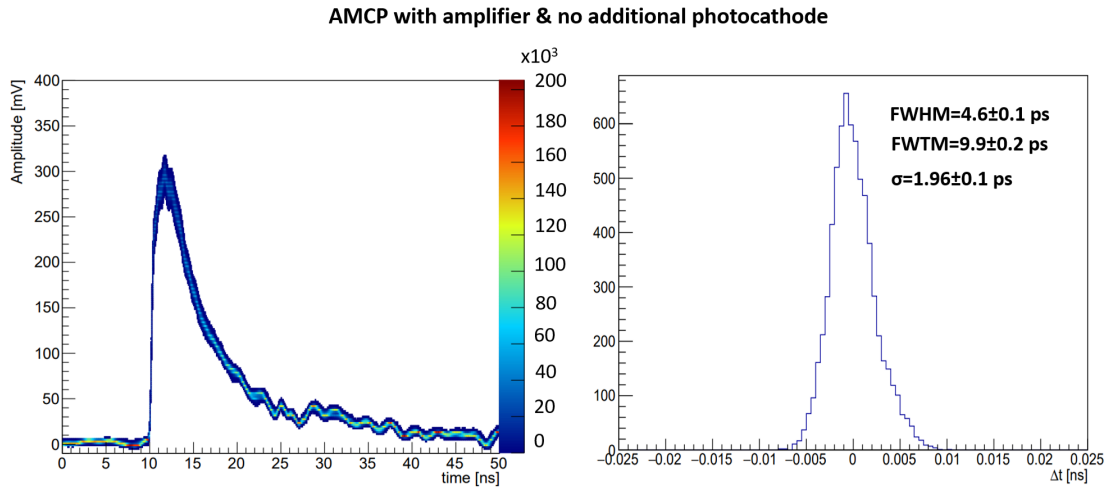


Figure 7.13: Accumulated waveforms (left) and arrival time distribution (right). A time resolution of (4.6 ± 0.1) ps could be measured.

From comparison with Figure 7.11 it can be seen that the average amplitude was slightly lower by removing the additional photocathode as the laser power was kept the same as before. This suggests that the efficiency of the gold photocathode was already significantly reduced during the previous measurements, and the top electrode produced the majority of the photoelectrons. The low flux of electrons from the gold layer only caused a broadening of the arrival time distribution due to the time it took the photoelectrons to reach the channel entrance. As expected, the arrival time distribution was narrower without the additional photocathode. A time resolution of (4.6 ± 0.1) ps could be achieved.

Time resolution with decreased flux

For the previous measurements, the number of incoming particles was still much higher than in the envisioned prototype PET detector, where the time resolution for single photoelectrons will be of importance. In the subsequent measurement, the laser intensity was first reduced by a factor of two (still without the additional photocathode) which decreased the time resolution to (10.8 ± 0.1) ps as shown in Figure 7.14. The lowest beam intensity that was tested was 100 nJ. The resulting arrival time distribution is shown in Figure 7.15. The time resolution further decreased to (12.6 ± 0.2) ps.

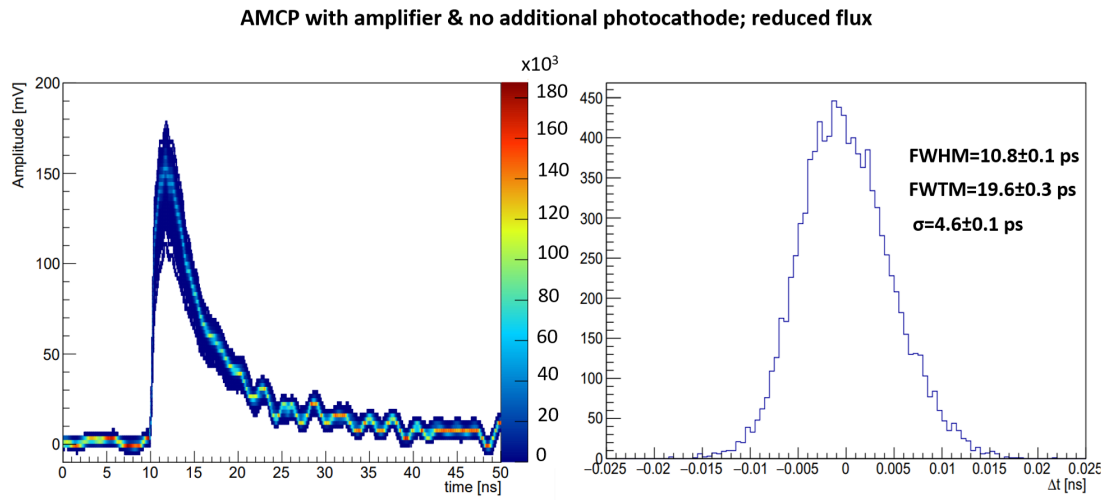


Figure 7.14: Accumulated waveforms (left) and arrival time distribution (right) for 160 nJ pulses. A time resolution of (10.8 ± 0.1) ps could be measured.

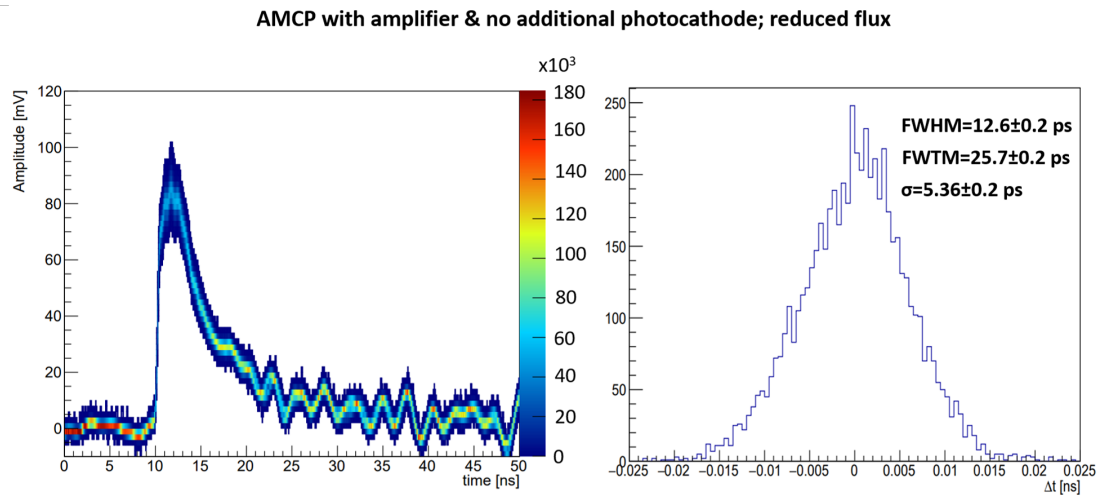


Figure 7.15: Accumulated waveforms (left) and arrival time distribution (right) for a 100 nJ beam. A time resolution of (12.6 ± 0.2) ps could be measured.

As expected, the time resolution decreases when the number of incident photoelectrons is lowered. Even at an intensity of 100 nJ and with the low quantum efficiency of the metallic photocathode, the estimated number of photoelectrons entering the channels is still between several hundred to a few thousand. This means that the time resolution for a single photoelectron is still expected to be worse than the measured $\Delta t = (12.6 \pm 0.2)$ ps. The exact relationship between the number of incoming photoelectrons and the time resolution is complex as it additionally depends on whether the electrons enter one or several channels. The beam was spread evenly over the measured sensor and there were about 17500 channels per sensor. Hence, at this beam intensity there shouldn't be more than one photoelectron per channel. In this regime a further decrease of the beam intensity will decrease the time resolution according to Equation 7.1 until the single photoelectron regime is reached. The measured time resolution (FWHM) was plotted as a function of the AMCP amplitude (A) and fitted with a function of the form $\Delta t = C_1 / A$ in Figure 7.16 to have a rough idea of how the time resolution will change with even lower fluxes. In future measurements, the laser beam should be further attenuated until a point is reached where only a fraction of laser pulses produce a signal, indicating that statistically, only a few photoelectrons enter the channels.

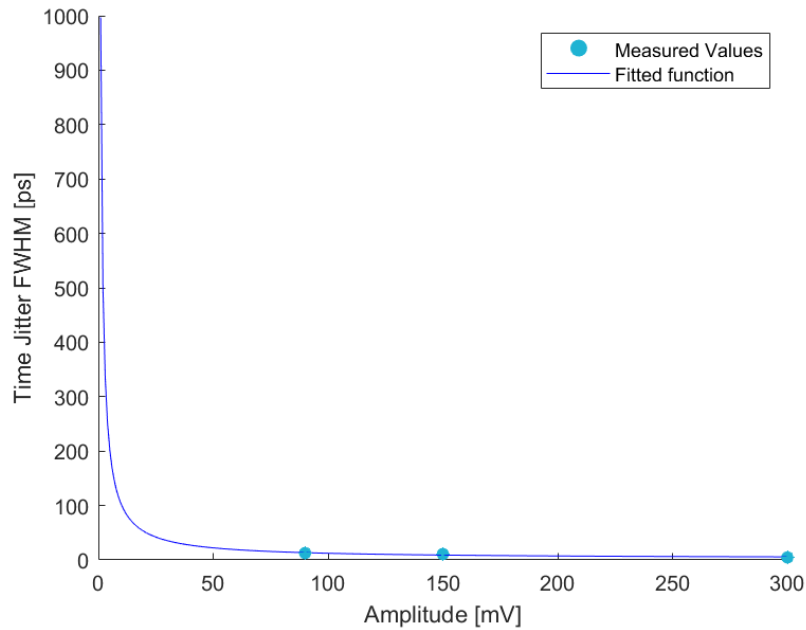


Figure 7.16: Measured time jitter as a function of the signal amplitude. A function of the form $\Delta t = C_1 / A$ was fitted to the data points.

7.2.5 Integrated amplifier

In a further measurement, the AMCP Chip1 was exchanged with one of the Planacon series (AMCP Chip2) where the capacitance of the $500\text{ }\mu\text{m}^2$ area was reduced to 19 pF. This time the chip was directly bonded to a LNA on the board inside the chamber to achieve more similar conditions as in the final integrated detector architecture. The AMCP could only be biased with -300 V due to a shunt. This means that the gain was significantly reduced to about 300 (this value could be actually even lower due to the lowered energy of the first impact). For this reason the beam intensity had to be increased again. The measured time resolution was (6.1 ± 0.2) ps (FWHM) in the high flux regime. Even though the signal intensity was very low, due to the low gain of the sensor, the achieved timing resolution was still very promising—especially when compared to the first measurement without any connected amplifier with a similar amplitude (Figure 7.11). This indicates that the achievable time resolution can still be significantly improved by shortening the distance between the AMCP anode and the amplifier and by eventually having a fully monolithically integrated detector.

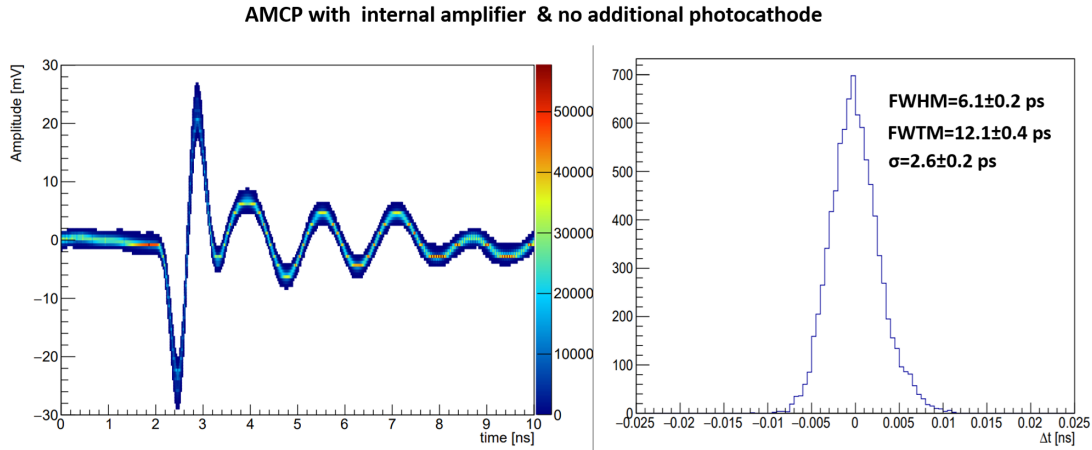


Figure 7.17: Accumulated waveforms (left) and arrival time distribution (right). A time resolution of (6.1 ± 0.2) ps (FWHM) could be measured.

The practical problems with shunts on the AMCP chip were caused by the wire bonds that were placed too close to the grounded area of the intermediate electrode, making the placement of the wires extremely critical. This design should be updated for future sets of test chips to remove the grounded metal area in the vicinity of the bonding pads.

7.3 Conclusion and outlook

This chapter presented the first steps toward the final TOF-PET detector. Three AMCP chips have been prepared and assembled into a Planacon phototube. The highly efficient photocathode of the Planacon assembly will allow performing the first measurements of the coincidence timing resolution. The arrival time jitter has been measured for the first time. A high time resolution of (4.6 ± 0.1) ps (FWHM) could be measured in the high flux regime. By decreasing the flux of photoelectrons to roughly a few hundred to thousands, this value increased to (12.6 ± 0.2) ps (FWHM).

In the future, these measurements should be repeated using funnel-shaped detectors to have a high active area and further decrease the laser power until the single photoelectron regime is reached. However, in its current state, the AMCP gain might not be high enough to be sensitive to single photoelectrons, given the already low signal amplitude with a few hundred incoming photoelectrons. There is still potential to further increase the gain by optimizing the MgO layer. It should also be noted that the gain was reduced during these measurements due to the removal of the photocathode and the hence lowered energy of the first impact. Alternatively, the gain of the LNA will have to be increased.

For the successful application in a Cherenkov TOF-PET scanner, a coincidence time resolution of around 10 ps (FWHM) is needed. The coincidence time resolution σ_C is related to the time resolution of a single AMCP detector σ by:

$$\sigma_C^2 = \sqrt{\sigma_{AMCP1}^2 + \sigma_{AMCP2}^2} \longrightarrow \sigma_C = \sqrt{2}\sigma, \quad (7.3)$$

assuming the response of the two AMCP detectors to be the same $\sigma_{AMCP1} = \sigma_{AMCP2}$. This means that the timing requirement is currently only fulfilled for high incoming fluxes. It is, however, essential to note that the final resolution will be improved significantly by having a monolithically integrated sensor. This was evident from the measurement presented in 7.2.5, where the AMCP chip and LNA were connected on the same readout board rather than over a cable outside the chamber.

To conclude, although these first measurements of the timing resolution are extremely promising, further optimization is still required for the envisioned complete detector architecture. Besides the obvious need for the funnel-shaped openings to achieve the needed active area, the output capacitance should also be further reduced, and the AMCP needs to be integrated with the amplifier. In the case of single photoelectron counting, it needs to be verified whether the amplification of the LNA should be increased to be sensitive enough. This will, however, also affect power consumption. The needed power of the amplifier also depends on the capacitance of the AMCPs, which is why it will be essential to decrease this value as much as possible. In these test chips, the sensor area was kept relatively small ($500 \mu\text{m}^2$). In the final integration, the AMCP area will depend on the chosen granularity (readout pixels) and could be much larger; hence the capacitance would increase.

8 Discussion and Outlook

In this last chapter, the main results obtained during the duration of this thesis are summarized, and the research questions posed in the introduction are discussed. Afterward, the possibilities and limitations of the technology are explored, and future activities and applications are presented.

8.1 Summary of the main results

8.1.1 AMCP fabrication

One of the main focuses was on optimizing the fabrication processes. Although earlier generations of AMCP served as proof of concept, their gain values were far too low to be considered for any meaningful application. One key aspect was the optimization of a-Si:H deposition by PE-CVD to avoid structural defects in the layer. This was done by carefully controlling intrinsic stress and hydrogen diffusion during the deposition process. The high-quality layers that could be achieved later allowed the application of strong electric fields, which is crucial for achieving high multiplication factors inside the channels. By combining photo-lithographic and DRIEs processes, channels with small diameters down to $1.6\text{ }\mu\text{m}$ and aspect ratios of 25 could be realized. As observed in simulations, small channel diameters help to achieve optimum timing characteristics of the detectors. One of the AMCP technology's key strengths is the fabrication process's flexibility, which allows tuning channel geometry to best fit a specific application. This was demonstrated by the realization of the first sensors with a funnel-shaped opening on top, ensuring a high active area of around 95 %. Paths towards further device optimization were shown by introducing fabrication methods to decrease the output capacitance of the detectors, which may be an important aspect in real applications. The capacitance was decreased by 30 % by increasing the decoupling layer thickness. A further decrease down to a few pF, depending on the planned sensor area, is achievable by either further increasing the thickness of the decoupling layer or redesigning the intermediate electrode layout.

The channel geometry of future devices could also be adjusted to have a trench-like shape. This allows for the etching of deeper structures due to the easier gas access during the Bosch process. Thus, even higher gains might be achievable, as demonstrated by simulations. Finally, the possibility of wall coatings was explored to enhance the SEY of the channel walls. This can be done by ALD processes where the entire channel area is conformally coated or, in the case of the funnel structure, by sputtering just the funneled part of the channel. With the SEY being highly dependent on the surface structure of the coated material, this step can still be further optimized. In the future, two different materials could be envisioned on the funnel walls and the straight part of the channels. In this way, the SEY could be optimized for the energy of the colliding electrons- for highly energetic particles in the upper part (funnel opening) and low energy collisions in the lower part (cylindrical channel part).

8.1.2 AMCP gain and timing properties

The fabricated devices were characterized under continuous and pulsed illumination. The multiplication gain could be increased up to around 1500 from the maximum of around 100 obtained in previous AMCP generations. This gain value is high enough for the integration of AMCPs with readout circuits. In previous generation of devices, a voltage rise on the intermediate electrode led to an unstable gain with time. With the newest generations with a more conductive chromium-based intermediate electrode, this effect could be drastically reduced, resulting in a more reproducible gain value over time. Characterization with a fast laser source provided the first insight into the temporal characteristics of the fabricated AMCPs. Since, in most applications, the incoming current is pulsed rather than continuous, it was also important to characterize the devices in this regime. No significant difference between gain values obtained in continuous or pulsed regime for strong electric fields could be observed. This observation means that no saturation effects were occurring under the applied measurement conditions. These measurement conditions will have to be expanded to include larger incoming currents in future experiments. Saturation effects should start to be observable once the current needed to replenish the charges in the channel is of a similar value to the one flowing through the stack (leakage current). However, a difference between the two gain values was measured for low biases (weak electric fields) in devices of the MCP152 series. This effect could be related to a charging effect of the decoupling layer stack and should be further explored in the future. The timing resolution of the AMCP was measured for the first time. By having the AMCP connected to an additional amplifier, a time resolution of (4.6 ± 0.1) ps at FWHM could be deduced. The resolution worsens for lower fluxes due to the decreased SNR. To keep this excellent time resolution for very low fluxes, the gain of the entire detector should be further increased- either by enhancing the gain of the AMCP itself (see Outlook below) or the connected amplifier.

It could also be shown that this resolution can be further increased by having the AMCP chip and the amplifier at a close distance so that signal noise is reduced to a minimum. In the future, an entirely monolithically integrated device should be fabricated to exploit the timing performance of the AMCP fully. The first funnel-shaped AMCP with an active area of 95 % and a MgO coating on top was characterized, resulting in a gain of around 451 at a bias of 350 V. Higher bias voltages could not be applied to the chip due to electrical breakdown taking place at higher voltages. However, a gain of 1578 at 500 V bias was extrapolated from the measurements. This gain value lies in the expected range taking into account the lower energy at the first impact during the measurement performed without a photocathode. The problem with high bias voltages will have to be addressed in future funnel AMCP designs. Furthermore, the SEY of MgO could also be influenced by the deposition parameter and the chosen layer thickness. The effects of these parameters should be investigated by measuring the SEY as a function of energy and angle (as done by [54]) for various deposition recipes to find the best option for our devices.

8.2 Discussion of the research questions

In this section the formulated research questions are addressed one by one.

1. What is the minimal AMCP gain needed for their use in real applications, such as TOF-PET scanners, and which other requirements need to be fulfilled?

The gain of the AMCP needs to be high enough to result in a signal that an electronic readout can record. The exact value, of course, depends on the incoming signal, the noise, and the needed threshold of the readout electronics. In this thesis, it could be shown that the achieved gain of around 1500 is high enough to detect a minimum incoming flux of a few hundred photoelectrons. A few single photoelectrons are expected in the envisioned prototype detector as an incoming current. The detection of a single photoelectron could not yet been demonstrated and might need further enhancement of the multiplication gain to achieve the desired SNR. There is still considerable potential for gain increase by pushing further the aspect ratio and by introducing high secondary emission coatings such as MgO that could either be sputtered on the funneled channel opening or fully deposited on the channel interior by an ALD process.

Besides a high enough gain, the detector also needs a high detection efficiency due to the very low number of expected incoming photoelectrons. Two quantities define the detection efficiency- one is the sensor's active area, and the other is the probability of producing secondary electrons inside the channel. The active area is entirely a geometrical aspect and has been shown to increase to around 95 % with the presented funnel opening. The second component is related to the SEY being Poisson distributed. The higher the mean of the yield distribution, the lower the possibility of producing zero secondary electrons for an impact. As seen in simulations, this detection efficiency drastically increases when MgO is used rather than a-Si:H especially for the first impact, which this is the most critical. The MgO deposition still needs to be further optimized to have the optimum overall detection efficiency.

The other requirement for PET application is the high timing resolution (close to 10 ps). The measured timing jitter is in the needed range. Although the jitter for a single incident photoelectron could not yet be determined, the measurements at a low flux show, with the possibility of further improvements, that the final timing resolution should be sufficient for using AMCPs in a PET scanner. Another possibility would be to use AMCPs in combination with scintillation crystals. Although the scintillation process is slower than Cherenkov radiation, they yield a higher number of photons per gamma interaction. Together with the fast timing of AMCPs, this could result in a better PET image quality than the proposed Cherenkov detector. However, a simulation of a whole PET scanner architecture is necessary to fully answer this question. Overall, it can be concluded that the development of AMCPs has matured to a point where they can be implemented in real applications.

2. Can the fabrication process of AMCPs be improved to meet these requirements?

The AMCP fabrication could be improved to achieve the needed gain and timing properties. Optimizing the PE-CVD process allowed deposited a-Si:H layers with a low number of structural defects. This is essential to apply strong electric fields on the final devices. By tuning the photolithography and DRIE processes, channels with a diameter down to $1.6\mu\text{m}$ could be fabricated, resulting in aspect ratios up to 25. This drastically increased the multiplication gain of the channels up to 1500. The implementation of a metallic intermediate electrode also ensured more stable gain dynamics. The small channel diameters also assist in achieving the best possible time resolution. Finally, the detection efficiency could be enhanced up to 95 % by etching funnel-shaped channel openings.

3. What are the advantages and limits of AMCPs, and can they overcome some of the limitations of conventional MCPs?

AMCPs have already been proven to be more flexible concerning their fabrication processes. Channel diameters are smaller than what can be achieved with conventional glass MCPs (with a minimum of $2\mu\text{m}$). Full monolithic integration with the readout electronic has not yet been realized, but this could potentially result in a better time and spatial resolution than what conventional MCPs can achieve, which are limited by a necessary vacuum gap between the channel end and the anode. Another advantage that has not yet been explored is the possibility of having a faster charge replenishment due to the strip current flowing directly through the stack and being less sensitive to saturation effects. The main distinction between AMCPs and MCPs in terms of their behavior is the difference in charge replenishment. The strip current of AMCPs flows directly through the bulk material, whereas in MCPs, it is confined to a conductive layer along the channel walls. The flowing current is also higher than that of MCPs, where the resistivity of the conducting layer can not be reduced indefinitely due to the risk of thermal runaways. This fact can be of importance for achieving a fast charge replenishment. The main limitation of AMCPs is still given by their multiplication gain. Although this value was increased to 1500 and can still be further optimized, AMCPs can not be stacked on top of each other, and the reliable etching of tilted channels comes with technical difficulties.

8.3 Outlook

During this thesis, AMCPs have matured from earlier versions to a point where they can now be envisioned for real applications. In the near future, a full monolithic detector should be fabricated where the AMCP will be directly grown on the readout electronics. The possibility of monolithic integration is one of the key strengths of AMCPs. It should allow to fully exploit the high temporal and spatial resolution of these devices. The flexibility in the fabrication process will also allow to perfectly adjust the channel geometry to the readout design underneath allowing high spatial resolutions.

Although the maximum gain of AMCPs is still lower than that of conventional MCPs, it is high enough to detect low to medium fluxes. AMCPs have not yet been tested for single particle counting. For this application, it would be preferential to further increase the gain to enhance the SNR. There are still various possibilities to do so. The channel aspect ratios fabricated by deep reactive ion etching processes have not yet reached their limit. They can still be further pushed to values around 35-40 by the optimization of the process parameters. Simulations showed that gains up to 7000 are achievable with these aspect ratios. Channel wall coatings also provide a vast potential to increase the gain further. Measurement of previous devices proved that the gain could be increased by almost a factor of two by using alumina coating and possibly even more for MgO. For this, the issue with charge collection caused by the ALD layer will have to be addressed and resolved. Considering the potential increase in aspect ratio and the successful application of wall coatings, AMCP multiplication gains up to 10000 are feasible. Another advantage of AMCP is the possibility of minimizing saturation effects by tuning the a-Si:H layer's conductivity. This approach has not yet been investigated. By having a fast charge replenishment, AMCP could be envisioned for applications where high count rates are required. A few other critical aspects were not yet investigated, such as the dark count rate and the detection efficiency. Characterizing these values will allow for a complete picture of the AMCPs properties and evaluate the best-suited applications.

Overall, AMCPs could be envisioned in a wide range of applications. Besides the discussed medical imaging systems, AMCPs could also be utilized in space and high-energy physics applications due to the radiation hardness of a-Si:H and its tolerance to magnetic fields. AMCP could also be utilized in neutron detection since the high hydrogen content of the a-Si:H layer promotes neutron-proton interactions. Finally, AMCPs could also be implemented in mass spectrometer, where saturation effects of the conventional glass MCPs often cause a loss of sensitivity.

Bibliography

- [1] R. Bar-Shalom, A. Y. Valdivia, and M. D. Blaufox, “Pet imaging in oncology”, in *Seminars in nuclear medicine*, Elsevier, vol. 30, 2000, pp. 150–185.
- [2] S. Vandenberghe, E. Mikhaylova, E. D’Hoe, P. Mollet, and J. S. Karp, “Recent developments in time-of-flight pet”, *EJNMMI physics*, vol. 3, no. 1, pp. 1–30, 2016.
- [3] M. H. Brodsky, R. S. Title, K. Weiser, and G. D. Pettit, “Structural, optical, and electrical properties of amorphous silicon films”, *Phys. Rev. B*, vol. 1, pp. 2632–2641, 6 Mar. 1970. DOI: 10.1103/PhysRevB.1.2632.
- [4] H. Sterling and R. Swann, “Chemical vapour deposition promoted by rf discharge”, *Solid-State Electron.*, vol. 8, no. 8, pp. 653–654, 1965.
- [5] N. Hata and S. Wagner, “A comprehensive defect model for amorphous silicon”, *J. Appl. Phys.*, vol. 72, no. 7, pp. 2857–2872, 1992.
- [6] Z. Moss and J. Graczyk, “Evidence of voids within the as-deposited structure of glassy silicon”, *Phys. Rev. Lett.*, vol. 23, no. 20, p. 1167, 1969.
- [7] M. Van Den Boogaard, S. Jones, Y. Chen, *et al.*, “The influence of the void structure on deuterium diffusion in a-si: h”, *MRS Online Proceedings Library (OPL)*, vol. 258, 1992.
- [8] R. Chittick, J. Alexander, and H. Sterling, “The preparation and properties of amorphous silicon”, *J. Electrochem. Soc.*, vol. 116, no. 1, p. 77, 1969.
- [9] I. L. Staebler and C. Wronski, “Reversible conductivity changes in discharge-produced amorphous si”, *Appl. Phys. Lett.*, vol. 31, no. 4, pp. 292–294, 1977.
- [10] M. Despeisse, “Etude et caractérisation d’un capteur en silicium amorphe hydrogéné déposé sur circuit intégré pour la détection de particules et de rayonnements”, Ph.D. dissertation, INSA, Villeurbanne, 2006.
- [11] K. Winer and L. Ley, “Surface states and the exponential valence-band tail in a-si: h”, *Phys. Rev. B*, vol. 36, no. 11, p. 6072, 1987.
- [12] M. Tanielian, “Adsorbate effects on the electrical conductance of a-si: h”, *Philosophical Magazine B*, vol. 45, no. 4, pp. 435–462, 1982.
- [13] W. Spear and P. L. Comber, “Electronic properties of substitutionally doped amorphous si and ge”, *Philosophical Magazine*, vol. 33, no. 6, pp. 935–949, 1976.

- [14] M. Stutzmann, D. K. Biegelsen, and R. A. Street, “Detailed investigation of doping in hydrogenated amorphous silicon and germanium”, *Phys. Rev. B*, vol. 35, pp. 5666–5701, 11 Apr. 1987. DOI: 10.1103/PhysRevB.35.5666.
- [15] C. R. Wronski and R. E. Daniel, “Photoconductivity, trapping, and recombination in discharge-produced, hydrogenated amorphous silicon”, *Phys. Rev. B*, vol. 23, no. 2, p. 794, 1981.
- [16] N. Wyrsh, C. Miazza, S. Dunand, *et al.*, “Radiation hardness of amorphous silicon particle sensors”, *J. Non-Cryst. Solids*, vol. 352, no. 9-20, pp. 1797–1800, 2006.
- [17] W. Spear and P. Le Comber, “Substitutional doping of amorphous silicon”, *Solid State Commun.*, vol. 17, no. 9, pp. 1193–1196, 1975.
- [18] D. E. Carlson and C. R. Wronski, “Amorphous silicon solar cell”, *Appl. Phys. Lett.*, vol. 28, no. 11, pp. 671–673, 1976.
- [19] A. Franco, “Monolithic particle detectors based on hydrogenated amorphous silicon”, EPFL, Tech. Rep., 2014.
- [20] W. Schwarzenbach, A. Howling, M. Fivaz, S. Brunner, and C. Hollenstein, “Sheath impedance effects in very high frequency plasma experiments”, *J. Vac. Sci. Technol.*, vol. 14, no. 1, pp. 132–138, 1996.
- [21] P. Chabloz, H. Keppner, D. Fischer, D. Link, and A. Shah, “Amorphous silicon pin diodes, deposited by the vhf-gd process: new experimental results”, *J. Non-Cryst. Solids*, vol. 198, pp. 1159–1162, 1996.
- [22] J. L. Wiza, “Microchannel plate detectors”, 1979, pp. 587–601.
- [23] G. W. Fraser, M. T. Pain, and J. E. Lees, “Microchannel plate operation at high count rates : further studies”, 1993, pp. 328–336.
- [24] E. H. Eberhardt, “Gain model for microchannel plates”, *Appl. Opt.*, vol. 18, no. 9, pp. 1418–1423, 1979.
- [25] E. Eberhardt, “An operational model for microchannel plate devices”, *IEEE Trans. Nucl. Sci.*, vol. 28, no. 1, pp. 712–717, 1981.
- [26] G. J. Price and G. W. Fraser, “Calculation of the output charge cloud from a microchannel plate”, 2001, pp. 188–196.
- [27] C. A. Kruschwitz, M. Wu, and G. A. Rochau, “Monte carlo simulations of microchannel plate detectors. ii. pulsed voltage results”, *Rev. Sci. Instrum.*, vol. 82, no. 2, p. 023 102, 2011.
- [28] “Beam test of a time-of-flight detector prototype”, *NIM-A*, vol. 606, pp. 404–410, 3 Jul. 2009, ISSN: 01689002. DOI: 10.1016/j.nima.2009.04.053.
- [29] A. Tremsin and J. Vallergera, “Unique capabilities and applications of microchannel plate (mcp) detectors with medipix/timepix readout”, *Radiat.*, vol. 130, p. 106 228, 2020.
- [30] A. Lehmann, A. Britting, W. Eyrich, *et al.*, “Tremendously increased lifetime of mcp-pmts”, *NIM-A*, vol. 845, pp. 570–574, 2017.

- [31] G. W. Fraser, M. T. Pain, J. E. Lees, and J. F. Pearson, "The operation of microchannel plates at high count rates", 1991, pp. 247–260.
- [32] "Lifetime of mcp-pmt", *NIM-A*, vol. 564, pp. 204–211, 1 Aug. 2006, ISSN: 01689002. DOI: 10.1016/j.nima.2006.04.089.
- [33] T. M. Conneely, J. S. Milnes, and J. Howorth, "Extended lifetime mcp-pmts: characterisation and lifetime measurements of ald coated microchannel plates, in a sealed photomultiplier tube", *NIM-A*, vol. 732, pp. 388–391, 2013, ISSN: 01689002. DOI: 10.1016/j.nima.2013.07.023.
- [34] A. Lehmann, M. Böhm, D. Miehl, *et al.*, "Latest improvements of microchannel-plate pmts", *NIM-A*, vol. 958, Apr. 2020, ISSN: 01689002. DOI: 10.1016/j.nima.2019.162357.
- [35] E. V. Antamanova, I. G. Bearden, E. J. Garcia-Solis, *et al.*, "Anode current saturation of ald-coated planacon mcp-pmts", *J. Instrum.*, vol. 13, 9 Sep. 2018, ISSN: 17480221. DOI: 10.1088/1748-0221/13/09/T09001.
- [36] M. A. Popecki, B. Adams, C. A. Craven, *et al.*, *Microchannel plate fabrication using glass capillary arrays with atomic layer deposition films for resistance and gain*, Aug. 2016. DOI: 10.1002/2016JA022580.
- [37] N. Wyrsh, F. Powolny, M. Despeisse, S. Dunand, P. Jarron, and C. Ballif, "Micro-channel plate detectors based on hydrogenated amorphous silicon", *MRS Online Proceedings Library (OPL)*, vol. 1245, 2010.
- [38] A. Franco, Y. Riesen, N. Wyrsh, *et al.*, "Amorphous silicon-based microchannel plates", *NIM-A*, vol. 695, pp. 74–77, 2012.
- [39] A. Franco, J. Geissbühler, N. Wyrsh, and C. Ballif, "Fabrication and characterization of monolithically integrated microchannel plates based on amorphous silicon", *Sci. Rep.*, vol. 4, no. 1, pp. 1–7, 2014.
- [40] L. Austin and H. Starke, "Ueber die reflexion der kathodenstrahlen und eine damit verbundene neue erscheinung secundärer emission", *Ann. Phys.*, vol. 314, no. 10, pp. 271–292, 1902.
- [41] D. E. Wooldridge, "Theory of secondary emission", *Phys. Rev.*, vol. 56, pp. 562–578, 6 Sep. 1939. DOI: 10.1103/PhysRev.56.562.
- [42] E. M. Baroody, "A theory of secondary electron emission from metals", *Phys. Rev.*, vol. 78, pp. 780–787, 6 Jun. 1950. DOI: 10.1103/PhysRev.78.780.
- [43] H. Seiler, "Secondary electron emission in the scanning electron microscope", *J. Appl. Phys.*, vol. 54, no. 11, R1–R18, 1983.
- [44] I. Bronshtein and B. S. Fraiman, "Vtorichnaya elektronnaya emissiya.(secondary electron emission).", 1969.
- [45] K. Kanaya and H. Kawakatsu, "Secondary electron emission due to primary and backscattered electrons", *J. Phys. D: Appl. Phys.*, vol. 5, no. 9, p. 1727, 1972.

- [46] K. Nishimura, T. Itotani, and K. Ohya, “Influence of surface roughness on secondary electron emission and electron backscattering from metal surface”, *Jpn. J. Appl. Phys.*, vol. 33, no. 8R, p. 4727, 1994.
- [47] A. R. Dzhanoev, F. Spahn, V. Yaroshenko, H. Lühr, and J. Schmidt, “Secondary electron emission from surfaces with small structure”, *Phys. Rev. B*, vol. 92, p. 125 430, 12 Sep. 2015. DOI: 10.1103/PhysRevB.92.125430.
- [48] C. Swanson and I. D. Kaganovich, “Modeling of reduced effective secondary electron emission yield from a velvet surface”, *J. Appl. Phys.*, vol. 120, no. 21, p. 213 302, 2016.
- [49] P. A. Redhead, J. P. Hobson, and E. V. Kornelsen, *The physical basis of ultrahigh vacuum*. Springer, 1968.
- [50] A. Shih, J. Yater, C. Hor, and R. Abrams, “Secondary electron emission studies”, *Appl. Surf. Sci.*, vol. 111, pp. 251–258, 1997.
- [51] D. C. Joy, “A database on electron-solid interactions”, *Scanning*, vol. 17, no. 5, pp. 270–275, 1995.
- [52] H. Schade and J. Pankove, “Photoemission from cesiated hydrogenated amorphous silicon”, *Surface Science*, vol. 89, no. 1-3, pp. 643–648, 1979.
- [53] J. Lapington, D. Thompson, P. May, *et al.*, “Investigation of the secondary emission characteristics of cvd diamond films for electron amplification”, *NIM-A*, vol. 610, no. 1, pp. 253–257, 2009.
- [54] J. Löffler, C. Ballif, and N. Wyrsh, “Amorphous silicon-based micro-channel plate detectors with high multiplication gain”, *NIM-A*, vol. 912, pp. 343–346, 2018.
- [55] N. Wyrsh, C. Miazza, C. Ballif, *et al.*, “Vertical integration of hydrogenated amorphous silicon devices on cmos circuits”, *MRS Online Proceedings Library (OPL)*, vol. 869, 2005.
- [56] J. S. Milnes and J. Howorth, “Picosecond time response characteristics of microchannel plate pmt detectors”, in *26th International Congress on High-Speed Photography and Photonics*, SPIE, vol. 5580, 2005, pp. 730–740.
- [57] M. Galanti, R. Gott, and J. Renaud, “A high resolution, high sensitivity channel plate image intensifier for use in particle spectrographs”, *Rev. Sci. Instrum.*, vol. 42, no. 12, pp. 1818–1822, 1971.
- [58] H. Tan, Y. Gu, H. Yu, *et al.*, “Total-body pet/ct: current applications and future perspectives”, *AJR*, vol. 215, no. 2, pp. 325–337, 2020.
- [59] C. Tsoumpas, D. Visvikis, and G. Loudos, “Innovations in small-animal pet/mr imaging instrumentation”, *PET clinics*, vol. 11, no. 2, pp. 105–118, 2016.
- [60] M. M. Ter-Pogossian, M. E. Phelps, E. J. Hoffman, and N. A. Mullani, “A positron-emission transaxial tomograph for nuclear imaging (pett)”, *Radiology*, vol. 114, no. 1, pp. 89–98, 1975.
- [61] T. Jones and D. W. Townsend, “History and future technical innovation in positron emission tomography”, *J. Med. Imaging*, vol. 4, no. 1, p. 011 013, 2017.

- [62] S. N. Reske and J. Kotzerke, “Fdg-pet for clinical use”, *Eur. J. Nucl. Med.*, vol. 28, no. 11, pp. 1707–1723, 2001.
- [63] L. Jødal, C. Le Loirec, and C. Champion, “Positron range in pet imaging: an alternative approach for assessing and correcting the blurring”, *PMB*, vol. 57, no. 12, p. 3931, 2012.
- [64] S. R. Cherry, “The 2006 henry n. wagner lecture: of mice and men (and positrons)—advances in pet imaging technology”, *J. Nucl. Med.*, vol. 47, no. 11, pp. 1735–1745, 2006.
- [65] M. E. Raichle, “Positron emission tomography”, *Annu. Rev. Neurosci.*, vol. 6, no. 1, pp. 249–267, 1983.
- [66] H. Zaidi and M.-L. Montandon, “Scatter compensation techniques in pet”, *PET clinics*, vol. 2, no. 2, pp. 219–234, 2007.
- [67] D. L. Snyder, L. J. Thomas, and M. M. Ter-Pogossian, “A matheemactical model for positron-emission tomography systems having time-of-flight measurements”, *IEEE Trans. on Nuclear Science*, vol. 28, no. 3, pp. 3575–3583, 1981.
- [68] E. Berg and S. R. Cherry, “Innovations in instrumentation for positron emission tomography”, in *Seminars in nuclear medicine*, Elsevier, vol. 48, 2018, pp. 311–331.
- [69] T. Jones and D. W. Townsend, “History and future technical innovation in positron emission tomography”, *J. Med. Imaging*, vol. 4, no. 1, p. 011 013, 2017.
- [70] J. S. Reddin, J. S. Scheuermann, D. Bharkhada, *et al.*, “Performance evaluation of the sipm-based siemens biograph vision pet/ct system”, in *2018 IEEE Nuclear Science Symposium and Medical Imaging Conference Proceedings (NSS/MIC)*, IEEE, 2018, pp. 1–5.
- [71] A. Nassalski, M. Kapusta, T. Batsch, *et al.*, “Comparative study of scintillators for pet/ct detectors”, in *IEEE Nuclear Science Symposium Conference Record, 2005*, IEEE, vol. 5, 2005, pp. 2823–2829.
- [72] P. Cherenkov, “Visible luminescence of pure liquids under the influence of γ -radiation”, in *Dokl. Akad. Nauk SSSR*, vol. 2, 1934, pp. 451–454.
- [73] I. Frank and I. Tamm, “Coherent visible radiation of fast electrons passing through matter”, in *Selected Papers*, Springer, 1991, pp. 29–35.
- [74] J. V. Jelley, “Cerenkov radiation and its applications”, *Br. J. Appl. Phys.*, vol. 6, no. 7, p. 227, 1955.
- [75] S. Korpar, R. Dolenec, P. Križan, R. Pestotnik, and A. Stanovnik, “Study of tof pet using cherenkov light”, *NIM-A*, vol. 654, no. 1, pp. 532–538, 2011.
- [76] J. Löffler, J. Thomet, S. Frey, C. Ballif, and N. Wyrsh, “Single photon detection with amorphous silicon-based microchannel plates: a monte carlo model”, *NIM-A*, vol. 1032, p. 166 589, 2022.
- [77] F. Nolet, F. Dubois, N. Roy, *et al.*, “Digital sipm channel integrated in cmos 65 nm with 17.5 ps fwhm single photon timing resolution”, *NIM-A*, vol. 912, pp. 29–32, 2018.

- [78] J. C. I. Löffler, "Towards single photon detection with amorphous silicon based microchannel plates", EPFL, Tech. Rep., 2021.
- [79] J. Cazaux, "Reflectivity of very low energy electrons (< 10 eV) from solid surfaces: physical and instrumental aspects", *J. Appl. Phys.*, vol. 111, no. 6, p. 064 903, 2012.
- [80] J. R. M. Vaughan, "A new formula for secondary emission yield", *IEEE Trans. Electron Devices*, vol. 36, no. 9, pp. 1963–1967, 1989.
- [81] R. Thomas, J. Gibson, and G. Haas, "Low energy electron reflection (leer) and electron affinity of mgo", *Appl. Surf. Sci.*, vol. 5, no. 4, pp. 398–405, 1980.
- [82] M. S. Haque, H. Naseem, and W. Brown, "Aluminum-induced crystallization and counter-doping of phosphorous-doped hydrogenated amorphous silicon at low temperatures", *J. Appl. Phys.*, vol. 79, no. 10, pp. 7529–7536, 1996.
- [83] R. Wehrspohn, S. Deane, I. French, *et al.*, "Relative importance of the si-si bond and si-h bond for the stability of amorphous silicon thin film transistors", *J. Appl. Phys.*, vol. 87, no. 1, pp. 144–154, 2000.
- [84] H. Shanks and L. Ley, "Formation of pin holes in hydrogenated amorphous silicon at high temperatures and the yield strength of a-si: h.", *J. Appl. Phys.*, vol. 52, no. 2, pp. 811–813, 1981.
- [85] Y. Mishima and T. Yagishita, "Investigation of the bubble formation mechanism in a-si: h films by fourier-transform infrared microspectroscopy", *J. Appl. Phys.*, vol. 64, no. 8, pp. 3972–3974, 1988.
- [86] D. Burgreen, *Elements of thermal stress analysis*. CP Press, 1971.
- [87] C. Davis, "A simple model for the formation of compressive stress in thin films by ion bombardment", *Thin solid films*, vol. 226, no. 1, pp. 30–34, 1993.
- [88] E. Johlin, N. Tabet, S. Castro-Galnares, *et al.*, "Structural origins of intrinsic stress in amorphous silicon thin films", *Phys. Rev. B*, vol. 85, no. 7, p. 075 202, 2012.
- [89] G. G. Stoney, "The tension of metallic films deposited by electrolysis", *Proc. R. Soc. Lond.*, vol. 82, no. 553, pp. 172–175, 1909.
- [90] M. Van den Donker, R. Schmitz, W. Appenzeller, B. Rech, W. Kessels, and M. Van de Sanden, "The role of plasma induced substrate heating during high rate deposition of microcrystalline silicon solar cells", *Thin solid films*, vol. 511, pp. 562–566, 2006.
- [91] F. Laermer and A. Schilp, "Method of anisotropically etching silicon patent 5501893", *Office, USP, USA*, 1996.
- [92] J. W. Choi, W. L. Loh, S. K. Praveen, R. Murphy, and E. T. K. Swee, "A study of the mechanisms causing surface defects on sidewalls during si etching for tsv (through si via)", *J. Micromech. Microeng.*, vol. 23, no. 6, p. 065 005, 2013.
- [93] J. Arnold and H. H. Sawin, "Charging of pattern features during plasma etching", *J. Appl. Phys.*, vol. 70, no. 10, pp. 5314–5317, 1991.

- [94] S. J. Jokela, I. V. Veryovkin, A. V. Zinovev, *et al.*, “Secondary electron yield of emissive materials for large-area micro-channel plate detectors: surface composition and film thickness dependencies”, *Physics Procedia*, vol. 37, pp. 740–747, 2012.
- [95] J.-K. Lee, S.-H. Lee, J.-H. Min, I.-Y. Jang, C.-K. Kim, and S. H. Moon, “Oblique-directional plasma etching of si using a faraday cage”, *J. Electrochem. Soc.*, vol. 156, no. 7, p. D222, 2009.
- [96] B. Chang, “Oblique angled plasma etching for 3d silicon structures with wiggling geometries”, *Nanotechnology*, vol. 31, no. 8, p. 085301, 2019.
- [97] J. Frenkel, “On pre-breakdown phenomena in insulators and electronic semi-conductors”, *Physical Review*, vol. 54, no. 8, p. 647, 1938.
- [98] K. Mackenzie, P. L. Comber, and W. Spear, “The density of states in amorphous silicon determined by space-charge-limited current measurements”, *Philosophical Magazine B*, vol. 46, no. 4, pp. 377–389, 1982.
- [99] R. Weisfield, “Space-charge-limited currents: refinements in analysis and applications to a-si1-x ge x: h alloys”, *J. Appl. Phys.*, vol. 54, no. 11, pp. 6401–6416, 1983.
- [100] B. De Boer, A. Hadipour, M. M. Mandoc, T. Van Woudenberg, and P. W. Blom, “Tuning of metal work functions with self-assembled monolayers”, *Advanced Materials*, vol. 17, no. 5, pp. 621–625, 2005.
- [101] S. Jain and K. S. Krishnan, “Thermionic constants of metals and semiconductors iii. monovalent metals”, *Proc. R. Soc. Lond.*, vol. 217, no. 1131, pp. 451–461, 1953.
- [102] R. Street, “Thermal generation currents in hydrogenated amorphous silicon p-i-n structures”, *Appl. Phys. Lett.*, vol. 57, no. 13, pp. 1334–1336, 1990.
- [103] H. Leamy, “Charge collection scanning electron microscopy”, *J. Appl. Phys.*, vol. 53, no. 6, R51–R80, 1982.
- [104] W. E. Spicer and A. Herrera-Gomez, “Modern theory and applications of photocathodes”, in *Photodetectors and Power Meters*, SPIE, vol. 2022, 1993, pp. 18–35.
- [105] D. A. Orlov, J. DeFazio, S. D. Pinto, R. Glazenberg, and E. Kernen, “High quantum efficiency s-20 photocathodes in photon counting detectors”, *J. Instrum.*, vol. 11, no. 04, p. C04015, 2016.
- [106] A. Lamas-Linares, B. Calkins, N. A. Tomlin, *et al.*, “Nanosecond-scale timing jitter for single photon detection in transition edge sensors”, *Appl. Phys. Lett.*, vol. 102, no. 23, p. 231117, 2013.
- [107] B. W. Adams, A. Elagin, H. Frisch, *et al.*, “Timing characteristics of large area picosecond photodetectors”, *NIM-A*, vol. 795, pp. 1–11, 2015.

Acknowledgements

In this final part, I would like to acknowledge all the people that made this thesis possible. I will always fondly remember the last four years I spent at PV-LAB.

Firstly, I want to thank Prof. Christophe Ballif for admitting me into his laboratory, supervising my thesis, and sharing his passion for photovoltaics and a greener world- also, I truly admire your juggling skills. Then I would like to thank Dr. Nicolas Wyrsh for codirecting this thesis, for all the discussions and inputs, and for still believing in my abilities even after many failed wafers. I also want to thank my jury members: Prof. Edoardo Charbon, Dr. Anton Tremsin, Dr. Werner Lustermann, and Prof. Nicolas Grandjean, who spent their precious time evaluating my work and providing valuable feedback.

Thank you to the AMCP team- Janina, Jonathan, Mohammad and Luca. As we all know, AMCPs can be very frustrating, but we managed to get them to work together. I would especially like to thank Luca for taking over the long shifts in the cleanroom while I was busy screaming at my thesis draft. Working on AMCPs has been a lot more fun since you joined the team and I am sure you could have a bright future as a wirebonding technician (if you wanted to). I also would like to acknowledge the members of the Sinergia collaboration for the productive discussions. Thank you to the AMCP/LNA task force- Emanuele, Jad, and our colleagues in Bern- Coen and Andreas for making the timing measurements possible. I would also like to thank Simone for his help in the cleanroom, the idea to make stripe AMCPs and the amazing parmigiana.

Thank you to the staff at CMi, especially Niccolo Piacentini, Joffrey Pernollet, and Adrien Toros, for their help with our complicated process steps. To my other colleagues working at CMi (except the guy who stole my tweezers)- may all your processes be successful and your lives happy. To Fabienne Bobard from CIME for her help and patience at the microscope and to Ulf Roeser for his assistance with the characterization setup.

To Jonathan- for being my "work-husband" /motivational speaker/french teacher/player Nr.2 and most importantly, my friend. Thank you for the memes, the dad jokes, and your continuous support. To Daniel for all the proofreading, the coffee break discussions, and the hours we spent playing "Overcooked".

To all my office mates over the years- Josua, who showed me around in my early days in the lab and who left a small collection of wine in the office, Eleonora for drinking said wine with me, Janina, who introduced me to Acroyoga, Andrew who turned the office into a botanical garden, Hyunjung, my korean twin and drinking buddy, Alejandro my favorite social butterfly and Noémie- the tandem partner I've been waiting for. To Frank for all the coffee and chocolate breaks. To Karine for organizing my life for me, Hassan for performing CPR on my computer, Sylvain for his help with System D. To Ezgi, my climbing partner, Luca G. whose social skills I admire, and to all the other amazing people that are or have been part of PV-LAB. Thank you for all the lovely discussions, the parties, the barbeques, the ski trips, and the hikes.

Thank you to the girls from our FLP group: Chun-min, Janina, Julie, Lili and Victoria- I hope we will continue to support each other and stay friends in the years to come.

I also would like to thank my friends outside the lab who were always there to cheer me up when life was tough- Fabienne, Monja, Saskia, Marc, Michael, Yves, Christian, Christa and Chantal. To Justen for listening to me and pointing out the "irrational thoughts". To my parents and my sister for their support over these years. And finally, to Philipp for his love, all the back massages, bringing me food and coffee, and forcing me to take all my vacation days.

Neuchâtel, 23 November 2022

Samira

Samira Alexandra Frey

✉ Rue des Usines 37, Neuchâtel, Switzerland ☎ +41792357039 @ samira.frey@bluewin.ch



About me

I love exploring the world around me and finding solutions to challenging problems.

Personal Information

Nationality: Swiss
Birthday: 10.03.1992

Areas of Specialization

Microfabrication • Particle Detection • MCPs • PECVD

Technical Skills

Programming: Matlab/R, C/C++, Mathematica, Python, COMSOL Multiphysics
Microfabrication: PECVD, Photolithography, Etching, Sputtering, Evaporation, Characterization Techniques

General Interests

Snowboarding, diving, rock climbing, playing piano, reading, being outside and spending time with animals

Languages

German	Native
English	C2
French	B1
Russian	A1

EDUCATION

- 2018–2022 **Ph.D in Physics**
EPFL, NEUCHÂTEL · Photovoltaics-and Thin Film Laboratory 📍
Amorphous Silicon Based Microchannel Plates for a Time-of-Flight PET Scanner
- 2015–2017 **Master of Science in Physics**
UNIVERSITY OF BERN · Bern, Switzerland 📍
Master's thesis: "Chemical analysis of a lunar meteorite by laser ablation mass spectrometry"
- 2010–2015 **Bachelor of Science in Physics**
UNIVERSITY OF BERN · Bern, Switzerland 📍
Bachelor's thesis: "Direkte und Indirekte Suche nach Dunkler Materie".

WORK EXPERIENCE

- 2018–2022 **Research Assistant**
EPFL, NEUCHÂTEL · Photovoltaics-and Thin Film Laboratory 📍
Research about the development of amorphous silicon based microchannel plates
- 2018–2018 **Internship**
BIOZENTRUM UNIVERSITY OF BASEL · Basel, Switzerland 📍
Internship in transmission electron microscopy
- 2017–2018 **Tax Assistant**
VALORA CORPORATE TAX · Muttensz, Switzerland 📍
Assistance in national and international tax projects
- 2016–2017 **Volunteer and Freelance Pirate**
QUEENSLAND · Australia 📍
Caretaker for injured animals. This and that. The usual, aye?
- 2015–2016 **Teaching Assistant**
PHYSICS INSTITUTE UNIVERSITY OF BERN · Bern, Switzerland 📍
Mentored undergraduate students in laboratory work

PUBLICATIONS

- 2021** S. Frey, M. Beygi, C. Ballif, N. Wyrsh, "Fabrication and Characterization of High Aspect Ratio Amorphous Silicon Based Microchannel Plates", 2021 IEEE Nuclear Science Symposium and Medical Imaging Conference (NSS/MIC), virtual.
- 2019** S. Frey, J. Löffler, C. Ballif, N. Wyrsh, "Characterization of Amorphous Silicon Based Microchannel Plates with High Aspect Ratio", IEEE Nuclear Science Symposium and Medical Imaging Conference (NSS/MIC), Manchester, 2019, DOI: 10.1109/NSS/MIC42101.2019.9059714.
- 2019** Frey, S., Wiesendanger, R., Tulej, M., Neuland, M., Riedo, A., Grimaudo, V., Wurz, P. "Chemical analysis of a lunar meteorite by laser ablation mass spectrometry" Planetary and space science, 182, 104816.